INFORMATION TO USERS

This reproduction was made from a copy of a document sent to us for microfilming. While the most advanced technology has been used to photograph and reproduce this document, the quality of the reproduction is heavily dependent upon the quality of the material submitted.

The following explanation of techniques is provided to help clarify markings or notations which may appear on this reproduction.

1. The sign or "target" for pages apparently lacking from the document photographed is "Missing Page(s)". If it was possible to obtain the missing page(s) or section, they are spliced into the film along with adjacent pages. This may have necessitated cutting through an image and duplicating adjacent pages to assure complete continuity.
2. When an image on the film is obliterated with a round black mark, it is an indication of either blurred copy because of movement during exposure, duplicate copy, or copyrighted materials that should not have been filmed. For blurred pages, a good image of the page can be found in the adjacent frame. If copyrighted materials were deleted, a target note will appear listing the pages in the adjacent frame.
3. When a map, drawing or chart, etc., is part of the material being photographed, a definite method of "sectioning" the material has been followed. It is customary to begin filming at the upper left hand corner of a large sheet and to continue from left to right in equal sections with small overlaps. If necessary, sectioning is continued again—beginning below the first row and continuing on until complete.
4. For illustrations that cannot be satisfactorily reproduced by xerographic means, photographic prints can be purchased at additional cost and inserted into your xerographic copy. These prints are available upon request from the Dissertations Customer Services Department.
5. Some pages in any document may have indistinct print. In all cases the best available copy has been filmed.

University
Microfilms
International

300 N. Zeeb Road
Ann Arbor, MI 48106

8520988

Smith, Doran Dakota

PARITY NONCONSERVATION IN ZERO MOMENTUM TRANSFER LEPTON HADRON INTERACTIONS

The University of Michigan Ph.D. 1985

University
Microfilms
International 300 N. Zeeb Road, Ann Arbor, MI 48106

PARITY NONCONSERVATION IN ZERO MOMENTUM TRANSFER LEPTON HADRON INTERACTIONS

by
Doran Dakota Smith

A dissertation submitted in partial fulfillment
of the requirements for the degree of
Doctor of Philosophy
(Physics)
in The University of Michigan
1985

Doctoral Committee:

Professor William Williams, Chairman
Associate Professor Daniel Axelrod
Professor Karl T. Hecht
Associate Professor Trevor Mudge
Professor Y.P. Edward Yao

TABLE OF CONTENTS

LIST OF FIGURES iv

LIST OF TABLES vi

LIST OF APPENDICES viii

CHAPTER

I. INTRODUCTION 1

A. Introduction
B. The Known Forces
C. Symmetry Properties of the Known Forces
D. Unification of Forces
E. Parity Violation and the Hydrogen Atom

References for Chapter I

II. THE DOING OF A PARITY EXPERIMENT 16

A. General Approach
B. Hydrogen Parity Experiments
C. Data Collection and Analysis Features
D. Michigan Interaction Region
E. Structure of n=2 Hydrogen

E.1 Magnetic Field Dependence
E.2 Stark Matrix Elements
E.3 Weak Matrix Elements
E.4 Hyperfine Transitions near the β-e Crossing
E.5 Details of the Parity Nonconserving α_0-β_0 Transition
E.6 Role of Damping

References for Chapter II

III. INHOMOGENEOUS ELECTRIC FIELD LINESHAPES 38

A. Outline of the Approach Used to Evaluate Integrals over the Beam Cross Section for the Inhomogeneous Electric Field
B. Lineshapes for the Ideal Case
C. Effects of Misalignments and Non-Ideal Electrodes

CHAPTER

IV. SYSTEMATICS 48

- A. Invariant Analysis
- B. Classification of Invariants
- C. Invariant Analysis Neglecting Beam Divergence
- D. Effects of Interference Between Motional Electric Field from Beam Divergence and Inhomogeneous Applied Electric Fields

References for Chapter IV

V. APPARATUS 64

- A. Apparatus Overview
- B. Source and Collimation
- C. Beta Quench
- D. Interaction Region
  - D.1 Microwave Cavity
  - D.2 Electric Field Electrodes
- E. Magnetic Field
- F. Alpha Quench and Detection
- G. Neutral Bean Detector
- H. Support System
- I. Electronic Instrumentation
- J. Pumping

References for Chapter V

VI. DATA, PROBLEMS, AND FUTURE PLANS 82

- A. Introduction
- B. Current Limits on the Understanding of Beam and Field Alignment Techniques
- C. α_{+}-β_{0} Transition
- D. α_{0}-β_{0} Transition
- E. Future Plans

APPENDICES 87

LIST OF FIGURES

Figure

2.1 Conceptual Block Diagram of Hydrogen Parity Experiments . 18

2.2 Field Configuration of Michigan Interaction Region . . . 24

2.3 Magnetic Field Dependence of n=2 Hydrogen Eigenstates . . 25

2.4 α_0-β_0 Transition 31

3.1 Electric Field Due to Closely Spaced Semicylinders . . . 40

3.2 Distortions to Lineshapes Caused by Semicylinder Electrodes 44

4.1 Interference of Motional Electric Field Due to Beam Divergence and dc Electric Field Inhomogeneities 55

5.1 Apparatus Block Diagram 65

5.2 Schematic Illustration of Phi Flip 69

5.3 Interaction Cavity Alignment Methods 70

5.4 Solenoid Support System 74

5.5 Detection Region 77

5.6 Data Acquisition System 79

B.1 Microcontroller - General Block Diagram 108

B.2 Microcontroller - Detailed Block Diagram 110

B.3 Five Phase Clock 111

B.4 Buss Timing Cycle 114

C.1 Magnetic Field Control Unit - General Block Diagram . . . 119

C.2 Magnetic Field Control Unit - Detailed Block Diagram . . 123

C.3 Rapid Sequencing of Magnetic Field Value 127

Figure

C.4 NMR Tuned Tank Model 135

C.5a Feedback Loop for Tuned Tank Balance 140

C.5b Feedback Loop for NMR Signal 140

C.5c Generalized Feedback Loop for NMR and Tuned Tank Balance, Including Offset Voltages 140

LIST OF TABLES

Table

1.1 Known Forces and Their Interactions 3

1.2 Symmetry Properties of the Known Forces 5

1.3 C_{1p} and C_{1n} 11

1.4 C_{2p} and C_{2n} 11

1.5 Radiative Corrections to Selected C's as a Percent of Tree Level Values 12

2.1 Hydrogen Eigenstates for n=2, j=1/2 26

2.2 Stark Matrix Elements for n=2, j=1/2 27

3.1 Integrals over Electric Field Inhomogeneities for the All Aligned Case 45

4.1 Invariant Analysis of Rate to Lowest Order in the Fields 57

4.2 Field and Invariant Coefficients Values for α_0-β_0 at 540 gauss 58

4.3 Important Invariants Neglecting Beam Divergence 59

4.4 Invariants for Interference Between Beam Divergence and Electric Field Inhomogeneities 60

4.5 Integrals for the Interference of Motional Electric Fields Due to Beam Divergence and Electric Field Inhomogeneities for Relative Displacements in the X Direction 61

4.6 Integrals for the Interference of Motional Electric Fields Due to Beam Divergence and Electric Field Inhomogeneities for Relative Displacements in the Y Direction 62

A.1 Possible Transitions 101

A.2 Summary of Terms Used in the Lineshape Theory 102

Table

C.1 Frequently Used Symbols 130

C.2 Practical Numbers for NMR Stabilization Loop 142

LIST OF APPENDICES

Appendix

A. Generalized Version of Gordon Drake/Laurent Lévy Driven Three Level Problem 88

  A. Driven 3 level - strong resonances

    A.1 dc Stark transformations
    A.2 Time dependence

  B. Driven 3-Level α_0-β_0
  C. General Solution

  References for Appendix A

B. Microcontroller 105

  A. Introduction
  B. Comparison to a General Purpose Computer
  C. Block Diagram Description
  D. Detailed Circuit Description

    D.1 Five Phase Clock
    D.2 Microsequencer and Microprogram Memory
    D.3 Data Bus
    D.4 Memory
    D.5 ALU
    D.6 External Control

  E. Software Support
  F. Possible System Configurations

C. Magnetic Field Control Unit 118

  A. Introduction
  B. Block Diagram Description

    B.1 NMR Stabilization Loop
    B.2 Tuned-Tank Balance Circuitry
    B.3 Rapid Sequencing of the Magnetic Field
    B.4 Test Capability

C. Detailed Block Diagram Description

- C.1 NMR Stabilization Loop
- C.2 Tuned-Tank Balance Circuitry
- C.3 Rapid Sequencing of the Magnetic Field
- C.4 Test Capability

D. Performance Analysis

- D.1 Analytical Description of NMR and LRC Resonant Circuit
  - D.1(a) Fourier expansion of modulated Lorentzian line shapes
  - D.1(b) Description of LRC resonant circuit
  - D.1(c) NMR Lineshape
- D.2 Noise and Signal Strengths
  - D.2(a) Johnson noise of the coil
  - D.2(b) NMR absorption dip signal size
  - D.2(c) Noise introduced through tuned-tank balance circuitry (TTBC)
- D.3 Systematics
  - D.3(a) Description of detected Q-curve and NMR signal
  - D.3(b) Harmonic distortion
  - D.3(c) DC offsets at the multiplier output and the integrator input

References for Appendix C

CHAPTER I

INTRODUCTION

A. Introduction

One goal of physics is to understand nature on a fundamental level. This involves understanding the laws of nature with a minimum of assumptions. Realizing that two or more apparently independent concepts are manifestations of a more global concept results in a reduction in the number of necessary assumptions. Newton's law of gravitation led to a simpler understanding of the motions of the heavenly bodies. Maxwell unified our understanding of electricity and magnetism in one simple set of equations. This drive toward a simpler and a more global understanding is known as "unification" of the laws of nature.

Unification attempts in physics are currently focusing on the four known forces in nature. Instead of our understanding being divided between four apparently unrelated concepts, the goal is to understand the forces in terms of one set of related ideas, hence unification of the forces of nature.

B. The Known Forces

There are currently four known forces: strong, electromagnetic, weak, and gravitational. The strong force in its rest frame is short-ranged, ~10^{-13} cm, and is responsible for the attractive forces between hadrons. The electromagnetic force has an infinite range and is responsible for attractive/repulsive forces between all charged particles. The weak force in its rest frame is very short ranged, 10^{-17} cm, and is responsible for radioactive decay. The gravitational force has an infinite range and is responsible for the attractive force between all matter and energy.

Table 1.1 lists the forces, their relative strength, the types of particles which exhibits the interactions, and the particles which mediate the forces.

C. Symmetry Properties of the Known Forces

The forces may be characterized by the symmetry properties they obey. Relevant symmetry properties are: translational invariance, rotational invariance, parity, charge conjugation, and time reversal. Translational invariance states that all the laws of physics are invariant under translations. For example, define a coordinate system (say x, y, and z axis) in which an experiment is performed yielding a certain result. Then the same result will be obtained if the experiment is translated by any distance along any of the coordinate axes. Rotational invariance states that the laws of physics are invariant under a rotation of the experiment in space. Parity invariance (P) (or invariance under parity inversion) states that the result of an experiment is independent of whether the experiment or its mirror image is performed. Charge conjugation (C) states that the result of an experiment is independent of the relative sign of the

TABLE 1.1

Known Forces and Their Interactions

FORCE	PARTICLE HADRONS	 LEPTONS	RELATIVE STRENGTH	COUPLING CONSTANT	PARTICLE MEDIATING FORCE
Strong	X	--	10	$g^2/4\pi \quad c$	Spin 1 Gluons
Electromagnetic	X	X	1/137	α	Spin 1 Photon
Weak	X	X	1.01×10^{-5}	$G_F((m_pc)^2/ \quad ^3)$	Spin 1 $W^\pm$ Z^o
Gravitation	X	X	$\sim2.0\times10^{-43}$	$G(m_e^2/e^2)$	Spin 2 Graviton

charges involved, i.e. the signs of all the electric charges can be reversed (positive charges changed to negative, the negative charges changed to positive, and magnetic moments reverse sign) and the outcome of the experiment should not change. Time reversal (T) invariance states that if time ran backwards what is observed should also occur in nature, i.e., if all the t's in a set of equations describing an experiment were changed to -t's, the resulting set of equations should describe a possible experiment.

Until the 1950's it was believed that the four known forces were invariant under these operations, i.e., they respected these symmetries. However, in 1957, Wu and co-workers observed the violation of parity and charge conjugation by the weak force in the decay of Co^{60}.[1] With the demise of parity as a good symmetry, it was believed that a combination of more elementary symmetries was a symmetry. It was believed that parity inversion followed by charge conjugation (CP) was a good symmetry. Cronin and Fitch observed CP violation in the decay of K's.[2]

Since CP is not a good symmetry, it has been suggested that CP combined with time reversal (CPT) is a good symmetry. This demands that T be broken in such a way that CPT not be broken. Explicit violation of T, where an experiment sets boundary conditions and then observes forward and backward going reactions proceeding at different rates, has not been observed. However, further measurements and analysis on the K-meson system independently suggest both CP and T violation.

Currently translational and rotational invariance and CPT are believed to be good symmetries for all forces. However, the author wishes to emphasize that these symmetries are only thought to be good since no experiment has shown otherwise. There is an atomic physics experiment under way at the University of Washington which has a high sensitivity to PT violation.[3] If this experiment is successful in observing PT violation, it may shed light on whether CPT is a good symmetry. Table 1.2 lists the four forces and the symmetries they obey.

TABLE 1.2

Symmetry Properties of the Known Forces

FORCE	STRONG	ELECTROMAGNETIC	WEAK	GRAVITATIONAL
Symmetry				
Trans.	X	X	X	X
Rot.	X	X	X	X
Charge Conj.	X	X	N	X
Parity	X	X	N	X
Time Reversal	X	X	?	X

Key:
X symmetry respected
N symmetry not respected
? symmetry currently assumed not respected

D. Unification of Forces

The standard model is a proposed theory that unifies the weak and electromagnetic forces. It predicts the existence of the photon (γ), which mediates the electromagnetic force, and three vector bosons W^+, W^-, and Z^0, which mediate the weak force. The standard model is a gauge theory and is based on a series expansion in powers of α. Although the standard model was first suggested in 1967.[4] It received little attention until 1971, when 't Hooft showed[5] that the series expansion theory was renormalizable (converged) to all orders of α.

The parity non-conserving Z^0 is predicted to couple to quarks as well as leptons. Previously the only coupling of quarks and leptons was thought to be via the parity conserving electromagnetic interaction photon. This means that the interactions in atomic systems are predicted to be a combination of electromagnetic and weak interactions, and threfore, should not respect parity.

The Z^0 was observed indirectly in 1973 in muon-neutrino electron scattering,[6] and the effects of it in several atomic physics experiments from the mid 70's to present.[7] In 1983 the vector bosons were produced at CERN.[8] The concensus is that the zero'th order predictions of the standard model have been verified. What remains is the more accurate measurement of the W^+, W^-, and Z^0 masses, and more importantly, measurement of the radiative corrections.

E. Parity Violation and the Hydrogen Atom

The standard model predicts that the hydrogen atom should display observable effects due to weak interactions. The purpose of this experiment is to measure parity violating effects in the hydrogen atom, and, consequently, provide conformation of, or deny the standard model.

The ultimate accuracy of this experiment, and hence its possible contribution, requires understanding the relationship between the predictions of the standard model and the measured quantities.[9]

To relate the predictions of the standard model to experimentally measured quantities, some results from Chapter II are used. Atomic parity violation experiments measure a quantity proportional to the product of the S state and derivative of the P state electronic wave functions at the nucleus, the quantites of interest C_{ip}, or C_{in} $(i = 1,2,3)$, and some well known constants. The standard model predicts the C's for electron-quark interactions, not electron-nucleon interactions, i.e., the measured C's are derived quantities, not fundamental ones. Therefore, interpretation of experimental results involves two sources of error. One is the error in the value of the atomic wave functions at the nucleus. This error is insignificant when using atomic hydrogen, but probably not less than 10% for any of the heavy atom experiments.[10] The second source of error affecting even hydrogen is that in deriving the C's for nucleons from the C's for quarks, uncertainties due to the strong interaction are directly reflected in the final answer.

The parity-violating potential between quarks and electrons can be parameterized phenomenologically as,

$$H_{PV}^{e-q} = \frac{G_F}{\sqrt{2}} \int d^3x\{\bar{e}\gamma_\mu\gamma_5 e(C_{1u}\bar{u}\gamma_\mu u + C_{1d}\bar{d}\gamma_\mu d) \tag{1.1}$$

$$+ \bar{e}\gamma_\mu e(C_{2u}\bar{u}\gamma_\mu\gamma_5 u + C_{2d}\bar{d}\gamma_\mu\gamma_5 d) + \bar{e}\sigma_{\mu\nu}q_\nu e(C_{3u}\bar{u}\gamma_\mu\gamma_5 u + C_{3d}\bar{d}\gamma_\mu\gamma_5 d)\}$$

where the C's are dimensionless coupling constants. Neglecting strong interactions, the tree level C's are,

$$\begin{aligned} C_{1u} &= R(1-2v_\theta)/6, \\ C_{1d} &= R(v_\theta-2)/6, \\ C_{2u} &= -Rv_\theta/2, \\ C_{2d} &= Rv_\theta/2, \\ C_{3u} &= 0, \\ C_{3d} &= 0, \end{aligned} \tag{1.2}$$

where $v_\theta = 4s^2_\theta - 1$, $s^2_\theta = \sin^2\theta_W = 1 - M_W^2 / M_Z^2$, $R = (37.281\ \text{GeV}/(M_W s_\theta))^2 \cong 1$, M_W and M_Z are the masses of the $W^\pm$ and Z^o, respectively.

The calculation of the radiative corrections to the C's is very complicated and is the subject of Bryan Lynn's thesis.[11] His assumptions include:

1) neglecting all Cabibbo-type mixings between generations of quarks,
2) neglecting the strong interactions of quarks,
3) assuming there are only three generations of light fermions,
4) taking the limit of $q^2=0$,
5) keeping only terms of $O(\alpha G_\mu)$,
6) neglecting all bound state effects; the S matrix for free particle quark-electron scattering is used (Bryan Lynn, and R.G. Stuart are currently calculating all one-loop radiative corrections for one electron atoms using bound state methods).

Approximations 1)-5) result in an error of less than 0.01 in the value of C_{iu} and C_{id}. The result of this calculation is the surprisingly simple closed form solutions given by equations 7 and 8 of ref. 9.

Using Sirlin's[12] work, Lynn eliminates the M_W dependence in favor of a much better known quantity, the measured lifetime of the muon (τ_μ). It is then possible to write the C's as functions of only M_Z and the Higgs mass (M_H). Using τ_μ as renormalized input data rather than $\bar{M}_W$ results in a 7% reduction in the values of all the C's at the tree level.

The C's for the electron-quark potential and the electron-nucleon potential can now be related. The effective electron-nucleon Hamiltonian is,

$$H_{PV}^{e-N} = \frac{G_\mu}{\sqrt{2}} \int d^3x \, \{\bar{e}\gamma_\mu\gamma_5 e(C_{1p}\bar{p}\gamma_\mu p + C_{1n}\bar{n}\gamma_\mu n)$$

$$+ \bar{e}\gamma_\mu e(C_{2p}\bar{p}\gamma_\mu\gamma_5 p + C_{2n}\bar{n}\gamma_\mu\gamma_5 n) \tag{1.3}$$

$$+ \bar{e}\sigma_{\mu\nu}q_\nu e(C_{3p}\bar{p}\gamma_\mu\gamma_5 p + C_{3n}\bar{n}\gamma_\mu\gamma_5 n)\} ,$$

where p denotes the proton and n the neutron. Using strong chiral SU(3)×SU(3)[13,14] the desired relationship is,

$$\begin{aligned}
C_{1p} &= 2C_{1u} + C_{1d} \\
C_{1n} &= C_{1u} + 2C_{1d} \\
C_{2p} &= g_A/g_V(2C_{2u} + C_{2d}) - 2D(C_{2u} + C_{2d}) \\
C_{2n} &= g_A/g_V(C_{2u} + 2C_{2d}) - 2D(C_{2u} + C_{2d}) \\
C_{3p} &= g_A/g_V(2C_{3u} + C_{3d}) - 2D(C_{3u} + C3d) \\
C_{3n} &= g_A/g_V(C_{3u} + 2C_{3d}) - 2D(C_{3u} + C_{3d})
\end{aligned} \tag{1.4}$$

where $g_A/g_V = 1.255\pm0.006$ and $D = 0.826\pm0.007$.

Tables 1.3 and 1.4 give C_{1p}, C_{1n} and C_{2p}, C_{2n} for hydrogen and ($C_{1p} + C_{1n}$) for deuterium as functions of M_Z and M_H. The rapid variation of C_{2p} in the vicinity of the Z^0 mass, $M_Z = 95.2\pm2.5$ GeV[15]is caused by rapid variation of C_{2u}, C_{2D}, Table 1.5 gives the percent corrections to the tree value C's caused by the radiative corrections. The percentages are large for C_{1p} and C_{2p} because C_{ip} and C_{2p} are supressed at the tree level.

How accurate are these results? The errors quoted in (1.4) for g_A/g_V and D are only experimental errors. Derivation of these numbers from the data is based on current theoretical understanding of strong interactions. g_A/g_V is derived by assuming only strong SU(2) global symmetry between protons and neutrons[13]. This is believed accurate to better than 1%, resulting in less than 1% error in the derivation of g_A/g_V. Since (see equ. (7) and (8) ref. 9),

$$C_{3u} + C_{3d} = C^T_{2u} + C^T_{2d} = 0 ,$$

Table 1.3

C_{1p} and C_{1n}

	$C_{1p}(H)$			$C_{1n}(H)$			$C_{1p}+C_{1n}$
M_Z \ M_H	10	100	1000	10	100	1000	100
90.0	.0184	.0165	.0141	-.490	-.490	-.490	-.948
90.9	.0318	.0301	.0280	-.490	-.490	-.489	-.919
91.8	.0446	.0430	.0412	-.489	-.489	-.489	-.892
92.7	.0568	.0553	.0537	-.488	-.488	-.489	-.866
93.6	.0684	.0671	.0656	-.488	-.488	-.488	-.842
94.4	.0795	.0782	.0770	-.487	-.487	-.488	-.818
95.3	.0900	.0889	.0879	-.486	-.487	-.487	-.796
96.2	.100	.0991	.0983	-.486	-.486	-.487	-.774
97.1	.110	.109	.108	-.485	-.486	-.487	-.754
98.0	.119	.118	.118	-.485	-.485	-.486	-.734

Table 1.4

C_{2p} and C_{2n}

	$C_{2p}(H)$			$C_{2n}(H)$		
M_Z \ M_H	10	100	1000	10	100	1000
90.0	.0179	.0158	.0132	-.0146	-.0125	-.00998
90.9	.0341	.0321	.0298	-.0306	-.0286	-.0264
91.8	.0494	.0475	.0455	-.0457	-.0439	-.0420
92.7	.0639	.0622	.0605	-.0601	-.0584	-.0568
93.6	.0777	.0762	.0747	-.0737	-.0722	-.0708
94.4	.0909	.0895	.0883	-.0867	-.0854	-.0842
95.3	.103	.102	.101	-.0992	-.0979	-.0970
96.2	.115	.114	.114	-.111	-.110	-.109
97.1	.127	.126	.125	-.122	-.121	-.121
98.0	.138	.137	.137	-.133	-.132	-.132

Table 1.5

Radiative Corrections to Selected C's as a Percent of Tree Level Values

M_H = 100 GeV

$C_{1p}+C_{1n}(^2H)$	$C_{1p}(H)$	$C_{2p}(H)$	$C_{1n}(H)$
3.01	-58.8	-68.6	-1.93
- .099	-24.7	-31.6	-2.07
- 3.05	7.62	- 5.32	-2.19
- 5.85	38.4	23.9	-2.32
- 8.52	67.6	51.7	-2.43
-11.1	95.6	78.2	-2.54
-13.5	122.	104.	-2.65
-15.8	148.	128.	-2.75
-18.1	172.	151.	-2.85
-20.2	196.	173.	-2.95

where the T means tree level, and all others include first order radiative corrections. The results for C_{1p}, C_{1n}, C_{3p}, C_{3n}, C^T_{2p}, and C^T_{2n} are good to 1%.

Unfortunately, C^1_{2p} and C^1_{2n}, the first order radiative corrections to C_{2p} and C_{2n}, suffer from at least three sources of strong interaction uncertainty[16]. 1) Derivation of D from the experimental data was based on chiral SU(3)×SU(3) symmetry which is good to only 10-30%. Therefore, D could by off by as much as 30%. 2) There could be exchange of $W^\pm$ and Z^0 between quarks within the nucleus which interaction is carried out to the electrons by photons. This would effect the values of C_{2p} and C_{2n} only. 3) Collins et.al. have shown that the axial-vector anomaly could change C_{2u}, C_{2d}, C_{3u}, and C_{3d} by as much as 10%.[17] Given the three sources of strong interaction uncertainty, the error in the calculation of C_{2p} and C_{2n} may be greater than 10%.

The C_1's do not involve any significant strong interaction uncertainty (see equ 1.4). C_{1p} is suppressed at the tree level, and due to radiative corrections varies rapidly in the vicinity of the Z^0 mass (95.3 GeV) (see Tables 1.3 and 1.5). C_{1n} is not suppressed at the tree level nor does it vary rapidly near the Z^0 mass. The size of the first order radiative corrections at 95.3 GeV are $C_{1p}^1 = 0.0489$ and $C_{1n}^1 = 0.0130$. Not until M_Z is < 92.7 GeV does $C_{1p}^1 <= C_{1n}^1$. Since 92.7 GeV is CERN's lower limit for M_Z, ignoring all experimental concerns, C_{1p} may provide the largest and most reliable measurement of the first order radiative corrections.

However, given the impetus of an experimental result obtained in hydrogen to better than 10%, some people believe that lattice gauge theories could be used to do more accurate calculations,[18] and some believe that such predictions are premature.[19] Given a 10% (assuming only 10%) uncertainty in the theoretical prediction of C_{2p} and C_{2n} an experimental answer good to better than 10% would still improve the current limits on the Z^0 mass, and provide the first measurement of radiative corrections predicted by the standard model.

References for Chapter I

1. C.S. Wu, E. Amber, R.W. Hudson, D.D. Hoppes, and R.P.Hayward, Phys. Rev. 105, 1413 (1957).

2. Nobel acceptance speeches, V.L. Fitch, Rev. mod. Phys. 53, 367 (1981); J.W. Cronin, Rev. Mod. Phys. 53, 373 (1981).

3. T.G. Vold, F.J. Raab, B. Heckel, E.N. Fortson, Phys. Rev. Lett. 52 (1984 2229.

4. S. Weinberg, Rev. Mod. Phys. 52, 3 (1980) 515; A. Salam, Rev. Mod. Phys. 52, 3 (1980) 525; S. Glashow, Rev. Mod. Phys. 52, 3 (1980) 539; and the many references given therein.

5. G. 't Hooft and M. Veltman, Nucl. Phys. B44 (1972) 189.

6. F.J. Hasert, et al., Phys. Lett. 46B (1973) 121.

7. Cesium: M.A. Bouchiat, J. Guena, L. Hunter, and L. Pottier, Phys. Lett. 117B (1982) 358.
   Thallium: P. Bucksbaum, E. Commins and L. Hunter, Phys. Rev. Lett. 46 (1981) 640.
   Bismuth: P.E.G. Baird, P.G.H. Sandars, et al., Phys. Rev. Lett. 39 (1977) 798.

8. G. Arnison, et.al., Phys. Lett. 126B, (1983) 398-410.

9. The author wishes to thank Bryan W. Lynn for his detailed and critical reading of this section. His help is much appreciated. Unless otherwise stated everything in this section is the work of Bryan Lynn. The source used in prepration of this work was the internal report "Order αG_μ Corrections to the Parity-Violating Electron-Quark Potential in the Weinberg-Salam Theory: Parity-Violations in Atoms", Bryan W. Lynn, University of Oxford, Clarendon Laboratory, Ref: 89/83.

10. C. Bouchiat, in: "Atomic Physics" 7, eds. D. Kleppner and F.M. Pipkin (Plenum Press, New York and London, 1981) and references quoted there.

11. Bryan W. Lynn, "$O(\alpha G_\mu)$ corrections to the parity-violating electron-proton potential in the Weinberg-Salam Theory" Ph.D. Thesis, Columbia Univ. January, 1982 (266 pgs.) University Microfilm.

12. A. Sirlin, Phys. Rev. D 27 (1983) 522.

13. R. Cahn and G. Kane, Phy. Lett. B 71 (1977) 348.

14. H. Pagels, Physics Reports 16 (1975) 220.

15. the Z^0 mass reference, See also the $W^{\pm}$ ref. .

16. There are currently two hydrogen parity experiments: Michigan and University of Washington. Both experiments are measuring C_{2p}.

17. J. Collins, F. Wilczek, A. Zee, Phys. Rev. D 18 (1978), 242.

18. Bryan W. Lynn, private communication.

19. Ed Yao, private communication.

CHAPTER II

THE DOING OF A PARITY EXPERIMENT

A. General Approach

Chapter I stated that the idea of parity is: Does an experiment and its mirror image yield the same result? In some situations this is not complete enough, for the mirror image of some experimental configurations can be obtained by a spatial rotation of the experiment, thus testing only rotational invariance. The required refinement is the concept of handedness. An object with a handedness is an object who's mirror image is unique, i.e. cannot be obtained by a spatial rotation of the initial object. Therefore, to test parity, an experiment must have a handedness.

Invariance under parity inversion can be tested by performing two experiments, perhaps by building a machine with a distinct handedness and its mirror image. If the results differ, parity is violated. Since weak interaction effects in atomic systems are so small, this is an impossible approach, since it is impossible to build a second machine close enough to the exact mirror image of the first machine to be able to see the effects. A practical approach is to build one machine whose handedness can be reversed. The experiment is then performed by periodically reversing the handedness and phase sensitively detecting changes in the result.

B. Hydrogen Parity Experiments

Figure 2.1 is a conceptual block diagram of all hydrogen parity experiments being performed.[1] Atomic hydrogen is prepared in an initial state, passed through a handed interaction region where it is driven to a final state, and then the population of the final state is detected. All current experiments use a hyperfine transition in the $n=2$ state. If the transition violates parity, the final state population will depend upon the handedness of the interaction region. If the handedness of the interaction region is perfectly reversed, any change in the population of the final state (neglecting statistics) is due to parity violation, and nothing else need be known, including the details of the interaction region. However, no reversal of the handedness of an interaction region is exact as a consequence of systematic effects. Although there are no parity conserving (PC) effects which behave like parity nonconserving (PNC) effects, in an experiment where there is a limited amount of information available, there can be PC effects which mimic PNC effects. This dictates a complete understanding of all effects that can mimic PNC effects.

The probability to be in the final state in all hydrogen parity experiments can be written as

$$|A|^2 = |A_{PC} \pm A_{PNC}|^2 = |A_{PC}|^2 \pm 2\mathrm{Re}(A_{PC}A_{PNC}) + |A_{PNC}|^2 \qquad (2.1)$$

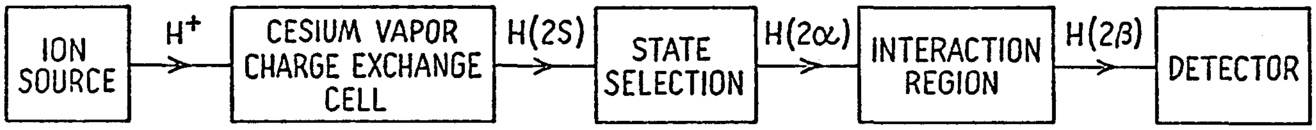

Figure 2.1 Conceptual Block Diagram of Hydrogen Parity Experiments

where the ± sign depends upon the relative handedness of the interaction region. Since the PNC amplitude A_{PNC} is very small with respect to the PC amplitude A_{PC}, the $|A_{PNC}|^2$ term will be dropped. The phase angle between A_{PC} and A_{PNC} should be close to zero to maximize the size of the interference term. The observed rate is given by

$$R^{(\pm)} = K|A_{PC} \pm A_{PNC}|^2 \cong R_{PC} \pm R_{PNC} \tag{2.2}$$

where K is a constant. A quantity independent of the overall rate is the asymmetry,

$$A = \frac{R^{(+)} - R^{(-)}}{R^{(+)} + R^{(-)}} = \frac{R_{PNC}}{R_{PC}} = \frac{2\mathrm{Re}A^*_{PC}A_{PNC}}{|A_{PC}|^2} = \frac{2|A_{PNC}|\cos\theta}{|A_{PC}|} \tag{2.3}$$

where θ is the phase angle between A_{PC} and A_{PNC}. Assuming only statistical noise, the signal-to-noise ratio for an integration time T is,

$$S/N = \frac{\text{PNC events}}{\sqrt{\text{PC events}}} = \frac{R_{PNC}T}{\sqrt{R_{PC}T}} = \frac{AR_{PC}T}{\sqrt{R_{PC}T}} = A\sqrt{R_{PC}T}\ . \tag{2.4}$$

The time required to achieve a given signal-to-noise is

$$T = \frac{(S/N)^2}{A^2R_{PC}} \tag{2.5}$$

The current work contains more than statistical noise. Due to cascade decay from higher lying states[2] (n ~ 10-12) and the very small size of $|A_{PC}|$, there is a background (B), x times larger than R_{PC}. In this case, equations (2.2)-(2.5) become

$$\begin{gathered} R^{(\pm)} = R_{PC} \pm R_{PNC} + B = R_{PC}(1+x) \pm R_{PNC} \\ A = \frac{R_{PNC}}{R_{PC}} \frac{1}{1+x} = A_o \frac{1}{1+x} \qquad (2.6) \\ S/N = \frac{R_{PNC}T}{\sqrt{(R_{PC} + B)T}} = A_o\sqrt{R_{PC}T} \frac{1}{\sqrt{1+x}} = (S/N)_o \frac{1}{\sqrt{1+x}} \\ T = \frac{(S/N)_o^2}{A_o^2 R_{PC}} (1+x) = T_o(1+x) \end{gathered}$$

where A_o, etc. are the corresponding quantities without the background.

C. Data Collection and Analysis Features

The PNC asymmetry due to the reversal of an interaction region handedness (flip) is very small, but has the useful feature that it changes sign under a flip, hence it can be phase-sensitively detected. Equation (2.3) is the asymmetry between the two handednesses of the interaction region. A typical experiment contains N independent reversals of the interaction region handedness. Common methods include reversing the direction of an electric or magnetic field, or laser polarization. The N reversals are useful for reducing unwanted effects when collecting and analyzing the data. This is illustrated with an example from a two flip experiment such as one involving reversals of electric and magnetic fields. Let

$$
\begin{aligned}
R^{++} &= R_{PC} + R_{PNC} \\
R^{+-} &= R_{PC} - R_{PNC} \\
R^{-+} &= R_{PC} - R_{PNC} \\
R^{--} &= R_{PC} + R_{PNC}
\end{aligned}
\tag{2.7}
$$

where R^{++}, etc. are the observed rates. The following quantity extracts the PNC rate as a fraction of the total rate, i.e., the asymmetry,

$$\frac{(R^{++} + R^{--}) - (R^{-+} + R^{+-})}{(R^{++} + R^{--}) + (R^{-+} + R^{+-})} = \frac{R_{PNC}}{R_{PC}} \, . \tag{2.8}$$

Generalizing this to an N flip experiment,

$$\frac{\sum\limits_{ij..N=0}^{1} R^{ij..N} \, (-)^{ij..N}}{\sum\limits_{ij..N=0}^{1} R^{ij..N}} = \frac{2^N R_{PNC}}{2^N R_{PC}} = \frac{R_{PNC}}{R_{PC}} \tag{2.9}$$

where $R^{00..0} \equiv R^{--..-}$ and $R^{11..1} \equiv R^{++..+}$, i.e. $R^{1101} = R^{++-+}$.

Practically no flip is perfect, $R^{+}_{PC} \neq R^{-}_{PC}$. How these imperfections affect the asymmetry depends upon their functional dependence on the physical quantities involved. Assume terms of the form $cf_1^2 f_2^2$ appear in the PC rate, where f_1 and f_2 are the magnitudes of two fields, and c is a constant independent of f_1 and f_2. For a two flip experiment let

$$\begin{aligned} R^{++} &= cf_1^2 f_2{}^2 + R_{PNC} \\ R^{+-} &= c(f_1 - \delta_1)^2 f_2^2 - R_{PNC} \\ R^{-+} &= cf_1^2(f_2-\delta_2)^2 - R_{PNC} \\ R^{--} &= c(f_1 - \delta_1)^2(f_2 - \delta_2)^2 + R_{PNC} \end{aligned} \tag{2.10}$$

where δ_1 and δ_2 account for errors in the field reversals. The asymmetry is

$$A = \frac{cf_1 f_2 \delta_1 \delta_2 + O(\delta^3) + R_{PNC}}{cf_1^2 f_2^2 + O(\delta)} \cong \frac{\delta_1 \delta_2}{f_1 f_2} + \frac{R_{PNC}}{R_{PC}} \tag{2.11}$$

Although part of the contribution to the asymmetry is from imperfect reversals, only the product of the errors is present. Hence, the origin of the rule of thumb, "to do a 1 ppm experiment with three flips requires three 1% flips."

Although the previous method is the heart of the data collection process, the author feels that both collection and analysis of data deserve more attention, but has done little due to time limitations. Lévy discusses the analog-to-digital conversion of the detection region output.[3] Harrison, et al. discuss the random flipping of the fields to suppress spurious noise sources,[4] and extract certain systematics.

D. Michigan Interaction Region

The fields of the interaction region in the Michigan experiment are shown in figure 2.2. In principle it does not matter in what direction the atomic beam transverses the interaction region. However, any component of $\vec{B}$ perpendicular to the atom velocity ($\vec{v}$) results in a motional electric field ($\vec{E}_m$) in the atom's rest frame. Since $\vec{E}_m$ results in undesirable systematics (see Chapter III), $\vec{v}$ is made parallel to $\vec{B}$.

There are three ways to reverse the handedness of this field configuration, reversing the direction of the dc electric field $\vec{E}$ (E-flip), reversing the direction of the dc magnetic field $\vec{B}$ (B-flip), or reversing the direction of the component of the 1.5 GHz rf electric field $\vec{\varepsilon}$ parallel to $\vec{E}$ (ϕ-flip).

E. Structure of n=2 Hydrogen

E.1 Magnetic Field Dependence

The magnetic field dependence of the eigenstates in the n=2 shell of hydrogen is shown in figure 2.3. The eigenstates are labeled using Lamb's notation[5]. The Greek and Latin letters label hyperfine structure states and the subscripts are $m_f = m_i + m_j$, where i is nuclear spin and j is the total electronic angular momentum. Since the transition of interest is very weak, ~4 ppm, it is not possible to do accurate calculations of the transition rate without including all 16 hyperfine levels.[6] However, for a first approximation, the $j = 3/2$ levels may be ignored. Wavefunctions for the $j = 1/2$ levels are given in Table 2.1.[7] At the magnetic field value of interest, ~550 gauss,

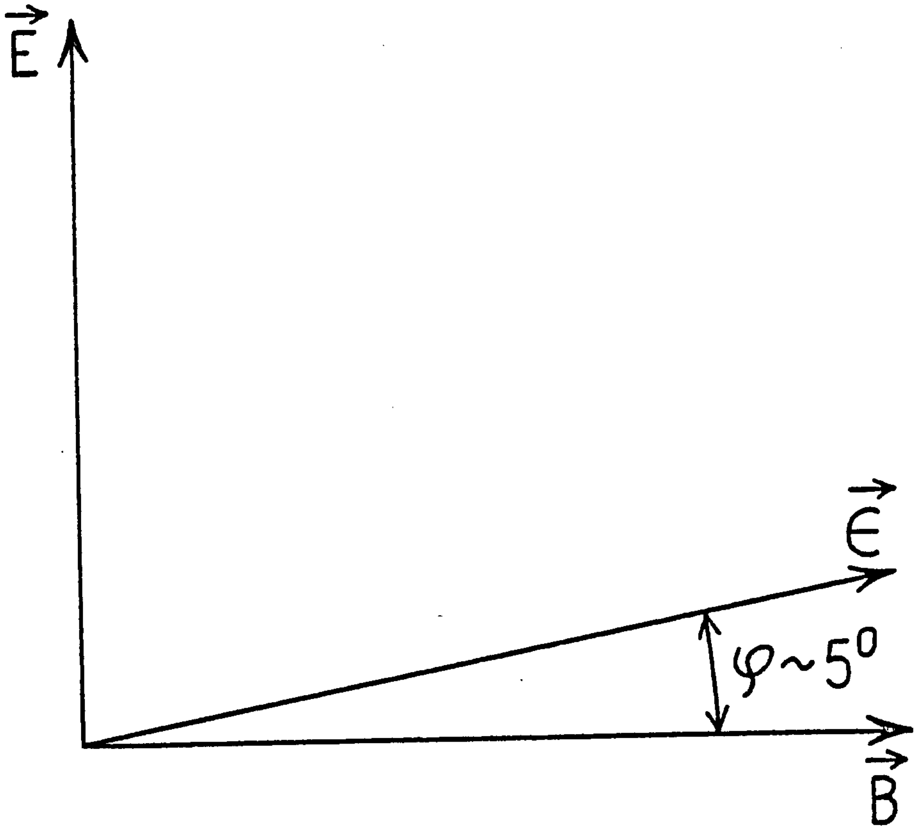

Figure 2.2 Field Configuration of Michigan Interaction Region

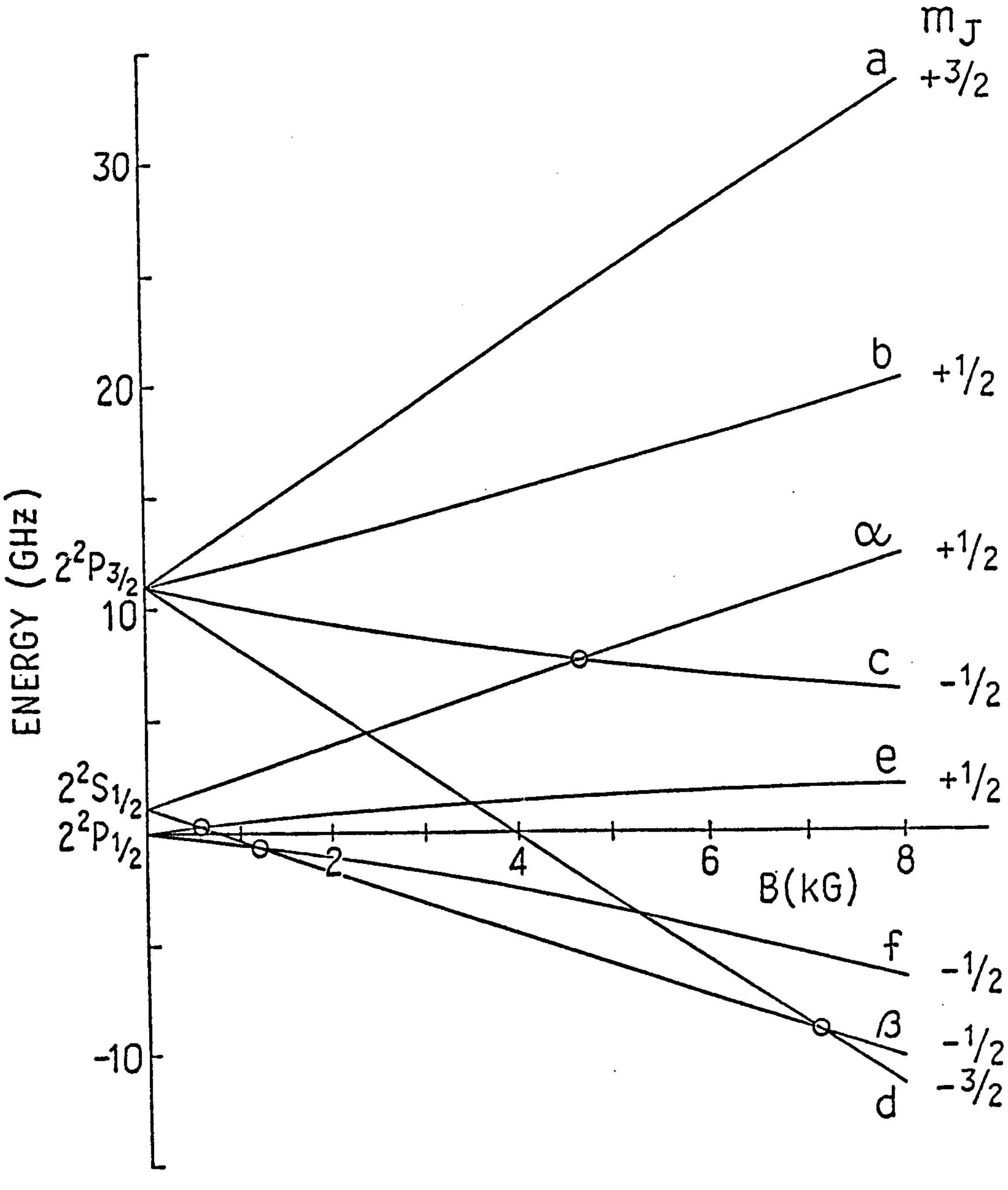

Figure 2.3 Magnetic Field Dependence of n=2 Hydrogen Eigenstates

Table 2.1

Hydrogen Eigenstates for n=2, j=1/2

$$|\alpha_{+1}\rangle \equiv |2S + \frac{1}{2} + \frac{1}{2}\rangle$$

$$|\alpha_0\rangle \equiv \cos\Theta_S |2S + \frac{1}{2} - \frac{1}{2}\rangle + \sin\Theta_S |2S - \frac{1}{2} + \frac{1}{2}\rangle$$

$$|\beta_0\rangle \equiv \cos\Theta_S |2S - \frac{1}{2} + \frac{1}{2}\rangle - \sin\Theta_S |2S + \frac{1}{2} - \frac{1}{2}\rangle$$

$$|\beta_{-1}\rangle \equiv |2S - \frac{1}{2} - \frac{1}{2}\rangle$$

$$|e_{+1}\rangle = |2P + \frac{1}{2} + \frac{1}{2}\rangle$$

$$|e_0\rangle = \cos\Theta_P |2P + \frac{1}{2} - \frac{1}{2}\rangle + \sin\Theta_P |2P - \frac{1}{2} + \frac{1}{2}\rangle$$

$$|f_0\rangle = \cos\Theta_P |2P - \frac{1}{2} + \frac{1}{2}\rangle - \sin\Theta_P |2P + \frac{1}{2} - \frac{1}{2}\rangle$$

$$|f_{-1}\rangle = |2P - \frac{1}{2} + \frac{1}{2}\rangle$$

$$\Theta_P \cong \Theta_S$$

$$\cos\Theta = \frac{1}{\sqrt{2}} \left\{x^2 + 1 - x\sqrt{x^2 + 1}\right\}^{-1/2}$$

$$x = \frac{(g_J + g_I)\mu_0 B}{\Delta}$$

Δ = zero field h.f.s. splitting

$$g_J \simeq \frac{3[j(j+1)] - \ell(\ell+1) + s(s+1)}{2j(j+1)}$$

$$g_I \simeq \frac{m_e}{m_p}\,(5.56)$$

$\sin\Theta \sim 1/20$, resulting in the wavefunctions being almost pure m_j states.

E.2 Stark Matrix Elements

Since electric fields (static or rf) only mix states of opposite parity $\ell_{initial}$ must differ from ℓ_{final}. They cannot mix states of opposite nuclear spin. z fields cannot change m_f, and x and y fields change m_f by ±1 only. Relevant Stark matrix elements are given in Table 2.2.[8]

Table 2.2

Stark Matrix Elements for n=2, j=1/2 (units of $\sqrt{3}\, ea_0$.)

$\langle e_+|z|\alpha_+\rangle = +1$

$\langle e_+|x|\alpha_0\rangle = \sin\Theta$

$\langle e_+|x|\beta_0\rangle = \cos\Theta$

$\langle e_0|x|\alpha_+\rangle = \sin\Theta$

$\langle e_0|z|\alpha_0\rangle = \cos 2\Theta$

$\langle e_0|z|\beta_0\rangle = -\sin 2\Theta$

$\langle e_0|x|\beta_-\rangle = \cos\Theta$

$\langle f_0|x|\alpha_+\rangle = \cos\Theta$

$\langle f_0|z|\alpha_0\rangle = -\sin 2\Theta$

$\langle f_0|z|\beta_0\rangle = -\cos 2\Theta$

$\langle f_0|x|\beta_-\rangle = -\sin\Theta$

$\langle f_-|x|\alpha_0\rangle = \cos\Theta$

$\langle f_-|x|\beta_0\rangle = -\sin\Theta$

$\langle f_-|z|\beta_-\rangle = -1$

Θ is the hyperfine angle defined in Table 2.1.

y matrix elements are obtained by multiplying the x matrix elements by i.

Matrix elements are in units of $\sqrt{3}\, ea_0$.

E.3 Weak Matrix Elements

Formulating this parity experiment in as general a way as possible means writing down a phenomenological parity nonconserving Hamiltonian which is independent of any gauge model,[9]

$$H_{PV}^{e-N} = \frac{G_\mu}{\sqrt{2}} \int d^3x\{\bar{e}\gamma_\mu\gamma_5 e(C_{1p}\bar{u}\gamma_\mu p + C_{1d}\bar{n}\gamma_\mu n)$$

$$+ \bar{e}\gamma_\mu e(C_{2p}\bar{p}\gamma_\mu\gamma_5 p + C_{2n}\bar{n}\gamma_\mu\gamma_5 n)$$

$$+ \bar{e}\sigma_{\mu\nu}q_\nu e(C_{3p}\bar{p}\gamma_\mu\gamma_5 p + C_{3n}\bar{n}\gamma_\mu\gamma_5 n)\} \qquad (2.12)$$

Lévy gives a complete list of weak matrix elements in n=2 hydrogen and deuterium.[10] C_3 is due to the electron weak anomalous moment. It is expected to be small with respect to the other terms and will be dropped. A nonrelativistic reduction of the first two terms and evaluation in the j=1/2 states of hydrogen results in,[11]

$$\langle nP_{1/2}|H_1^W|nS_{1/2}\rangle = iC_1\overline{V}\delta_{m_j'm_j}\delta_{m_i'm_i}$$

$$\langle nP_{1/2}|H_2^W|nS_{1/2}\rangle = -2iC_2\overline{V}\delta_{m_j'\pm 1m_j}\delta_{m_i'\pm 1m_i} \qquad (2.13)$$

where

$$\overline{V} = \frac{3G_F}{\sqrt{2}\ 8\pi}\frac{}{mc} R_{n1}'(0)R_{no}(0) = 0.118Z^4\frac{\sqrt{n^2-1}}{n^4}\text{ Hz}$$

where G_F is the fermi constant and $R_{no}(0)$ and $R_{n1}'(0)$ are the S wave function and first derivative of the P wave function at the origin, respectively. The only non-vanishing matrix element of interest to the current work is

$$\langle e_0 | H^W | \beta_0 \rangle = -i\sqrt{2}VC_{2p}\cos 2\Theta \qquad (2.14)$$

As shown in Table 1.4 the value of C_{2p} is expected to be of the order 0.1.

E.4 Hyperfine Transitions near the β-e Crossing

Of the eight n=2, j=1/2 magnetic substates, four are metastable (α_+, α_0, β_0, β_-) and are assumed stable for this work. The other four (e_+, e_0, f_0, f_-) have lifetimes of 1.6 ns corresponding to 100 MHz radiative widths. The α and β states are S states and have even parity, while the e and f states are P states and have odd parity. Due to parity conservation it is impossible to drive an electric dipole transition from one S state to another. One general way to drive an S-to-S transition is to apply a magnetic field of about 550 gauss and a DC electric field to mix β and e states. The new eigenstates no longer have a definite parity. However, if the Stark fields are small, the order of a few Volts/cm, it is possible to identify perturbed states, β_0', β_-', e_+', e_0'. The α states are only very slightly perturbed due to their large separation from the e and f states. Transitions can then be driven between α and β' states. If a β' state contains a finite population when the Stark fields are removed, the β states will also contain finite populations. Therefore, when the statement is made that the current work drives α to β transitions it signifies the above procedure.

In this work (see fig. 2.1), the source produces atoms in the α_+ and α_0 state, which enter an interaction region where they are driven to β_0 or β_-, and the β state is then detected in the detection region. Three transitions of interest are α_+-β_0, α_0-β_- and α_0-β_0 (see Appendix A for details). The probability to be in the final state is a few percent of the initial state for the α_+-$\beta_-$and α_0-β_-transitions. However, optimal transition rates for α_0-β_0 are the order of 4 ppm. Only the α_0-β_0 transition is sensitive to the weak coupling.

This experiment uses a 550 gauss magnetic field ($\vec{B}$) to get the e and β states to cross (Fig. 2.3). $\vec{B}$ defines the z axis. A static electric field ($\vec{E}$) of 2.2 volts/cm is applied perpendicular to $\vec{B}$ (defining $\hat{x}$) mixing e_+ with β_0. β_0 is also mixed with e_0 by the weak force forming $|\beta_0'\rangle = |\beta_0\rangle + \delta_S|e_+\rangle + \delta_W|e_0\rangle$. An rf-electric field ($\vec{\varepsilon}$) of 4.4 volts/cm at 1.5 GHz is applied in the plane formed by $\vec{E}$ and $\vec{B}$ at an angle ϕ (currently 5°) to $\vec{B}$. $\vec{\varepsilon}$ has two channels to drive a transition from α_0 to β'_0 (see figure 2.4). ε_x drives one channel from α_0 to β'_0, where β'_0 is formed by E_x mixing e_+ and β_0. ε_z drives the second channel from α_0 to β'_0, where β'_0 is formed by H^W mixing e_0 and β_0. Therefore, there are two amplitudes to be in the final state, one PC and PNC. These are the two amplitudes in equation 2.1.

The above is the popular interpretation of this experiment, but what this experiment really measures is not the amount of $|e_0\rangle$ mixed into $|\beta_0\rangle$ by the weak force, but the amount of $|e_0\rangle$ mixed into and in phase with $|\beta_0\rangle$, regardless of the origin. Therefore, what is measured is δ and not δ_W. Calling it δ_W is a matter of interpretation.

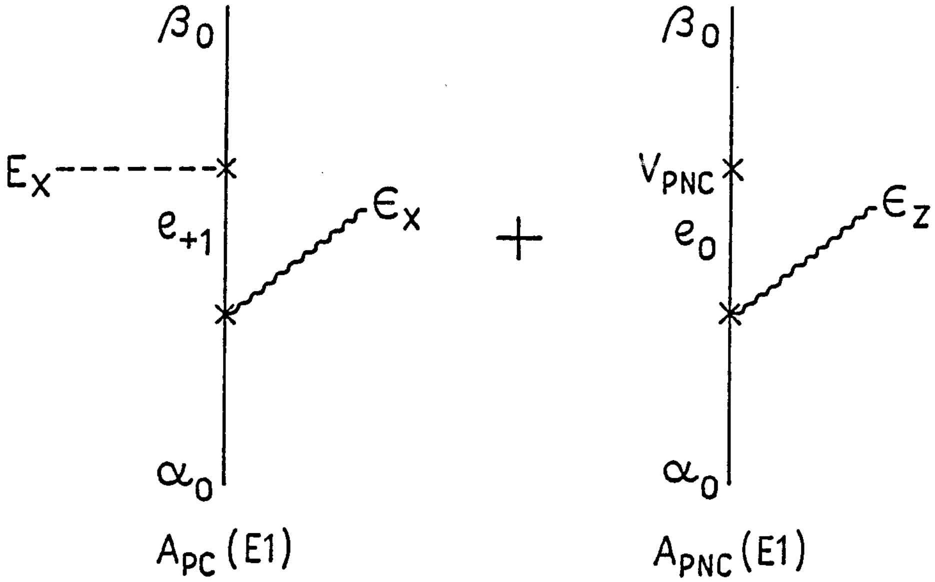

Figure 2.4 α_0-β_0 Transition

E.5 Details of the Parity Nonconserving α_0-β_0 Transition

The author knows of at least four different derivations of the α_0-β_0 transition amplitude, one due to R.W. Dunford[12] using perturbation theory and a formalism due to Lamb, a second one due to W.L. Williams[13] who solves the four-level problem by factoring a fourth order equation into two second order equations, a third due to G. Drake and L. Lévy[14] numerically integrating the Schrödinger equation, and a fourth due to G. Drake[15] which involves solving for the α_0-e_0 amplitude first, then treating the α_0-e_+-β_0 and α_0-e_0-β_0 amplitudes as perturbations. The latter approach is called the driven 3-level problem.

The numerical integration is by far the most accurate. However, to gain insight into the general features of the problem, the results of the driven 3-level problem will be presented. The transition probability for α_0 -β_0 is (see Appendix A),

$$|\beta_0|^2 = \frac{B^2(-2e^{-(\varepsilon + \gamma)\tau/z}\cos(w'\tau) + e^{-\gamma\tau} + e^{-\varepsilon\tau})}{\omega'^2 + \frac{(\gamma - \varepsilon)^2}{4}} \tag{2.16}$$

where B is dependent upon $\vec{E}$ and $\vec{\varepsilon}$, ε is the rf induced width of α_0, γ is the stark induced width of β_0, and ω' is the detuning from line center. In the limit of $\gamma = \varepsilon$ this reduces to

$$\tau^2 B^2 e^{-\gamma\tau} \frac{\sin^2(\omega'\tau/2)}{(\frac{\omega'\tau}{2})^2}. \tag{2.17}$$

Although simple, this formulation includes the Stark and rf broadening of the initial and final states, finite transit time effects, and ω' includes the rf and stark shifts. The optional transition rate at 545 Gauss occurs at $E = 2.2$ v/cm, $\tau = \frac{1}{3}$ μsec, and $\varepsilon = 4.4$ v/cm, $|\beta_0|^2_{opt} = 3.6\times10^{-6}$.

The general features of the transition are as follows. The problem is a four-level problem (α_0, β_0, e_+, e_0) and none of them can be ignored even in a first approximation. For optimal conditions the final distribution of populations is $\alpha_0 \cong 1/3$, $\beta_0 \cong 3.5$ ppm, ground (1S) state $\cong 2/3$. The PNC rate is so small (PNC = A×PC) it does not effect the PC rate and will be ignored for the rest of the discussion. The two predominant channels in this problem are $\alpha_0 \rightarrow e_+ \rightarrow n = 1$ and $\alpha_0 \rightarrow e_0 \rightarrow n = 1$. However, the PC rate is $\alpha_0 - \beta_0'$ ($\alpha_0 \rightarrow e_+ \rightarrow \beta_0$), and it is impossible to drive to β_0' without driving to e_+'. Even worse than this is that $\alpha_0 \rightarrow e_0 \rightarrow n = 1$ is a much stronger transition than either of the first two. When trying to populate β_0' most atoms transition to e_0 and, hence, n=1. What is good about this is that most atoms go through the e_0 state and give the weak interaction a chance to drive them to β_0, making the asymmetry larger.

The question arises as to why leave the population of $\alpha_0 = 1/3$? To completely depopulate α_0 would require using more rf power. Using more rf power means most of the population ending up in β_0' would be put there during the beginning of the interaction time, and since β_0' has a Stark-induced width, the initial population would have the rest of the interaction time to decay to n=1. If the rf power is turned down too much, not enough population gets into β_0'. Therefore, the compromise that is met is drive hard enough to populate β_0', but not so hard that the population has most of the interaction time to decay to the ground state.

The asymmetry is

$$A = \frac{4\overline{V}C_{2p}}{3ea_0E_x\theta\phi} \cong 3.1\times10^{-6}\ C_{2p} \tag{2.18}$$

The time required to achieve a given signal-to-noise ratio S/N is given by eq. 2.5. For this experiment $R_{PC} = |\beta_0|^2\eta\Omega I_0$ where η is the detector efficiency, Ω the detector solid angle, and I_0 the initial α_0 intensity in atoms/sec. For the current experimental configuration $\eta = 0.2\text{-}0.25$, $\Omega = 3/16$, and Lévy claims $I_0 = 10^{13}$ metastables per hyperfine component.[15] The integration time to achieve a S/N = 1 for $C_{2p} = 1$ is approximately 13 hours. The current experiment has high lying states cascading down resulting in a background 3 times R_{PC}. This lengthens 13 hours to 51 hours.

E.6 Role of Damping

The R_{PNC} term is proportional to the pseudoscalar invariant (see Chapter III) $\vec{\varepsilon}\cdot\vec{E}\ \vec{\varepsilon}\cdot\hat{B}$. The fact that this term is also formally T-odd raised the question of its observability. Transitions which involve states that are damped (can decay via photon emission to the ground state) but do not involve photon emission themselves result in the following conclusions.[16] The existence of a formally T-odd term is possible only as a result of the induced damping of the $2S_{1/2}$ substates. Such a term cannot be present in the probability for the atom to remain in the initial state α_0. It can occur in the transition probability to the observed final state β_0, if the initial populations of the α_0 and β_0 are different. These probabilities do not sum to unity even on resonance where β_0 is the only significant final state. Probability balance is maintained by the existence of a corresponding T-odd term of opposite sign in the sum over the other final states. In this case the other final states are in the radiative sector.

The problems with the T-odd pseudoscalar arise when people incorrectly calculate right and left eigenvectors in perturbation theory with Wigner-Weisskopf approximation. To do first order perturbation theory one proceeds as usual. For example, the mixing of the β_0 and e_+ states in an electric field results in the right eigenvector,

$$|\beta_0'\rangle = |\beta_0\rangle + |e_+\rangle \frac{V}{E_{\beta_0} - E_{e_+} + i\Gamma/2} . \qquad (2.19a)$$

The left eigenvector is

$$\langle \tilde{\beta}_o' | = \langle \beta_o | + \langle e_+ | \frac{V^*}{E_{\beta_o} - E_{e_+} + i\Gamma/2} \; . \qquad (2.19b)$$

Note that the denominator was not complex-conjugated. Whether the denominator of 2.19b is complex-conjugated or not leads to experimentally observable effects. An experiment proposed by Dunford[17] and performed by Lévy[18] verifies the correctness of this approach. Bell places the motivation for the above prescription on a firm theoretical basis.[19]

References for Chapter II

1. Michigan, University of Washington (Seattle), Yale.

2. L.P. Lévy, PhD dissertation, University of Michigan (1982) 209 unpublished (available from University Microfilms, Ann Arbor).

3. Ref. 2, pg. 229.

4. G.E. Harrison, M.A. Player, P.G.H. Sandars, J. Phys. E, Scientific Instruments 4, 750 (1971).

5. W.E. Lamb, Jr., R.C. Retherford, Phys. Rev. 79, 4 (1950), 549-572.

6. Ref. 2, pg. 237.

7. R.W. Dunford, PhD dissertation, University of Michigan (1978) 22 unpublished (available from University Microfilms, Ann Arbor).

8. W.L. Williams, private communication.

9. R.W. Dunford, R.R. Lewis, W.L. Williams, Phys. Rev. A, 18, 6 (1978) 2421-2436.

10. Ref. 2, pg. 27.

11. Ref. 7, pg. 15.

12. Ref. 7, pg. 58.

13. W.L. Williams, private communication.

14. G. Drake, University of Windsor, private communication.

15. Ref. 2, pg. 69.

16. L.P. Levy and W.L. Williams, Phys. Rev. Lett. 48, 101 (1982). The rest of this paragraph is quoted from aforementioned article.

17. Ref. 7, pg. 168.

18. Ref. 16.

19. J.S. Bell, Proceedings of the International Workshop on Neutral Current Interactions in Atoms, Cargese, 1979, ed. W.L. Williams.

CHAPTER III

INHOMOGENEOUS ELECTRIC FIELD LINESHAPES

A. Outline of the Approach Used to Evaluate Integrals over the Beam Cross Section for the Inhomogeneous Electric Field

This generation of the experiment forms the electric field in the interaction region by applying voltages to two closely spaced carbon-coated glass semicylinders. This work neglects the end effects of the tubes. This is believed to be reasonable, since for this type of boundary value problem the perturbations caused by finite tube length decay exponentially to zero with a decay constant the order of the tube inner diameter. The resulting electric field for infinitely long semicylinders is given by Jackson[1] as:

$$\vec{E} = -\frac{2V}{\pi b}\,\frac{1}{(1-\rho^2)^2 + 4\rho^2\cos^2\theta}\left\{(1+\rho^2)\cos\theta\,\hat{\rho} - (1-\rho^2)\sin\theta\,\hat{\theta}\right\}, \tag{3.1}$$

where V is the difference between the potentials applied to the semicylinders, b is the semicylinder inner radius, $\rho = r/b$ (where r, the radial distance from the cylinder axis, and b have units of length), and θ is measured from a plane perpendicular to the plane through the gap. In Cartesian coordinates (3.1) becomes,

$$\vec{E} = -\frac{2V}{\pi b}\,\frac{\{1 - (\sigma^2-\chi^2)\}\hat{x} + 2\sigma\chi\hat{y}}{1 + (\sigma^2+\chi^2)^2 - 2(\sigma^2-\chi^2)}, \tag{3.2}$$

where $\sigma = \rho\sin\theta$ and $\chi = \rho\cos\theta$. This electric field is plotted in figure 3.1.

This electric field has significant inhomogeneities across the beam. For a beam diameter one half the electric field electrode diameter, the square of the ratio of the maximum electric field to the minimum electric field, at maximum beam diameter, is 2.7. This was expected to cause large changes in the lineshape compared to the uniform electric field case. This is not the case.

The following outlines the procedure used to perform integrals over the beam cross section where the complicated electric field makes it difficult to do the integrals in closed form.

We start with the lineshape function given in Appendix A, equation (42),

$$|\beta(\omega',\tau)|^2 = e^{-(\varepsilon+\gamma)\tau/2}\ |\cos\theta_2|^2 | \int_{-\tau/2}^{\tau/2} B\ e^{(\gamma-\varepsilon)t/2}\ e^{-i\omega' t}\ dt|^2\ . \tag{3.3}$$

Since the variations in the dc electric field are large, γ, B, and ω' must be considered to be functions of E_x and E_y. Assuming B is not a function of time, it may be factored out of the integral, and the integral performed by elementary means. This results in the following general form for the average over the beam,

$$\frac{1}{A}\int_A |\beta|^2 dA = \frac{1}{\pi\rho_0^2}\int_0^{\rho_0} \rho d\rho \int_0^{2\pi} d\theta\ f(E_x,E_y) \tag{3.4}$$

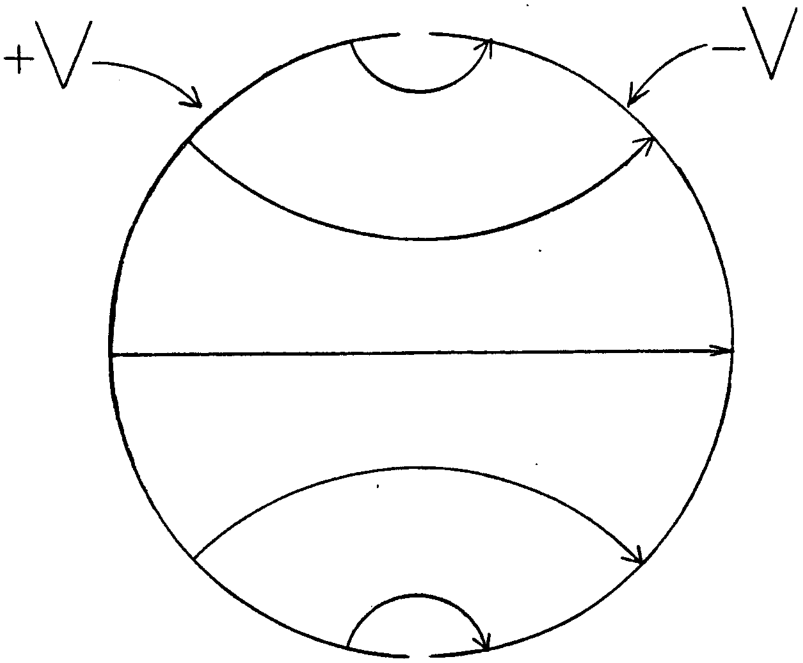

Figure 3.1 Electric Field Due to Closely Spaced Semicylinders

where f is a complicated function of E_x and E_y. This integral is expanded in a Taylor series in two variables, E_x and E_y, about $E_x = E_x(\rho=0) = E_o$ and $E_y = E_y(\rho=0) = 0$, resulting in,

$$\frac{1}{\pi\rho_o^2}\int_0^{\rho_o}\rho d\rho\int_0^{2\pi}d\theta\{f(E_o,0) + f_{E_x}(E_o,0)(E_x-E_o) + f_{E_y}(E_o,0)(E_y)$$

$$+\frac{1}{2}f_{E_xE_x}(E_o,0)(E_x-E_o)^2 + \frac{1}{2}f_{E_yE_y}(E_o,0)(E_y)^2$$

$$+ f_{E_xE_y}(E_o,0)(E_x-E_o)(E_y) + \ldots\} \tag{3.5}$$

where

$$f_{E_x}(E_o,0) = \left.\frac{\partial f(E_x,E_y)}{\partial E_x}\right|_{\substack{E_x=E_o\\E_y=0}}, \text{ etc.}$$

Expanding about $E_x = E_o$ and $E_y = 0$ results in rapid series convergence for two reasons. First, these are the average values of the electric fields over a circle centered on $\rho=0$, the electrode center. Second, the first term in the expansion, $f(E_o,0)$, is the only nonzero term for the homogeneous electric field case, and the remaining terms are only nonzero if the electric field contains inhomogeneities. Thus the solution has a lineshape term due to the average value of the electric field across the beam plus lineshape terms due to electric field inhomogeneities.

Since the derivatives of f are evaluated at specific values of E_x and E_y they may be factored out of the integral, leaving only integrals over powers of electric field inhomogeneities to be performed. The dependence of the transition rate on all the fields is contained in the derivatives. Therefore, a separation of the physical and the alignment variables is achieved. Thus, the calculation of the entire lineshape as a function of magnetic field, for each term in (3.5), requires the evaluation of one integral over the electric field, evaluation of an expression which is only a function of magnetic and electric fields, but not the alignment variables, and multiplication of the two together.

E_x and E_y are then expanded in a Taylor series in ρ about $\rho=0$ resulting in,

$$E_x = \frac{2V}{\pi b}\left\{-1 + \rho^2\cos(2\theta) - \rho^4\cos(4\theta) + \ldots\right\}$$

$$E_y = \frac{2V}{\pi b}\left\{-\rho^2\sin(2\theta) + \rho^4\sin(4\theta) - \rho^6\sin(6\theta) + \ldots\right\} \tag{3.6}$$

The radius of convergence is $\rho < 1$. The resulting integrand is a power series in positive integer powers of ρ, trivially integrable.

All calculations involving the power series for E_x and E_y are done through tenth order in ρ. However, the Taylor series of f in E_x and E_y is very involved since the number of terms in the derivatives of f increases rapidly with increasing order.

To handle the complexities in the derivatives of f, the following approach was developed. Let $f = f_N/f_D$, where f_N and f_D are the numerator and denominator, respectively, of f. Partial derivatives of f_N and f_D with respect to E_x and E_y are then derived and evaluated numerically at $E_x = E_0$ and $E_y = 0$. The quotient rule is applied to f_N/f_D in a formal sense, i.e., if f_x is desired, $f_x = \dfrac{f_D f_{Nx} - f_{Dx} f_N}{(f_D)^2}$ is formed. Then numerical values for f_D, f_N, f_{Dx}, and f_{Nx} are substituted into the formula for f_x. This can be extended to any order of partial derivative required for the Taylor series expansion of f, limited only by how complicated the derivatives of f_N are allowed to become.

B. Lineshapes for the Ideal Case

The ideal case is defined as that of no misalignments of the fields or beam, and no beam divergence. This is called the "all-aligned" case. Figure 3.2 is a plot of the α_0-β_0 transition for the all-aligned, uniform electric field case compared to the electric field produced by ideal tubes in the all-aligned case. The transition rates are optimized with respect to the dc and rf electric fields. The effect of the inhomogenous electric field on the lineshape is small. To understand this one must study two features of the solution (equ. 3.5). Both of these features are conveniently separated.

Table 3.1 gives the integrals for the all-aligned case with the ideal electrodes. The integrals are of the form,

$$\frac{1}{A}\int_A [E_x(\rho) - E_0]^n[E_y(\rho)]^m dA = \frac{1}{A}\int_A [\Delta E_x]^n[\Delta E_y]^m \quad . \qquad (3.7)$$

In the interval $[0,2\pi]$, ΔE_x is even about π, and ΔE_y is odd about π. Therefore, any integrals where m is odd must be zero. Since ΔE_x and ΔE_y are the sum of harmonic functions in the interval $[0,2\pi]$ the integrals in the n=0, m=1 and n=1, m=0 cases are zero. However, for ΔE_x, the sum of the harmonic functions is not harmonic. Therefore, the n=3, m=0 case is nonzero. The ρ_0^8 term for the n=3, m=0 case in Table 3.1 occurs as the product of two 2θ-terms and one 4θ-term. Requiring that the θ products result in a dc term explains the powers of ρ in other terms also, i.e., in squaring (n=0,m=2), the only dc terms are of

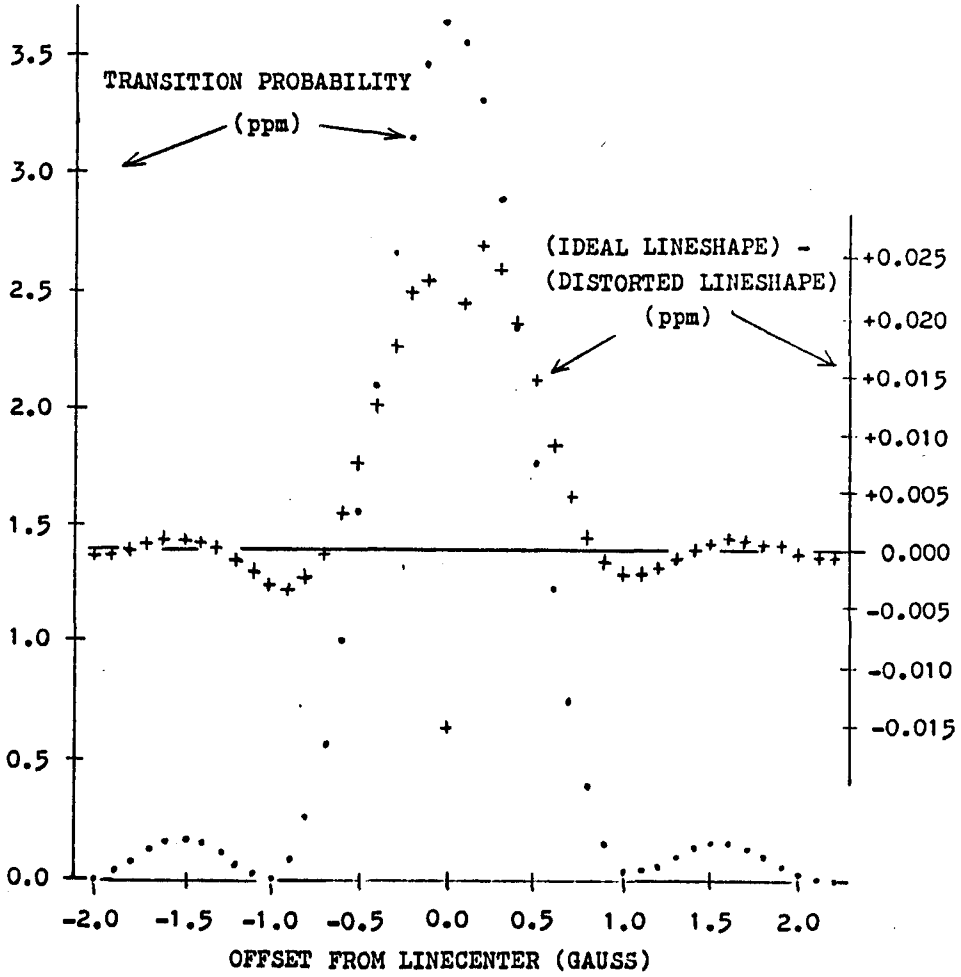

Figure 3.2 Distortions to Lineshapes Caused by Semicylinder Electrodes

Table 3.1
Integrals over Electric Field Inhomogeneities for the All Aligned Case

Integrals are of the form:

$$\frac{1}{A}\int_A [E_x(\rho) - E_x(\rho=0)]^n[E_y(\rho) - E_y(\rho=0)]^m \, dA$$

n	m	Integral $\left(E_x(\rho=0) = 2V/\pi b,\ E_y(\rho=0) = 0\right)$
0	0	1
0	1	0
0	2	$(\frac{2V}{\pi b})^2(\frac{1}{6}\rho_o^4 + \frac{1}{10}\rho_o^8)$
0	3	0
0	4	$(\frac{2V}{\pi b})^4(\frac{3}{40}\rho_o^8)$
1	0	0
1	1	0
1	2	$(\frac{2V}{\pi b})^3(-\frac{1}{20}\rho_o^8)$
1	3	0
2	0	$(\frac{2V}{\pi b})^2(\frac{1}{6}\rho_o^4 + \frac{1}{10}\rho_o^8)$
2	1	0
2	2	$(\frac{2V}{\pi b})^4(\frac{1}{40}\rho_o^8)$
3	0	$(\frac{2V}{\pi b})^3(-\frac{3}{20}\rho_o^8)$
3	1	0
4	0	$(\frac{2V}{\pi b})^4(\frac{3}{40}\rho_o^8)$

the form $(\sin n\theta)^2$. The ρ_0^4 term is from ρ^2 and the ρ_0^8 term is from ρ^4. Similarly, the presence of all other terms can be understood.

Unfortunately, there is no easy interpretation of the derivatives. First, they are functions of all three fields in the problem. If both electric fields are fixed, to optimize the transition rate for example, their dependence on the magnetic field still remains. Although it is possible to understand the behavior of the first and maybe the second derivatives, the third and fourth derivatives contain little physical content. Frequently, although not always, the first order integrals are zero, canceling the easiest-to-understand derivative. Fortunately, the derivatives never get large enough so that when multiplied by the small quantity $(\rho_0 = 1/2)^N$, they cause any sizeable effect on the line shape. With the exception of the zeros of the original line shape, the differences caused by inhomogenous electric fields is at most 2% of the original transition rate.

C. Effects of Misalignments and Non-Ideal Electrodes

Extensive calculations accounting for the effect of inhomogeneous electric fields in the following cases has been completed: 1) x and y offset of beam with respect to electrode axis, 2) rotation of beam and electrodes with respect to Zeeman axis in the xz and xy planes, 3) rotation of just the beam with respect to Zeeman axis in the xz and xy planes, 4) rotation of the electrode about its cylinder axis, 5) rotation of the electrodes and beam in the xy plane and rotation of the electrodes about their cylinder axis. All cases include the effects of beam divergence and are performed for the $\alpha_+-\beta_0$ and $\alpha_0-\beta_0$ transitions. Case 1 is discussed in Chapter IV for the $\alpha_0-\beta_0$ transitions. The other cases are not described in this work.

The discussion of the electric field electrodes has assumed that they are ideal semicylinders. Any complete analysis of the electrodes must include all of their possible physical imperfections. Due to time constraints the author has not investigated the consequences of physical imperfections. However, they are listed here for future consideration. The electrode inside diameter can vary. In principle, the axes of the two semicylinders should lie on the same line. In practice they will be offset in both the x and y directions and rotated in the xz and yz planes. Variation of the inner diameter, and both rotations result in z applied electric fields, a serious consideration for this experiment.

CHAPTER IV

SYSTEMATICS

A. Invariant Analysis

The transition rate can be decomposed into the sum of powers of scalar and pseudoscalar terms composed of the relevant physical variables.[1] The possible terms in this decomposition are derived by requiring that any term appearing be rotationally invariant, hence the term invariant analysis. Dukes, Kwong, and Lewis[2] have completed an invariant decomposition for the parity experiment. Their analysis includes the dc electric field $\vec{E}$, dc magnetic field $\vec{B}$, ac rf electric field $\vec{\varepsilon}$, and ac rf magnetic field $\vec{b}$. The results are given in Table 4.1. There is more than one way to do the vector decomposition of the rate, all ways are equivalent of course. The advantage of the decomposition used in Table 4.1 is that the fields are separated into the more intuitive longitudinal $(\hat{z})$ and transverse components $(\hat{x},\hat{y})$. The dependence of the rate on the magnitude of $\vec{B}$ is contained in the coefficients.

Invariant analysis is useful for placing limits on misalignments between the desired applied fields $\vec{E}$, $\vec{B}$, and $\vec{\varepsilon}$, limits on the allowable size of the undesired applied field $\vec{b}$, motional electric fields due to beam divergence or misalignment of the average beam velocity with the Zeeman axis, and stray electric fields.

Invariant analysis is used to identify unwanted parity conserving (PC) interference terms which reverse sign under reversal of the interaction region handedness, as does the wanted parity nonconserving (PNC) term. For example, assume the electric field $\vec{E}$ in (4.2) is the sum of an applied electric field in the $\hat{x}$ direction, $E \;\; = E_A^x\hat{x}$, and a motional electric field due to misalignment of the magnetic field $\vec{B}$ and the beam velocity $\vec{v}$ in the yz plane, $\vec{E}_M = E_M^x\hat{x}$. Insertion into the G_1 term results in

$$G_1(\vec{\varepsilon}\times\hat{B})^2((\vec{E}_A + \vec{E}_M) \times \hat{B})^2 = G_1(\vec{\varepsilon}\times\hat{B})^2((E_A^x)^2 + (E_M^x)^2 + 2E_A^xE_M^x) \; . \tag{4.6}$$

Ideally, the reversal of $\vec{E}_A$ only changes the rate via the PNC term J_2. However, (4.6) contains an interference term $2E_A^xE_M^x$ which changes sign under reversal of $\vec{E}_A$, thus changing the rate. The change in the rate due to $G_1E_A^xE_M^x$ must be reduced sufficiently so as not to mask the PNC term. By knowing the size of the invariant coefficients, $G_1,\ldots G_8$, it is possible to determine the allowable size of E_M^x, and the accuracy with which the B and ϕ reversals must be performed. By analysis of all such terms it is possible to set limits on the size of all misalignments and the required accuracy of the three reversals.

Although Dunford[3] discusses an invariant analysis of the α_0-β_0 transition for applied dc electric fields, the current generation of experiment does not correlate the $\vec{E}$ and $\hat{\phi}$ flips to the extent he did, and transverse inhomogeneities in $\vec{E}$ introduces new alignment requirments. Therefore, the invariant analysis for applied dc electric fields is repeated.

The invariant decomposition in Table 4.1 is not complete. It is only valid to lowest order in the fields. It predicts $|A_E|^2 \sim |\vec{E}|^2|\vec{\varepsilon}|^2$ obviously false, since the $\alpha_0\beta_0$ transition rate peaks at $|\vec{E}| \sim$ 2.5 V/cm, $|\vec{\varepsilon}| \sim$ 4.5 V/cm. The decomposition is valid only for small fields, $|\vec{E}| \sim |\vec{\varepsilon}| <$ 1 V/cm. This is important since this lowest order invariant analysis is used to determine required equipment performance. For example, the $|A_E|^2$ rate is 25 times more sensitive to a $\hat{x}$ motional electric field of 16 mV (1000 μrad tilt of $\vec{B}$) when $|\vec{E}|$ = 1 V/cm than when $|\vec{E}| = |\vec{E}|_{optimal} \cong 2.5$ V/cm.

B. Classification of Invariants

Misalignments in this experiment can divided into two general classes: one arising from misalignments between fields, and one arising from misalignments of the beam with respect to the fields. There are also three subclasses of problems; tilts, offsets, and deviations of the beam from cylindrical symmetry. The beam can be offset, and/or tilted with respect to the interaction region, and not cylindrically symmetric. The fields can be tilted and offset with respect to each other. The latter condition may not be so obvious, but the position of the electrodes with respect to the cavity endcaps is important since the electrodes distort the microwave electric field that diverges in the endcaps. Also, since $\vec{B}$ is generated with a finite length solenoid, $\vec{B}$ diverges, creating radial components of magnetic field, resulting in an atom transversing the interaction region experiencing motional electric fields. The following is an invariant analysis including all possible tilts of the fields with respect to each other and offsets of the beam with respect to $\vec{E}$.

The results of the lineshape theory developed in Chapter III is that the effect of the inhomogeneous electric field are important when considering offsets of the beam with respect to the electrode center and the cylindrical symmetry of the beam. Determining the size of the latter two effects requires a beam average be performed. The following invariant analysis is performed by beam averaging (4.2). For terms neglecting beam divergence the beam average is trivial. Cases accounting for interference between the motional electric field due to beam divergence and the inhomogeneities in the applied electric field require use of the inhomogeneous electric field lineshape theory.

C. Invariant Analysis Neglecting Beam Divergence

$\vec{E}$ in (4.2) is the total electric field experienced by the atom. This electric field arises from three different types of sources; the electric field from the electrodes, $\vec{E}_A$; the motional electric field due to misalignments of the average beam velocity with the magnetic field, $\vec{E}_M$; and the electric field due to stray sources, $\vec{E}_S$. Possible sources of stray electric fields are nonconductive patches on the electric field electrodes collecting electric charge, and the electric field from other origins in the apparatus (β-quench, detection region, see Chapter V), entering the interaction region. This analysis assumes all fields are constant throughout the interaction region. This is incorrect for all of the mentioned sources of $\vec{E}_S$, but does provide insight into allowable limits.

Substitution of $\vec{E} = \vec{E}_A + \vec{E}_M + \vec{E}_S$ into $|A_E|^2$ results in 81 terms for the α_0-β_0 transition. Six of these terms flip sign under all three reversals, 24 terms flip sign under only two of the reversals, and 41 terms flip sign under only one of the reversals. This analysis assumes that the different reversals cause $\vec{E}_A \rightarrow -\vec{E}_A$, $\beta \rightarrow -\beta$, and $\varepsilon_x \rightarrow -\varepsilon_x$, $\varepsilon_y \rightarrow -\varepsilon_y$, and $\varepsilon_z \rightarrow \varepsilon_z$. This approach is believed to be reasonably accurate for all but the ε_y case. It is over-generalized since ε_y can be set equal to zero without loss of generality. However, once the ϕ reversal is performed, ε_y is no longer zero in the old coordinate system. Though possible to keep ε_y zero by rotating the coordinate system, this may be more trouble than it is worth, and it is unphysical. Regardless of how ε_y is defined before the ϕ reversal, its value afterwards is completely unpredictable.

Table 4.2 gives a selected set of misalignments and reversal accuracies. Table 4.3 lists the largest systematics using the values in table 4.2. The values in table 4.2 are adjusted so that the largest PC/PNC ratios in table 4.3 are close to unity.

D. Effects of Interference Between Motional Electric Field from Beam Divergence and Inhomogeneous Applied Electric Fields

Interference between the motional electric field due to beam divergence and the inhomogeneities in the applied electric field of the electrodes restricts the alignment of the beam with respect to the electrode center, and the cylindrical symmetry of the beams initial state population. Assuming the beam diverges from a point source in a uniform magnetic field, results in a motional electric field,

$$\vec{E}_M = 300\,\frac{v}{c}\,(-\hat{v}\cdot\hat{B})\Phi_o\,\frac{\rho}{\rho_o}\,\hat{\phi} = D\rho\hat{\phi}\ , \tag{4.7}$$

where Φ_o is the maximum beam divergence,[4] ρ_o is the beam diameter, $\hat{v}$ and $\hat{B}$ are parallel or antiparallel, B in gauss, and $\vec{E}_M$ in volts/cm.

Table 4.4 lists those terms which can possibly restrict beam/electrode alignment once a beam average is completed. The first and seventh entries are of the form $\vec{E}_A\cdot\vec{E}_M$, and can be shown to be zero irrespective of the form of $\vec{E}_A$. Averaging over the beam results in

$$\frac{1}{\pi\rho_o^2}\int_o^{\rho_o}\rho d\rho\int_o^{2\pi}d\phi\ \vec{E}_A\cdot\vec{E}_M\ . \tag{4.8}$$

Substituting the explicit form of $\vec{E}_M = D\rho\hat{\phi}$,

$$\frac{k}{\pi\rho_o^2}\int_o^{\rho_o}\rho^2 d\rho\int_o^{2\pi}d\phi\ E_A^{\phi} \tag{4.9}$$

Note the form of the ϕ integral,

$$\int_o^{2\pi} E_A^{\phi}\,d\phi \tag{4.10}$$

Comparing (4.10) to the result of applying Stoke's theorem to one of Maxwell's equations in the static case,

$$\int_S(\vec{\nabla}\times\vec{E})\cdot\hat{n}da = \int_C \vec{E}\cdot d\vec{\ell} = 0\ , \tag{4.11}$$

and choosing $d\vec{\ell} = \rho_o\hat{\phi}$ results in,

$$\rho_o \int_o^{2\pi} E^\phi \, d\phi = 0 \, . \qquad (4.12)$$

Equation 4.12 is identical to (4.10), therefore, due to the form of $\vec{E}_M$ from a diverging beam, (4.8) is zero regardless of the shape of $\vec{E}_A$. Equation 4.8 tells us that $E_A^x E_M^x = -E_A^y E_M^y$. Since these terms are required individually, this is a useful internal consistency check. Table 4.4 contains only four unique terms that must be evaluated, $E_A^x E_M^x$, $E_A^y E_M^x$, $E_A^x E_M^y$, $E_A^y E_M^y$. E_A^z is a linear combination of the x and y fields due to the electrodes being rotated with respect to the Zeeman axis. Therefore, nothing new needs to be evaluated for the E_A^z cases.

The beam and electrodes can be misaligned in a combination of the x and y directions. Since the effects of these offsets are small (although important) they will be treated separately. Figure 4.1 shows both offsets and the relevant integrals. Using only the symmetries and not the relative magnitudes or exact shape of the motional and applied electric fields, it is possible to determine the nonzero integrals. The nonzero integrals have been evaluated by approximating the integrand $O(\rho^{11}, x_o^2, y_o^2) = 0$. The integrals for x and y offsets are given in tables 4.5 and 4.6 respectively. The terms of interest are,

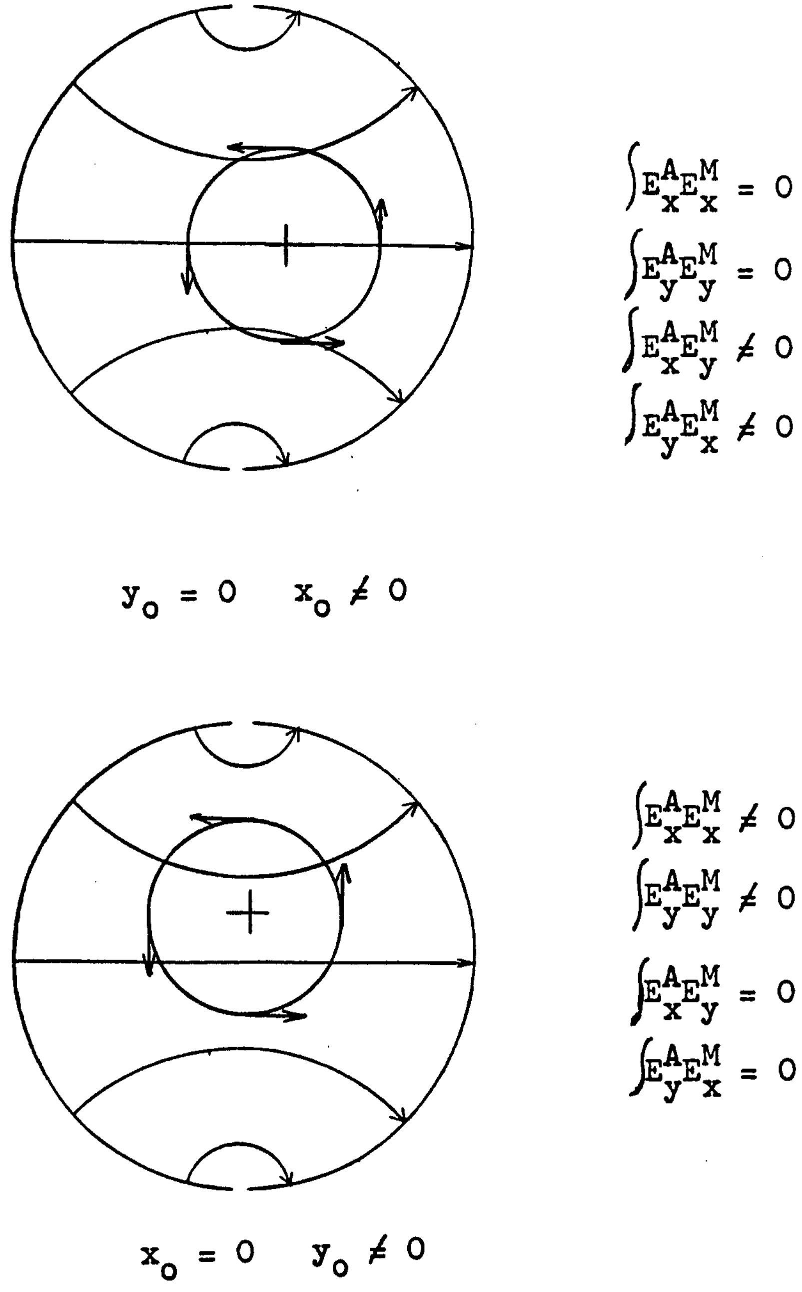

$\int E_x^A E_x^M = 0$

$\int E_y^A E_y^M = 0$

$\int E_x^A E_y^M \neq 0$

$\int E_y^A E_x^M \neq 0$

$y_o = 0 \quad x_o \neq 0$

$\int E_x^A E_x^M \neq 0$

$\int E_y^A E_y^M \neq 0$

$\int E_x^A E_y^M = 0$

$\int E_y^A E_x^M = 0$

$x_o = 0 \quad y_o \neq 0$

Figure 4.1 Interference of Motional Electric Field Due to Beam Divergence and dc Electric Field Inhomogeneities

$$\left.\begin{array}{l} x_0 \neq 0 \\ y_0 = 0 \end{array}\right\} \quad \begin{array}{l} \int E_A^x E_M^y = \frac{DV}{b\pi} \rho_o^2 x_o \\ \int E_A^y E_M^x = \frac{DV}{b\pi} \rho_o^2 x_o \end{array}$$

$$\left.\begin{array}{l} x_0 = 0 \\ y_0 \neq 0 \end{array}\right\} \quad \begin{array}{l} \int E_A^x E_M^x = - \frac{DV}{b\pi} \rho_o^2 y_o \\ \int E_A^y E_M^y = \frac{DV}{b\pi} \rho_o^2 y_o \end{array} \qquad (4.13)$$

Requiring the entries in table 4.4 be less than or equal to the PNC term results in,

$$x_0 < 1.56\times10^{-4}$$

$$y_0 < 1.65\times10^{-3}$$

The current electrodes have a 6 mm inner radius, yielding

$$bx_0 = 9.25\times10^{-5}\ \text{cm} \quad (36\ \mu\text{inch})$$

$$by_0 = 9.9\times10^{-4}\ \text{cm} \quad (390\ \mu\text{inch})$$

Table 4.1

Invariant Analysis of Rate to Lowest Order in the Fields

$$|A_M|^2 = F_1(\vec{b}\times\hat{B})^2 + F_2(\vec{b}\cdot\hat{B})^2 \qquad \text{(equ. 4.1)}$$

$$\begin{aligned}|A_S|^2 = {} & G_1(\vec{\varepsilon}\times\hat{B})^2(\vec{E}\times\hat{B})^2 + G_2(\vec{\varepsilon}\times\hat{B}\cdot\vec{E}\times\hat{B})^2 \\ & + G_3(\vec{\varepsilon}\cdot\hat{B})^2(\vec{E}\times\hat{B})^2 + G_4(\vec{\varepsilon}\times\hat{B})^2(\vec{E}\cdot\hat{B})^2 \\ & + G_5(\vec{\varepsilon}\cdot\hat{B})^2(\vec{E}\cdot\hat{B})^2 + G_6(\vec{\varepsilon}\cdot\hat{B})(\vec{E}\cdot\hat{B})(\vec{\varepsilon}\times\hat{B}\cdot\vec{E}\times\hat{B}) \\ & + G_7(\vec{\varepsilon}\cdot\hat{B})(\vec{E}\cdot\hat{B})(\vec{\varepsilon}\times\vec{E}\cdot\hat{B}) + G_8(\vec{\varepsilon}\times\hat{B}\cdot\vec{E}\times\hat{B})(\vec{\varepsilon}\times\vec{E}\cdot\hat{B})\end{aligned} \qquad \text{(equ. 4.2)}$$

$$\begin{aligned}(A_M A_S^* + cc) = {} & H_1(\vec{\varepsilon}\cdot\hat{B})(\vec{b}\cdot\hat{B})(\vec{E}\cdot\hat{B}) + H_2(\vec{\varepsilon}\times\hat{B}\cdot\vec{b}\times\hat{B})(\vec{E}\cdot\hat{B}) \\ & + H_3(\vec{\varepsilon}\times\hat{B}\cdot\vec{E}\times\hat{B})(\vec{b}\cdot\hat{B}) + H_4(\vec{\varepsilon}\cdot\hat{B})(\vec{b}\times\hat{B}\cdot\vec{E}\times\hat{B}) \\ & + H_5(\vec{\varepsilon}\times\vec{b}\cdot\hat{B})(\vec{E}\cdot\hat{B}) + H_6(\vec{\varepsilon}\times\vec{E}\cdot\hat{B})(\vec{b}\cdot\hat{B}) + H_7(\vec{b}\times\vec{E}\cdot\hat{B})(\vec{\varepsilon}\cdot\hat{B})\end{aligned} \qquad \text{(equ. 4.3)}$$

$$\begin{aligned}(A_S A_W^* + cc) = {} & J_1(\vec{\varepsilon}\times\hat{B})^2(\vec{E}\cdot\hat{B}) + J_2(\vec{\varepsilon}\cdot\hat{B})(\vec{\varepsilon}\times\hat{B})\cdot(\vec{E}\times\hat{B}) \\ & + J_3(\vec{\varepsilon}\cdot\hat{B})(\vec{\varepsilon}\times\vec{E}\cdot\hat{B}) + J_4(\vec{\varepsilon}\cdot\hat{B})^2(\vec{E}\cdot\hat{B})\end{aligned} \qquad \text{(equ. 4.4)}$$

$$(A_M A_W^* + cc) = k_1(\vec{\varepsilon}\times\hat{B}\cdot\vec{b}\times\hat{B}) + k_2(\vec{\varepsilon}\times\vec{b}\cdot\hat{B}) + k_3(\vec{\varepsilon}\cdot\hat{B})(\vec{b}\cdot\hat{B}) \qquad \text{(equ. 4.5)}$$

Table 4.2

Field and Invariant Coefficients Values for α_0-β_0 at 540 gauss

	Angular Dependence[1]	Limits on Angular Value
$\vec{B} = (540\ \text{gauss})\hat{z}$		
$\lvert\vec{\varepsilon}\rvert = 1.0$		
$\varepsilon_x = 0.0871$		
$\varepsilon_y = 0.001$		
$\varepsilon_z = 0.996$		
$E_A^x = 1.0$		
$E_A^y = 0.0011$	$\sin\gamma\ \cos\alpha$	$\gamma < 1100\ \mu\text{rad}$
$E_A^z = 0.0001$	$\cos\gamma\ \sin\alpha$	$\alpha < 100\ \mu\text{rad}$
$E_M^x = 0.00015$	$\sin\chi$	$\chi < 0.27\ \mu\text{rad}$ (for $\lambda = \pi/2,\ 3\pi/2$)
$E_M^y = 0.1$	$\sin\chi$	$\chi < 185\ \mu\text{rad}$ (for $\lambda = 0,\ \pi$)
$E_S^x = 0.011$		
$E_S^y = 0.001$		
$E_S^z = 5.0\times10^{-5}$		
Accuracy of E, B, and ϕ reversals = 1%		
$G_1 = 3.63$		
$G_2 = 0.0383$		
$G_3 = 0$		
$G_4 = 0$		
$G_5 = 8.56$		
$G_6 = -9.77$		
$G_7 = -4.14$		
$G_8 = -0.818$		
$J_2\overline{V} = -6.83\times10^{-7}$ $(J_2\overline{V}\ \vec{\varepsilon}\cdot\hat{B}\vec{\varepsilon}\cdot\vec{E} = 5.9\times10^{-8})$		

[1] See footnote 4 for angle definition.

Table 4.3

Important Invariants Neglecting Beam Divergence

Invariant Term	Change Sign Under Listed Reversals	Value of PC Invariant Term / Value of PNC Invariant Term
$G_6\varepsilon_x\varepsilon_z E_A^z E_M^x$	EBϕ	0.215
$G_6\varepsilon_y\varepsilon_z E_A^z E_M^y$		1.64
$G_7\varepsilon_x\varepsilon_z E_A^z E_S^y$		0.606
$G_7\varepsilon_y\varepsilon_z E_A^x E_S^z$		0.348
$G_1 2\varepsilon_x^2 E_A^x E_M^x$	EB	-1.39
$G_1 2\varepsilon_x^2 E_A^y E_M^y$		-1.02
$G_2 2\varepsilon_x\varepsilon_y E_A^x E_M^y$		-0.113
$G_8\varepsilon_x^2 E_A^x E_S^y$		1.05
$G_6\varepsilon_x\varepsilon_z E_A^x E_S^z$	Eϕ	0.715
$G_6\varepsilon_x\varepsilon_z E_A^z E_S^x$		0.157
$G_7\varepsilon_x\varepsilon_z E_A^z E_A^y$		0.606
$G_1 2\varepsilon_x^2 E_A^x E_S^x$	E	-1.02
$G_6\varepsilon_x\varepsilon_z E_A^x E_A^z$		0.143
$G_8\varepsilon_x^2 E_A^x E_M^y$		1.05

Only those terms where the ratio of (PC invariant)/(PNC invariant) is greater than 1/10 are listed.

Table 4.4

Invariants for Interference Between Beam Divergence and Electric Field Inhomogeneities

$$2G_1(\varepsilon_x^2 + \varepsilon_y^2)(E_A^x E_M^x + E_A^y E_M^y) \equiv 0$$

$$2G_2\varepsilon_x\varepsilon_y(E_A^x E_M^y + E_A^y E_M^x)$$

$$2G_2\varepsilon_x^2 E_A^x E_M^x$$

$$2G_2\varepsilon_y^2 E_A^y E_M^y$$

$$G_7\varepsilon_x\varepsilon_z E_A^z E_M^y$$

$$G_7\varepsilon_y\varepsilon_z E_A^z E_M^x$$

$$2G_8\varepsilon_x\varepsilon_y(E_A^x E_M^x + E_A^y E_M^y) \equiv 0$$

$$G_8(\varepsilon_x^2 + \varepsilon_y^2)(E_A^x E_M^y + E_A^y E_M^x)$$

Table 4.5
Integrals for the Interference of Motional Electric Fields Due to Beam Divergence and Electric Field Inhomogeneities for Relative Displacements in the X Direction

Integrals are of the form:

$$\frac{1}{A}\int_A \left[E_x^A(\rho) - E_x^A(\rho=0) + E_x^M(\rho)\right]^n\left[E_y^A(\rho) - E_y^A(\rho=0) + E_y^M(\rho)\right]^m dA$$

n	m	Integral
0	0	1
0	1	0
0	2	$(\frac{2V}{\pi b})^2(\frac{1}{6}\rho_o^4 + \frac{1}{10}\rho_o^8) + \frac{1}{4}D^2$
1	0	0
1	1	0
2	0	$(\frac{2V}{\pi b})^2(\frac{1}{6}\rho_o^4 + \frac{1}{10}\rho_o^8) + \frac{1}{4}D^2$

$D = 300\,(v_B/c)B\Phi_0/\rho_0$

D	mks volts due to beam divergence
v_B	beam velocity
c	speed of light
B	magnetic field value in gauss
Φ_0	maximum angle in rads that a cylindrically symmetric beam diverging from a point source makes with the average beam velocity
x_0	(tube displacement along x axis)/(tube inner radius)

Table 4.6

Integrals for the Interference of Motional Electric Fields Due to Beam Divergence and Electric Field Inhomogeneities for Relative Displacements in the Y Direction

Integrals are of the form:

$$\frac{1}{A}\int_A [E_x^A(\rho) - E_x^A(\rho=0) + E_x^M(\rho)]^n[E_y^A(\rho) - E_y^A(\rho=0) + E_y^M(\rho)]^m dA$$

n	m	Integral
0	0	1
0	1	0
0	2	$(\frac{2V}{\pi b})^2(\frac{1}{6}\rho_o^4 + \frac{1}{10}\rho_o^8) + (\frac{2V}{\pi b})(-Dy_o\rho_o^2) + \frac{1}{4}D^2$
1	0	0
1	1	0
2	0	$(\frac{2V}{\pi b})^2(\frac{1}{6}\rho_o^4 + \frac{1}{10}\rho_o^8) + (\frac{2V}{\pi b})(+Dy_o\rho_o^2) + \frac{1}{4}D^2$

y_o (tube displacement along y axis)/(tube inner radius)

References for Chapter IV

1. H. Weyl, The Classical Groups, Chapter 2, (Princeton University Press, 1946); G.F. Temple, Cartesian Tensors: An Introduction, (Wiley, New York, 1960).

2. C. Dukes, H. Kwong, and R.R. Lewis, internal report, 1977 (unpublished).

3. R.W. Dunford, PhD dissertation, University of Michigan, 1978 (available from University Microfilms, Ann Arbor, MI).

4. L.P. Lévy and W.L. Williams, Parity Nonconservation in the Hydrogen Atom III, Phys. Rev. A 30, 220 (1984).

CHAPTER V

APPARATUS

A. Apparatus Overview

Figure 5.1 is a general block diagram of the experimental apparatus. The source produces a beam of hydrogen in the n=2 state. The beam is then collimated and passes through the beta quench region where the final (β_0) state is depopulated by quenching in a dc electric field. It then enters the interaction region where the atoms in the initial state (α_0) are driven to the final state via a combination of dc magnetic, dc electric, and rf electric fields. The dc magnetic field is generated by the solenoid, the dc electric field by the glass electrodes, and the rf electric field by the interaction cavity. The beam then passes through a second microwave cavity where the remaining atoms in the initial state are removed by rf quenching. The final state is then quenched by a dc electric field, emitting 10.2 eV Lyman-alpha photons. The photons are detected by photoionization detectors, whose current output is measured by a data acquisition system.

B. Source and Collimation

The source is a duoplasmatron[1] producing a beam of protons at 500 eV which are then charge exchanged in a cesium vapor region. The charge exchange process produces several species other than neutral

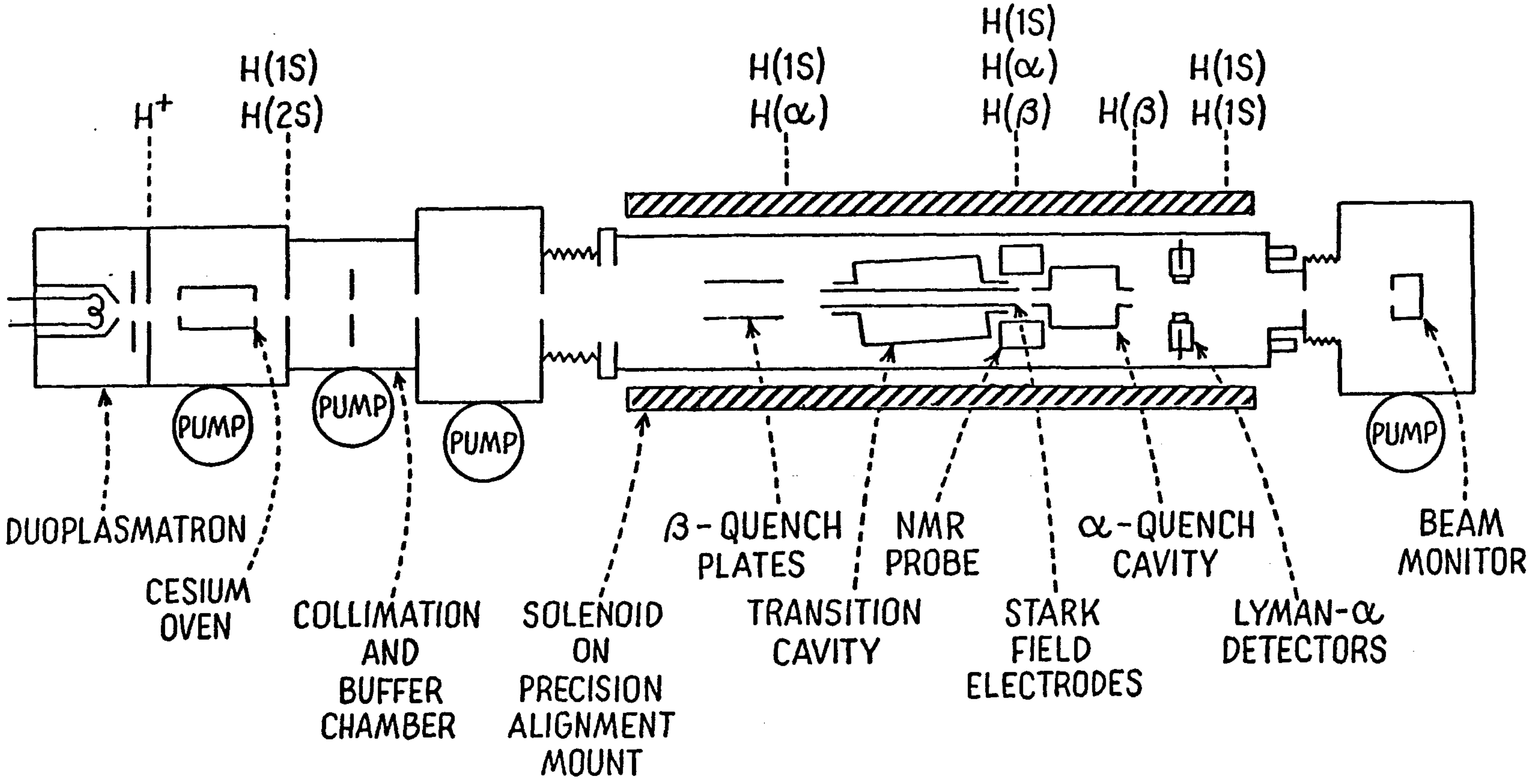

Figure 5.1 Apparatus Block Diagram

hydrogen. Charged species are removed from the beam by passing it through electrostatic deflection plates, after which the beam consists mainly of neutrals, some of which are atomic hydrogen. The cesium vapor pressure is set at $1.4\times10^{14}/\text{cm}^2$ for optimum formation of hydrogen in the $n=2$ level.

The beam is collimated, assuming the source is diffuse, with two circular knife edge collimators, yielding a diameter of 0.5 cm in the interaction region. For the purposes of collimation, the assumption of a diffuse source is the conservative assumption. The experience of Lévy[2] is that the source is "essentially" a point source.

Beam divergence is determined in two ways. For a point source, the collimators give a maximum divergence of 1500 μrads. It is measured by observing the strength of the α_{+1}-β_0 transition rate when the only dc electric field is the motional electric field due to beam divergence in a 520 gauss magnetic field. For a point source, the angle of divergence is proportional to the distance the atom is from the beam axis. Assuming the beam is cylindrically symmetric and uniformly distributed, this results in a beam divergence of ??? rads.

The stability of the beam is characterized in three ways: direction of the mean velocity, spatial distribution of atoms in the beam cross section, and the distribution in time of the atoms passing through the detection region. Techniques have not been developed to unambiguously measure the first two effects.

C. Beta Quench

The purpose of the beta quench region is to depopulate the final (β_0) state observed in the experiment. Upon entering the beta quench region the majority of the excited population of the beam is in the α_{+1}, α_0, β_0, and β_- levels of the n=2 shell. Since the experiment is performed at a magnetic field value near the crossing of the β and e states it is possible to selectively remove β states from the beam by applying a dc electric field. The dc electric field mixes the e states with the β states, causing their decay to the n=1 state. Since the α levels are separated by approximately 1500 MHz from the β states, only a small fraction of the α states are lost.

The beta-quench region consists of two closely-spaced semicylinders held at ±V ($V = 15V$ for α_{+1}-β_0, $V = 30V$ for α_0-β_0) with respect to machine ground. The exit end of the semicylinders is shaped to yield a quadrupole fall-off the electric field, thus reducing the size of electric fields from the beta quench region entering the interaction region.

D. Interaction Region

The interaction region contains an rf electric field, $\vec{\varepsilon}$, of about 4 V/cm at 1500 MHz tilted at an angle ϕ (5°) with respect to the Zeeman axis (fig. 2.2), and a dc electric field, $\vec{E}$, of about 2 V/cm perpendicular to the Zeeman axis. The rf electric field is generated by operating a right circular cylindrical microwave cavity in the TM_{010} mode. In this mode the rf electric field is parallel to the cylinder axis. The beam passes through the microwave cavity parallel to the axis of the solenoid field. The dc electric field is generated by applying voltages ±V to a pair of carbon-coated glass semi-cylinders, whose axis is parallel to the magnetic field.

D.1 Microwave Cavity

The ϕ reversal is performed by rotating the cavity axis 180° around the beam axis, fig. 5.2. To achieve a 1% ϕ reversal the cavity must be accurately and repeatably rotated about the beam axis. Figure 5.3 shows the apparatus used to do this. A stationary ring is located in a fixed position with respect to the beam axis, fig. 5.3a. Machined into the face of this ring are three equally spaced grooves in which are held 1/4" sapphire ball bearings, fig. 5.3b. The ball bearings mate with three equally spaced grooves in the 5° wedge, groove set (a) fig. 5.3c. The 5° wedge holds the cavity. The cavity body is a right circular cylinder with mating end plates. The end plates are cylindrically symmetric and mate with the end caps. Holes are machined through the end caps at 5° with respect to the cavity axis to allow for the passage of the beam. To perform the ϕ reversal the 5° wedge and cavity are lifted off the ball bearings, rotated 180° about the beam axis, and sat back on the ball bearings using groove set (b). Using a combination of screws and gears the ϕ reversal can be performed under vacuum by manipulating two rotary feedthroughs.

The cavity rotation assembly was designed to meet the future needs of the experiment. The stationary ring and 5° wedge are large enough to accept a cavity operating at a frequency low enough to permit the α_0-β_0 resonance to occur at 510-515 gauss. The stationary ring is

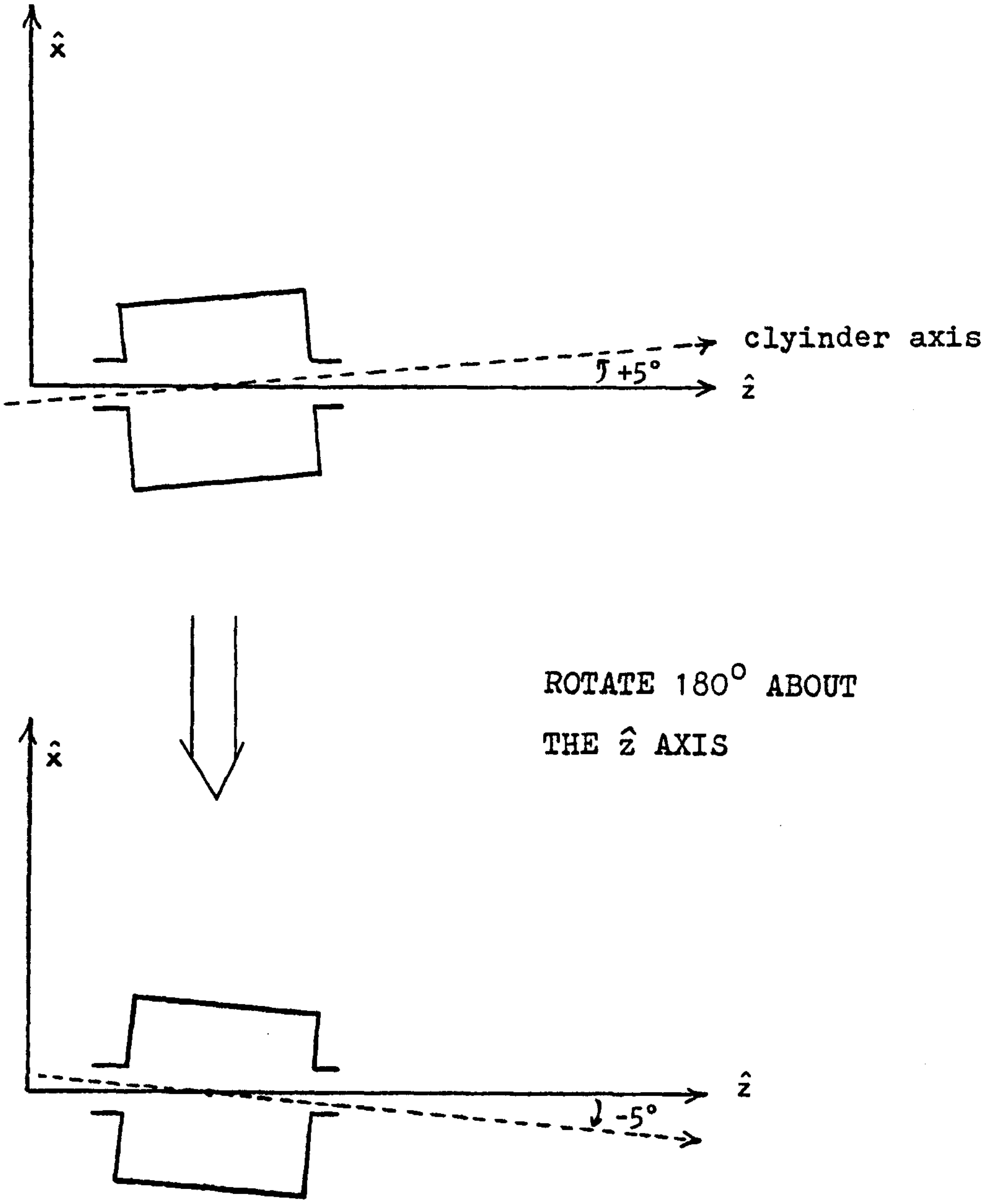

Figure 5.2 Schematic Illustration of Phi Flip

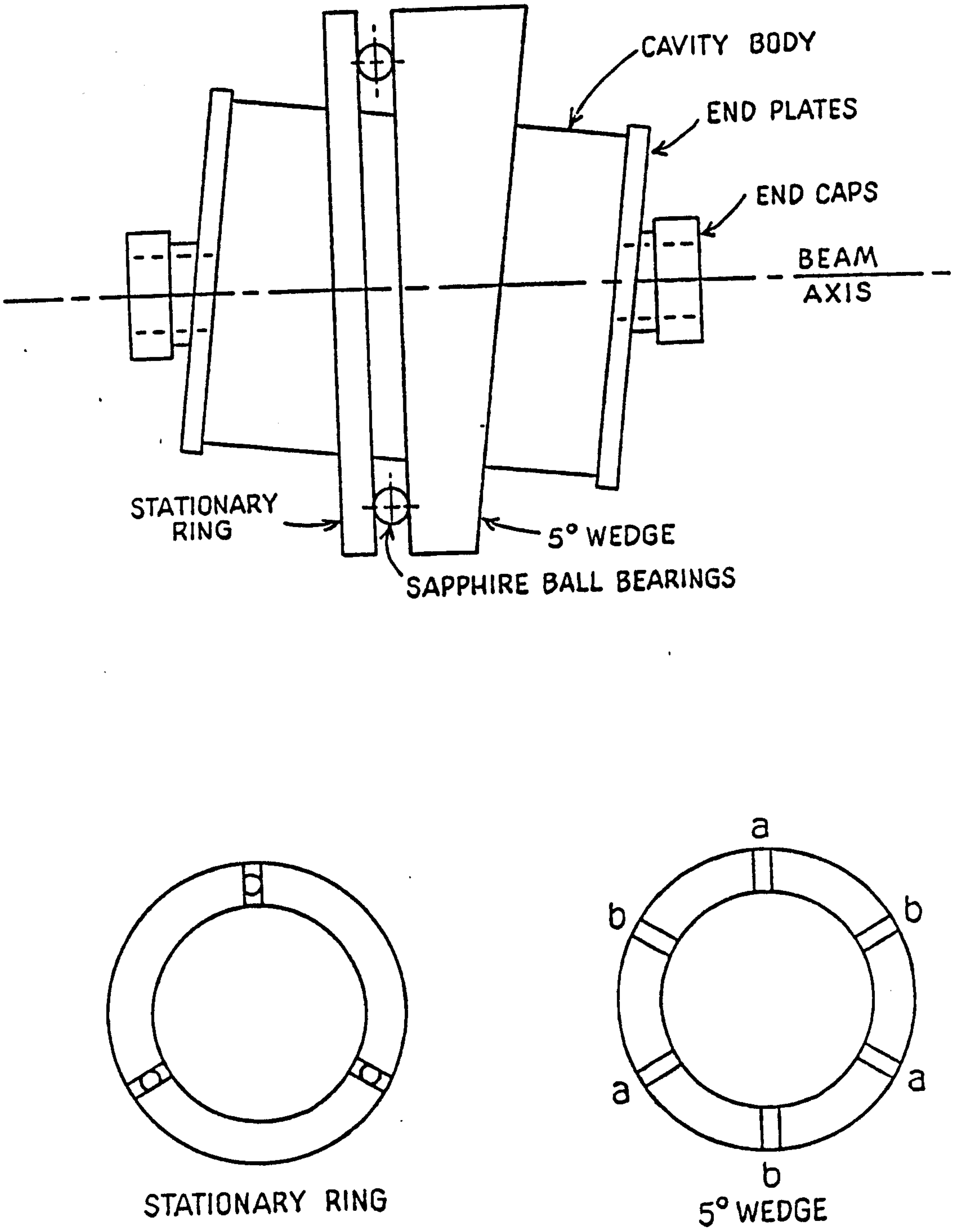

Figure 5.3 Interaction Cavity Alignment Methods

large enough to accept a cavity held by a 10° wedge. Since the cavity body and end plates are cylindrically symmetric, they can be used at any angle.

Requiring that the ϕ reversal be performed with a particular accuracy restricts the errors permitted in the components of the rf electric field, $\vec{\varepsilon}$, when the direction of $\vec{\varepsilon}_x$ is reversed. If a 1% reversal (Chapter IV) is to be achieved, initially, $\vec{\varepsilon} = \varepsilon_x\hat{\varepsilon}_x + \varepsilon_z\hat{\varepsilon}_z$, and after the reversal $\vec{\varepsilon}' = -\varepsilon'_x\hat{\varepsilon}_x + \varepsilon'_y\hat{\varepsilon}_y + \varepsilon'_z\hat{\varepsilon}_z$, where $(\varepsilon_x-\varepsilon'_x)/\varepsilon_x <$ 0.005, and $\varepsilon'_y/\varepsilon_z < 0.01$.

To satisfy the ε_y requirement, two conditions must be met. First, assuming the axis about which the cavity rotates remains fixed, it must be rotated 180°±6.5°. Secondly, assuming the cavity rotates 180°, but its axis tilts out of the initial x-z plane, this tilt must not be more than 0.57°. Both of these requirements are trivial to meet.

Translating the ε_x requirement directly into machining tolerances requires parts machined to better than 0.001 inch. However, the actual requirement is not the reversal of the cavity about some imaginary axis, but the reversal of ε_x about the beam axis. An axis about which ε_x changes only its sign, can always be found. This reasoning ignores the components of ε_x due to the divergence of $\vec{\varepsilon}$ in the endcaps. Restrictions placed on cavity tolerances due to this divergence are unknown.

D.2 Electric Field Electrodes

The electrodes used to apply the dc electric field are carbon coated glass semi-cylinders. The semi-cylinders are carbon coated both inside and outside. Typical end-to-end resistance of a semi-cylinder is about 50 MΩ.

The semi-cylinders are held at one end by a five axis positioning stage. The stage is adjustable while the system is under vacuum via five flange mounted rotary feedthroughs. The electrodes can be rotated about their cylindrical axis, translated along the x and y axes, and rotated about the cavity center in the xz and yz planes. The positioning stage was designed to permit a resolution of 100 micro-inches in translation and 50 microradians in rotation.

E. Magnetic Field

The apparatus involved in magnetic field generation comprises a solenoid, solenoid power supply, solenoid support system, and earth-field shim coils.

The solenoid and power supply were custom-built by Alpha Scientific of Hayward, CA. The solenoid has twelve layers of 440 turns of #10 square copper wire, with two moveable cylindrically-symmetric shims of four layers of 62 turns of the same wire. The shims and solenoid are electrically connected in series. By adjusting the position of the shims along the solenoid axis, the shape of the magnetic field has been adjusted so that the axial component changes by less than 200 ppm through the central 12 centimeters of the interaction region. Currently, almost no effort has been put into minimizing axial component variation. It is expected that significant improvements can be made.

The power supply is a voltage-controlled current source. It was designed to the following specifications, where ΔI = change in output current:

$\Delta I/5°C$ change in ambient temperature $< \pm 10$ ppm
$\Delta I/\pm 10\%$ change in line load $< \pm 10$ ppm
$\Delta I/1$ second $< \pm 10$ ppm
$\Delta I/8$ hours $< \pm 100$ ppm

The power supply's current output is controlled by a magnetic field control unit using a digital-to-analog converter, and soon an NMR-based control unit will be installed (see Appendix C).

To keep the motional electric fields small enough so as not to introduce undesirable systematic effects, it is necessary to align the magnetic field with the average beam velocity to one microradian. Since the solenoid weighs approximately 1500 lbs, this was somewhat of a challenge. The selected system involves hanging the entire solenoid from two 0.050 inch by 4.0 inch phosphor bronze strips which are attached to a float submerged in a tank of automobile antifreeze (mainly ethylene glycol), see fig. 5.4. The phosphor bronze strips permit the solenoid to be rotated in the yz plane. The neutral buoyancy of the float permits rotation in the xz plane and translations along the x, y, and z axes. Rotations in the yz and xz planes will be controlled by five micro-inch resolution micrometers, permitting resolution well beyond the required one microradian.

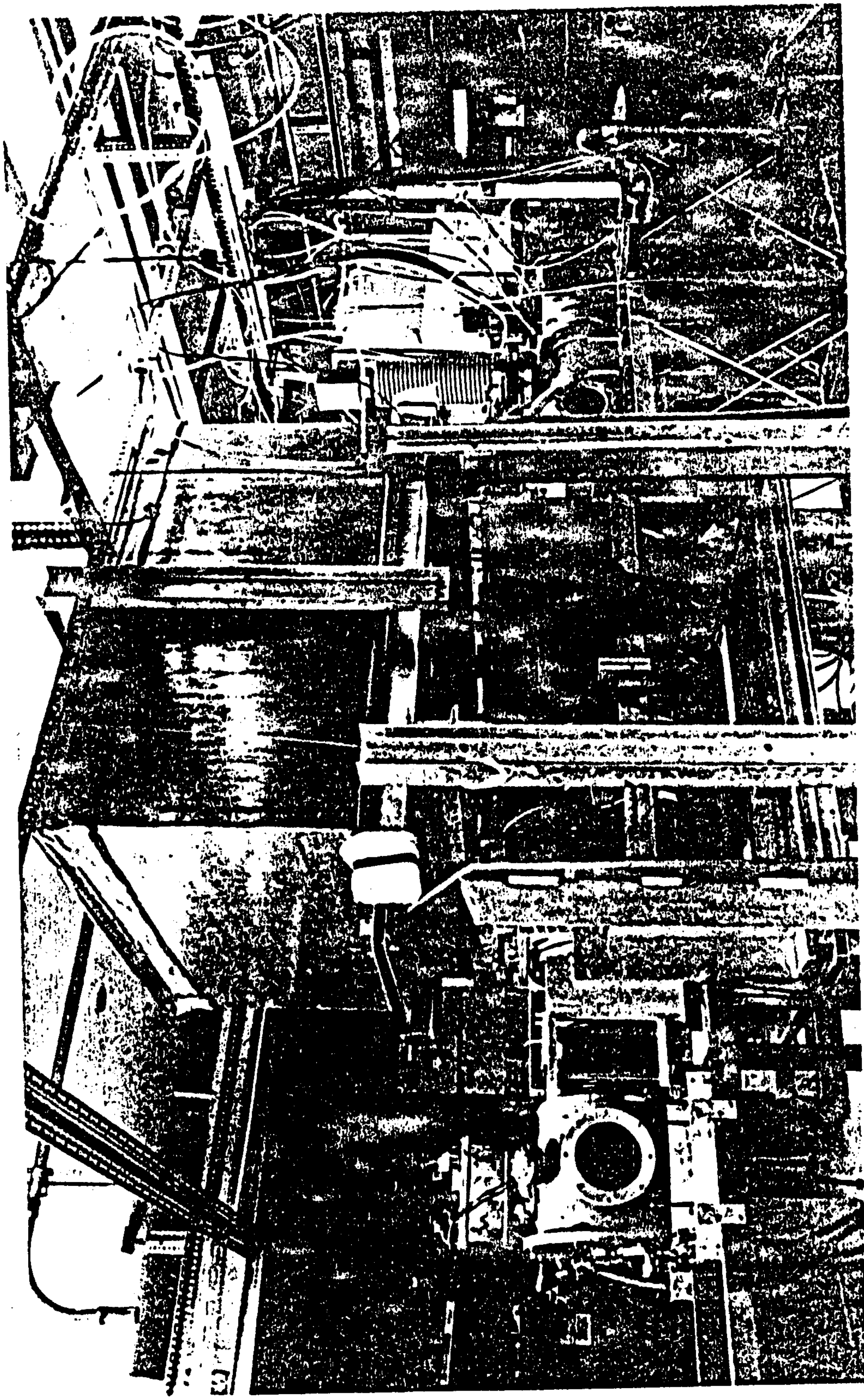

Figure 5.4 Solenoid Support System

The earth's magnetic field has components along the x, y, and z axes. To perform the magnetic field reversal without adjusting the solenoid's magnetic field direction, it is necessary to cancel out the x and y components of the earth's field. This is done with a set of earth field shim coils. They are two rectangular pairs of coils placed in the xz and yz planes on the outside of the main solenoid. The homogeneity of these coils throughout the twelve centimeters of the interaction region is the order of one milligauss. The z component of the earth's magnetic field is parallel to the main magnetic field and will be compensated for by the NMR magnetic field control unit.

F. Alpha Quench and Detection

The α quench cavity follows the main transition region by 3 cm and removes the initial α_0 state before the beam reaches the detectors.[3] The population of the α states is 10^5 times larger than the β_0 population when the beam exits the main transition region. The atoms in the β_0 states are detected by observing the Lyman-α radiation when they are quenched in a dc electric field near the β-e crossing. Although the dc Stark quenching rate of the α state atoms is much smaller (10^{-3}) than that for the β state atoms at this magnetic field, the radiation from such quenching would completely dominate the desired signal. This problem is eliminated by removing a large fraction of the α state atoms by resonant α-f quenching in a microwave cavity just prior to the detection region. The cavity axis is perpendicular to the magnetic field axis. The quenching efficiency is very good, but a small fraction of the background remains related to this region: its origin comes from multiple scattering of the Lyman-α radiation produced in the α quench cavity into the detectors. Three light baffles between the cavity and the detection region have reduced this problem to an acceptable level. The atoms in the β state are detected by applying a localized electric field to selectively quench them in the field of view of the Lyman-α detectors. Because of a Lyman-α radiation background arising from the decay of the high Rydberg states produced in the cesium charge exchange it has been discovered that if the electric field localization is very high, this background can be greatly reduced. The background is proportional to the beam volume in sight of the detectors whereas the signal is proportional to the quenching efficiency. A very high quenching efficiency has been achieved with a quadrupole field configuration, together with carbon films to improve the boundary conditions. This electric field configuration has the same features as that used by Van Wijngaarden et al.,[4] and is shown in figure 5.5. The electric field is transverse to the magnetic field direction and is confined to a distance of 6 mm along the beam direction by using shaped ceramic glass supports for the thin carbon films and the four quenching rods. The square of the electric field switches from 10 to 90% of its central value in 1.5 mm.

The Lyman-α photoionization detectors have been described elsewhere.[5] Their main features are large solid angle, good quantum efficiency (20 to 25%) and high gain (up to 10^4). The current from the two photoionization detectors is fed to a current sensitive preamplifier with a maximum sensitivity 10^9 V/A.

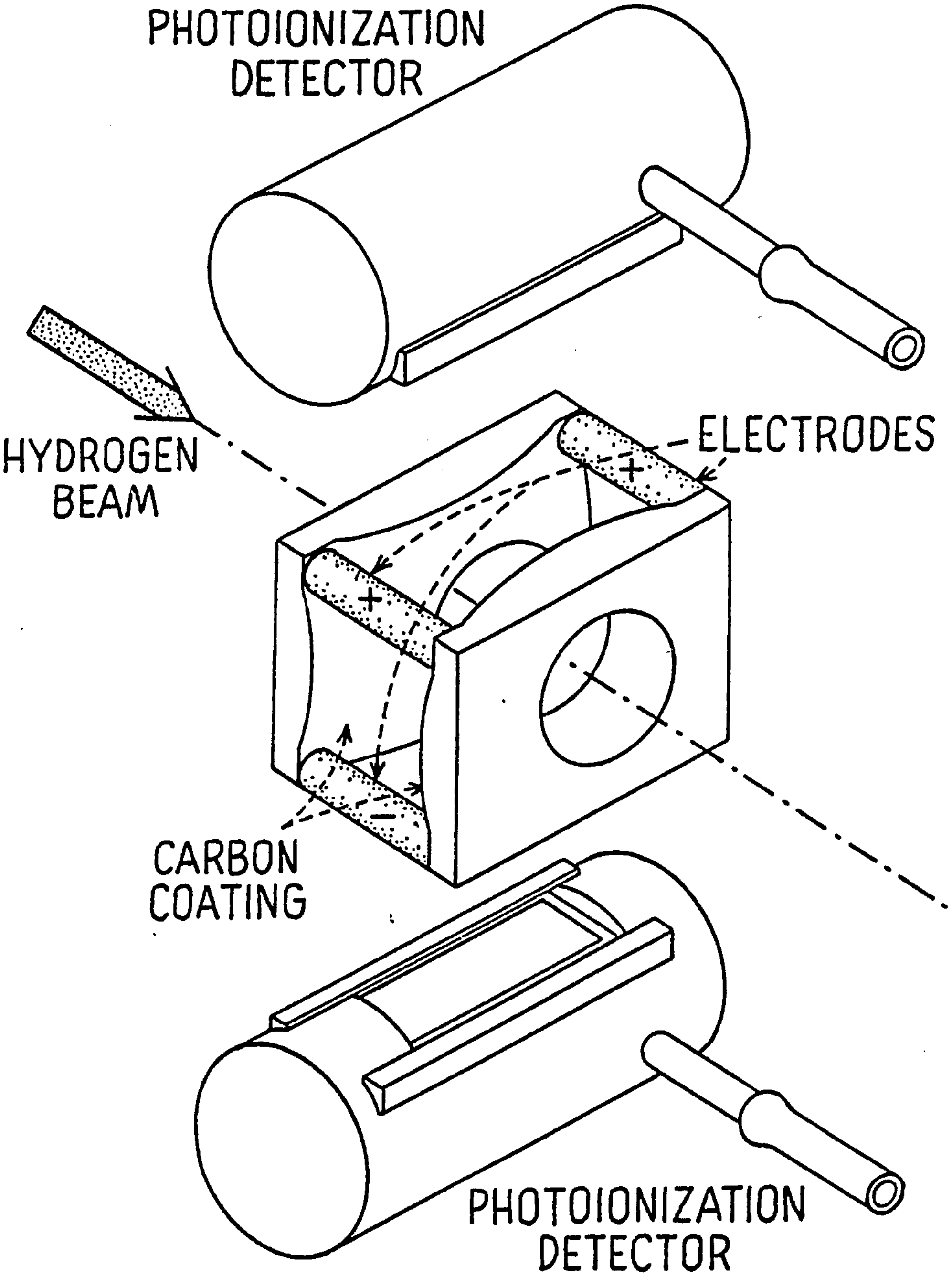

Figure 5.5 Detection Region

G. Neutral Beam Detector

The beam ends its transit of the machine by hitting a Faraday cup. The Faraday cup is useful for determining if the source is providing neutrals that are not arriving in the detection region as n=2 hydrogen.

H. Support System

The frame of the machine was designed so that the interaction region could be moved independently of the beam source and solenoid. The two collimators are attached to the source region of the machine (fig. 5.1) and the source region is separated from the interaction region by a bellows. The vacuum chambers of the source and interaction regions are each attached to their own frames, and the frames are anchored solidly to the floor. Therefore, if the vacuum chambers and frames were rigid objects, it would be possible to move the interaction region without moving the beam direction. Although this is not the case (nor was it expected to be) due to the bellows being very stiff, it represents a significant improvement over the previous generation.

I. Electronic Instrumentation

Figure 5.6 is a block diagram of the soon-to-be-installed data acquisition system. The computer is a Charles River Data Universe 68/05 which communicates with the following major items: a graphics terminal, plotter-printer, and a unit called the microcontroller. The

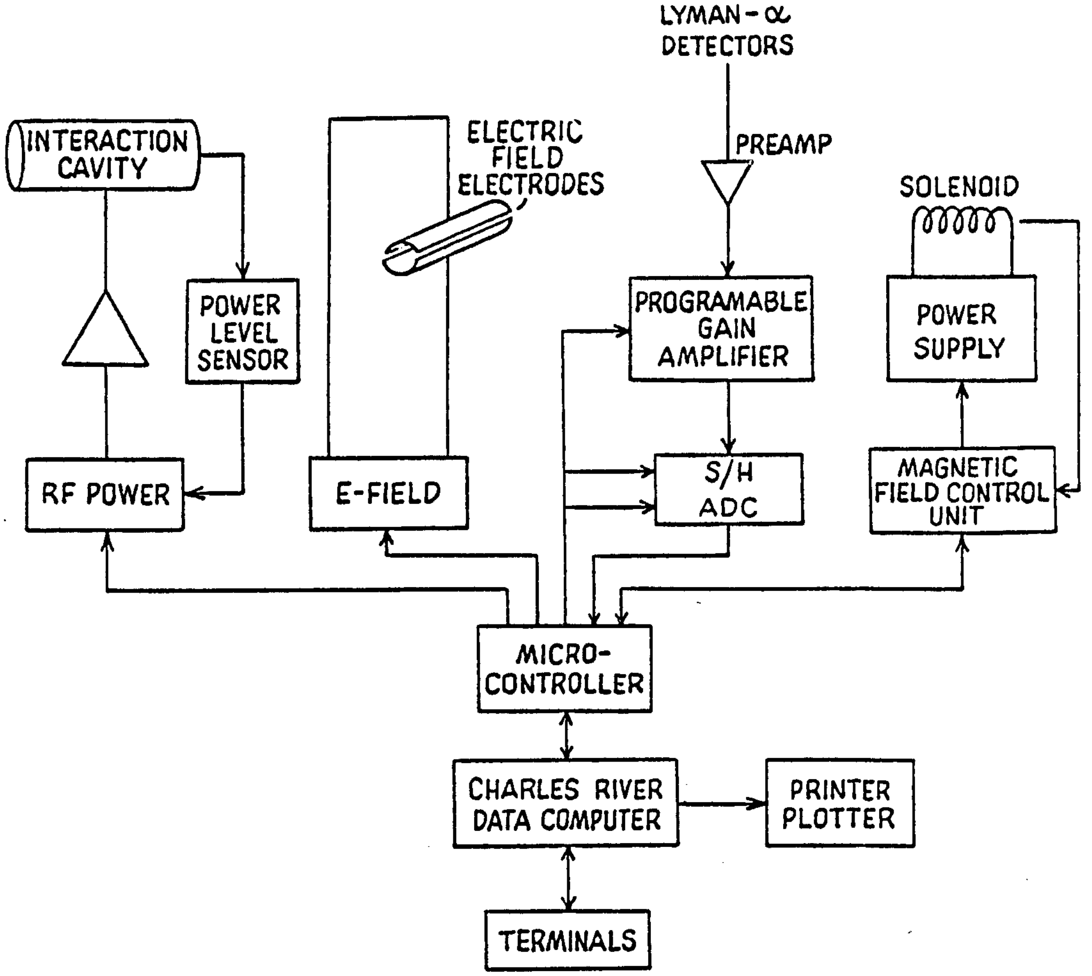

Figure 5.6 Data Acquisition System

microcontroller, rf power leveler, E-field direction/magnitude unit, programmable gain and ADC, and NMR unit are custom-built devices. It is possible for either the computer or the microcontroller to control the rf power level, E-field magnitude and direction, the gain and analog-to-digital conversion of the Lyman-α signal, and the value of the magnetic field through the NMR unit. Typically the computer controls the previously mentioned devices when the system is being tested. The microcontroller controls the devices when taking data and one is concerned about the relative timing of different events. The microcontroller can issue new commands to any one device every 500 nsec (see Appendix B).

J. Pumping

In fig. 5.1 pumps P1 and P2 are Varian (Model #VK-12A) cryopumps with pumping speeds of approximately 1000 liters/sec. After the system has been pumped on for two weeks, the base pressure with the source valved off is about 2×10^{-8} torr. With the source operating the pressure is slightly higher. P3 is an orb-ion pump differentially pumping the source.

References for Chapter V

1. T. Trainor, PhD dissertation, unpublished (available from University Microfilms, Ann Arbor, MI).

2. L.P. Lévy, PhD dissertation, University of Michigan (1982) unpublished (available from University Microfilms, Ann Arbor, MI).

3. This section duplicated with minor modification from L. Levy Thesis, pg. 73-76.

4. A. van Wijngaarden et al., J. Phys. B9, 2017 (1976).

5. L. Lévy, PhD Thesis (1982) University of Michigan, Chapter IX(ii).

CHAPTER VI

DATA, PROBLEMS, AND FUTURE PLANS

A. Introduction

At the time of this writing preliminary results indicative of trends have been observed. These results and associated problems are presented in this chapter.

B. Current Limits on the Understanding of Beam and Field Alignment Techniques

By using invariant analysis it is possible to set upper limits on allowed field and beam misalignments. The approach, where a set of misalignments are assumed and invariant analysis used to calculate the resulting asymmetry, is known as working backwards. In actuality, the experimenter must work forward; i.e., an asymmetry is observed and field and/or beam misalignments derived. For the current method of applying fields to the interaction region no one knows how to work forward, or even if it can be done in principle. However, not only has very little effort been put into figuring out to work forward, no one has shown it can not be done either. What is know is that not all misalignments distort the lineshapes in the same way.

C. α_+-β_0 Transition

The E and B flips have been performed for the α_+-β_0 transition (final state population = 25% of initial state). The ϕ flip has not been attempted, awaiting completion of minor mechanical items. The applied electric field E is reversed by reversing the potentials applied to the glass electrodes. The B flip is performed by reversing the direction of the current in the solenoid. Due to the presence of the earth's magnetic field this does not necessarily reverse B applied, however the component of B_{earth} parallel to $B_{applied}$ is only a few milligauss. Assuming this constitutes a B flip results in the following asymmetries over a selected range of operating conditions:

E flip: +3.1% -4.0%
B flip: +1.0% -5.1%
ϕ flip: unused

Figure 6.1 is an example of a $E_{applied}$ flip.

D. α_0-β_0 Transition

Due to the small size of the α_0-β_0 transition (4 ppm of the initial state) the signal-to-noise is very poor and therefore no flips have been attempted, the efforts being put into signal-to-noise improvement. Figure 6.2 is an example the α_0-β_0 transition. The top trace shows α_0-β_0 transition. The top trace shows α_0-β_0 (center), two allowed deuterium transitions (edges), and α_+-β_- (right edge, also). The bottom trace, only α_0-β_0, was taken later, showing an improvement in the signal-to-noise. Even later traces (not shown) have better signal-to-noise and show no evidence of Ramsy patterns, indicating minimal z electric fields due to electrode end effects.

E. Future Plans

Near term plans include completing the magnetic field control unit, data acquisition system, and ϕ flip. Interference of motional electric fields with the E and B flips and how to work forward must be studied. In the long term a "cold source" of atomic hydrogen will be installed with a beam velocity ~1/240 of the current beam velocity. This makes the experiment 240 times easier to do in terms of the physics. However, the magnetic field homogeneity requirements are probably 240 times greater.

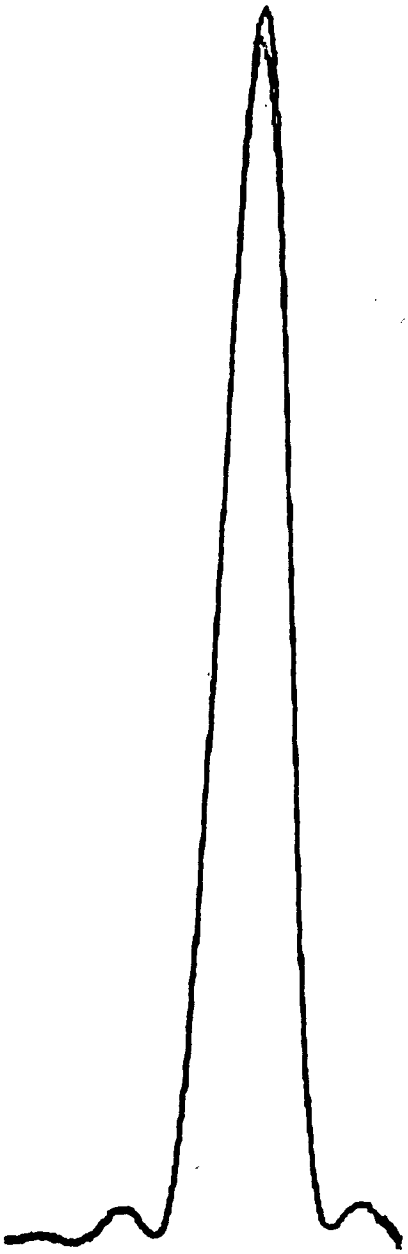

Figure 6.1. $\alpha_+ - \beta_0$ E_{applied} Flip

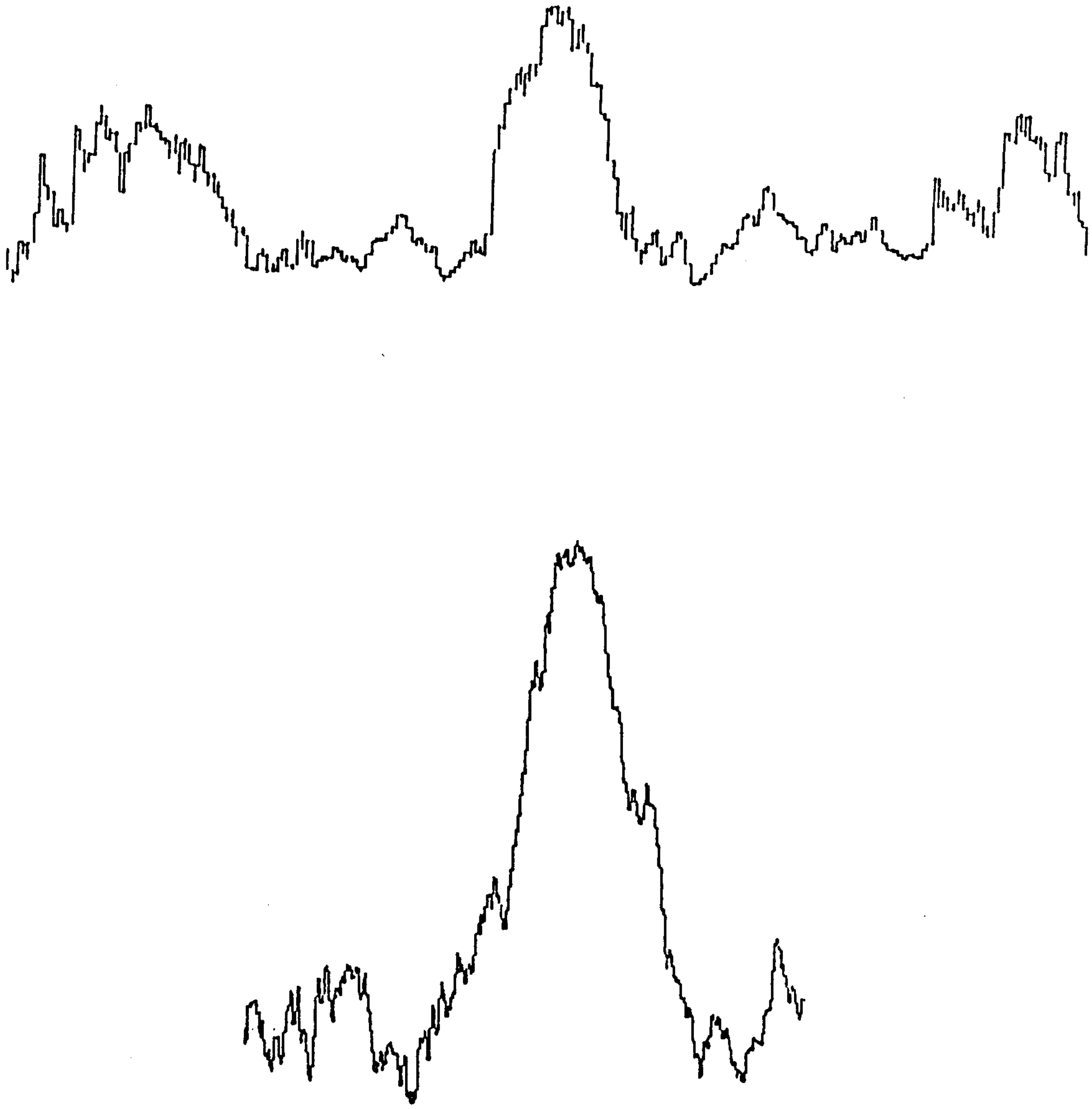

Figure 6.2. α_0-β_0 Transition

APPENDICES

Appendix A

Generalized Version of Gordon Drake/Laurent Lévy Driven Three Level Problem[1]

A. Driven 3 level - strong resonances

The goal here is to solve the driven 3-level problem for both the strong (α_{+1}-β_0, α_0-β_{-1}) and α_0-β_0 resonances.[2] Table 1 presents four transitions in hydrogen that are of interest in this work. Assuming the resonances involve only 3 levels is a good approximation. For α_+-β_- and α_0-β_- transitions only one channel exists into the final state (ignoring all states except α, β, and e). For α_+-β_0 there are two channels, but both legs of the second channel are hyperfine-suppressed, yielding a transition rate even smaller than α_0-β_0. The α_0-β_0 transition is a 4 level transition, but great lengths are taken not to apply a dc electric field in the z-direction between e_0 and β_0.

A.1 dc Stark transformations

For the strong resonances

$$\begin{bmatrix} \alpha' \\ e' \\ \beta' \end{bmatrix} = \begin{bmatrix} \cos\theta_1 & \sin\theta_1 & 0 \\ -\sin\theta_1 & \cos\phi & \sin\theta_2 \\ 0 & -\sin\theta_2 & \cos\theta_2 \end{bmatrix} \begin{bmatrix} \alpha \\ e \\ \beta \end{bmatrix} \qquad (A.1)$$

where

$$\sin^2\phi = \sin^2\theta_1 + \sin^2\theta_2 \ , \quad \sin\theta_1 = \frac{\langle e|H_S|\alpha\rangle}{E_e - E_\alpha - i\Gamma/2} \ , \quad \sin\theta_2 = \frac{\langle \beta|H_S|e\rangle}{E_\beta - E_e + i\Gamma/2} \ .$$

α, e, β are the Zeeman eigenstates between 500 to 600 gauss, and α', e', β' are the eigenstates after addition of the dc Stark fields.

Since $\sin\theta_1 \sim 0$, (A.1) becomes

$$\begin{bmatrix} \alpha' \\ e' \\ \beta' \end{bmatrix} = \begin{bmatrix} 1 & 0 & 0 \\ 0 & \cos\theta_2 & \sin\theta_2 \\ 0 & -\sin\theta_2 & \cos\theta_2 \end{bmatrix} \begin{bmatrix} \alpha \\ e \\ \beta \end{bmatrix} \tag{A.2}$$

A.2. Time dependence

The equation of motion in the Stark basis is[3]

$$i\cdot\dot{u}' = [H'_{rf} - i\,\frac{D'}{2}]u' \tag{A.3}$$

where u' is a column matrix and H'_{rf} and D' are square matrices. Here

$$H'_{rf} = e^{i\Lambda'_r t}\,P^{-1}\,H_{rf}\,Pe^{-i\Lambda'_r t} \quad , \tag{A.4}$$

and D'/2 is the imaginary part of $P^{-1}\,H_S\,P = \Lambda'$ and $H_S = H_Z + e\vec{E}_a\cdot\vec{r}$.

$$H_S = \begin{bmatrix} E_\alpha & \langle\alpha|H_S|e\rangle & 0 \\ \langle e|H_S|\alpha\rangle & E_e - i\Gamma/2 & \langle\beta|H_S|e\rangle \\ 0 & \langle e|H_S|\beta\rangle & E_\beta \end{bmatrix} \tag{A.5}$$

Assuming $\langle\alpha||e\rangle \sim 0$ since they have large energy denominators, equation (A.5) becomes

$$H_S \cong \begin{bmatrix} E_\alpha & 0 & 0 \\ 0 & E_e - i\Gamma/2 & E \\ 0 & E & E_\beta \end{bmatrix} . \tag{A.6}$$

where $E = \langle\beta|H_S|e\rangle$. The eigenvalues of equation (A.6) are

$$E_\alpha\ ,\ (E_e - i\Gamma/2) + \frac{|E|^2[(E_e-E_\beta) + i\Gamma/2]}{(E_\beta-E_e)^2 + \Gamma^2/4}\ ,$$
$$E_\beta - \frac{|E|^2[(E_e-E_\beta) + i\Gamma/2]}{(E_e-E_\beta)^2 + \Gamma^2/4} \tag{A.7}$$

Therefore

$$iD'/2 = \begin{bmatrix} 0 & 0 & 0 \\ 0 & -i\Gamma/2 + \dfrac{i\Gamma/2\ |E^2|}{(E_e-E_\beta)^2 + \Gamma^2/4} & 0 \\ 0 & 0 & -\dfrac{i\Gamma/2\ |E^2|}{(E_e-E_\beta)^2 + \Gamma^2/4} \end{bmatrix}$$

Let $\gamma = \dfrac{|E|^2\Gamma}{(E_\beta-E_e)^2 + \Gamma^2/4)}$ which is the dc Stark induced width of the β state. Also

$$\Lambda_r' = \begin{bmatrix} E_\alpha & 0 & 0 \\ 0 & E_e - \dfrac{|E^2|(E_\beta-E_e)}{(E_e-E_\beta)^2 + \Gamma^2/4} & 0 \\ 0 & 0 & E_\beta + \dfrac{|E|^2(E_e-E_\beta)}{(E_e-E_\beta)^2 + \Gamma^2/4} \end{bmatrix} \qquad (A.9)$$

Let $u = \dfrac{|E|^2(E_e-E_\beta)}{(E_e-E_\beta)^2 + \Gamma^2/4}$. Then equation A.9 becomes

$$\Lambda_r' = \begin{bmatrix} E_\alpha & 0 & 0 \\ 0 & E_e+u & 0 \\ 0 & 0 & E_\beta-u \end{bmatrix} = \begin{bmatrix} E_\alpha' & 0 & 0 \\ 0 & E_e' & 0 \\ 0 & 0 & E_\beta' \end{bmatrix} \qquad (A.10)$$

Equation (A.2) which gives P^{-1} (to within a phase factor) has an inverse P given by the transpose of P^{-1}. The inverse is good to at least $O(\theta^2)$.

$$H_{rf} = \begin{pmatrix} 0 & R & 0 \\ R & 0 & T \\ 0 & T & 0 \end{pmatrix} \cos(\omega t) \quad , \quad \text{where} \quad \begin{matrix} R = \langle\alpha|H_{rf}|e\rangle \\ T = \langle\beta|H_{rf}|e\rangle \end{matrix}$$

Let

$$H'_{rf} = e^{i\Lambda'_r t}\, P^{-1}\, H_{rf} P\, e^{-i\Lambda'_r t}$$

$$= \frac{1}{2}\begin{bmatrix} 0 & R\cos\theta\, e^{i(E'_\alpha - E'_e - \ \omega)t} & -R\sin\theta\, e^{i(E'_\alpha - E'_\beta - \ \omega)t} \\ R\cos\theta\, e^{i(E'_e - E'_\alpha + \ \omega)t} & 0 & 0 \\ -R\sin\theta\, e^{i(E'_\beta - E'_\alpha + \ \omega)t} & 0 & 0 \end{bmatrix} \tag{A.11}$$

where all terms off-resonance by about 1500 MHz have been ignored.

Letting

$$\delta'_r = E'_e - E'_\alpha + \cdot\omega \qquad \Delta'_r = E'_\beta - E'_\alpha + \cdot\omega$$

$$R' = R\cos\theta \qquad V' = -R\sin\theta \quad ,$$

equation (A.11) becomes

$$H'_{rf} = \frac{1}{2}\begin{bmatrix} 0 & R'\, e^{-i\delta'_r t} & V'\, e^{-i\Delta'_r t} \\ R'\, e^{i\delta'_r t} & 0 & 0 \\ V'\, e^{i\Delta'_r t} & 0 & 0 \end{bmatrix} \tag{A.12}$$

Using equations (A.3), (A.8), and (A.12), the equation of motion becomes

$$i\cdot \begin{bmatrix} \dot{\alpha}' \\ \dot{e}' \\ \dot{\beta}' \end{bmatrix} = \begin{bmatrix} 0 & \frac{1}{2} R'\, e^{-i\delta'_r t} & \frac{1}{2} V'\, e^{-i\Delta'_r t} \\ \frac{1}{2} R'\, e^{i\delta'_r t} & -i\,\frac{\Gamma}{2} + i\gamma/2 & 0 \\ \frac{1}{2} V'\, e^{i\Delta'_r t} & 0 & -i\gamma/2 \end{bmatrix} \begin{bmatrix} \alpha' \\ e' \\ \beta' \end{bmatrix} \tag{A.13}$$

Absorb the • into R' and V'. In the $\dot{\alpha}'$ equation the R' term is much larger than the V' term, and it should be given the assumptions. Equation (A.13) reduces to

$$
\begin{aligned}
i\dot{\alpha}' &= \frac{1}{2} R' e^{-i\delta_r' t} e' \\
i\dot{e}' &= \frac{1}{2} R' e^{i\delta_r' t} \alpha' - \frac{i}{2}(\Gamma+\gamma)e' \\
i\dot{\beta}' &= \frac{1}{2} V' e^{i\Delta_r' t} \alpha' - \frac{i\gamma}{2} \beta'
\end{aligned}
\qquad (A.14)
$$

Drake's solution to the driven two-level problem results in the following

$$\alpha' = Ae^{-i(\delta'+D)t/2} + Be^{-i(\delta'-D)t/2} \qquad (A.15)$$

$$e' = e^{-\Gamma' t/2}[Ce^{+i(\delta'+D)t/2} + Fe^{i(\delta'-D)t/2}] \qquad (A.16)$$

where

$$D = [\delta'^2 + R'^2]^{1/2}$$

$$A = -\frac{[(\delta'-D)\alpha'(0) + R'e'(0)]}{2D} \qquad B = \frac{(\delta'+D)\alpha'(0) + R'e'(0)}{2D}$$

$$C = \frac{(\delta'+D)e'(0) - R'\alpha'(0)}{2D} \qquad F = \frac{(-\delta'+D)e'(0) + R'\alpha'(0)}{2D}$$

$$\Gamma' = \Gamma-\gamma \ .$$

The initial conditions $\alpha'(0) = 1$, $e'(0) = 0$ will be used. Solving for β' by using the solution for α' results in,

$$\beta'(t) = e^{-\frac{\gamma}{2}t} \beta(0) - ie^{-\frac{\gamma}{2}t} \int_0^t \frac{V'}{2} e^{i(\Delta_r' - i\frac{\gamma}{2})t} \alpha' dt \qquad (A.17)$$

Expanding equation (A.16) results in

$$A = \frac{-(\delta'-D)}{2D} = \frac{-(\delta' - [\delta'^2+R'^2]^{1/2})}{2D} \qquad \text{note } R'^2 << \delta'^2 \text{ so}$$

$$A = 0 + 0\left(\frac{R'^2}{(\Gamma/2)^2}\right) \tag{A.18}$$

$$B = 1 - 0\left(\frac{R'^2}{(\Gamma/2)^2}\right)$$

Substituting equation (A.18) into (A.17) yields

$$\beta(t) = \pi\, e^{-\frac{\gamma}{2}t}\, \beta(0) - ie^{-\frac{\gamma}{2}t} \int_0^t \frac{\gamma'}{2}\, e^{i(\Delta_r' - i\frac{\gamma}{2} - \frac{\delta'}{2} + \frac{D}{2})t}\, dt \tag{A.19}$$

Expanding δ'-D in the argument of the exponential of equation (A.19) in powers of R'/δ',

$$\delta'-D = \delta' - [\delta'^2+R'^2]^{1/2}$$

$$\cong \delta' - \delta' - \frac{1}{2}\frac{R'^2}{\delta'} = -\frac{1}{2}\,\frac{R'^2(\delta_r' + i\Gamma/2)}{\delta_r'^2 + \Gamma^2/4} \tag{A.20}$$

Noting that $\gamma/\Gamma << 1$ and $\theta << 1$,

$$s' = \frac{1}{4}\,\frac{R'^2\delta_r'}{\delta_r'^2 + \Gamma'^2/4} = \frac{1}{4}\,\frac{R^2\cos^2\theta(\delta_r+u)}{(\delta_r+u)^2 + (\Gamma-\gamma)^2/4}$$

$$\cong \frac{1}{4}\,\frac{R^2\delta_r}{\Gamma^2/4} + \frac{1}{4}\,\frac{R^2}{\Gamma^2/4}\,u \cong s + \frac{1}{4}\,\frac{R^2}{\Gamma^2/4}\,u \cong s \tag{A.21}$$

$$\varepsilon' = \frac{1}{4}\,\frac{R'^2\Gamma'}{\delta_r'^2 + \Gamma'^2/4} = \frac{1}{4}\,\frac{R^2\cos^2\theta(\Gamma-\gamma)}{(\delta_r+u)^2 + \frac{(\Gamma-\gamma)^2}{4}} \cong \frac{1}{4}\,\frac{R^2\Gamma}{\delta_r^2 + \Gamma^2/4} = \varepsilon \tag{A.22}$$

Let $\omega' = \Delta_r + s - u$ and $\beta'(0) = 0$, then (A.19) reads

$$\beta'(t) = \frac{e^{-\frac{\gamma}{2}t}}{i} \int_0^t \frac{\gamma'}{2} e^{i\omega' t} e^{(\gamma-\varepsilon)t/2} dt \tag{A.23}$$

The transformation back to the Zeeman basis for the strong resonance is

$$\beta = \beta'\cos(\theta_2) + e'\sin(\theta_2) \tag{A.24}$$

The e' term can be dropped, as shown below. From equation (A.16) we have

$$e' = e^{-\Gamma' t/2}\left(\frac{-R'}{2D} e^{i(\delta'+D)t/2} + \frac{R'}{2D} e^{i(\delta'-D)t/2}\right) \tag{A.25}$$

The second term damps out like $e^{-\Gamma' t/2}$ leaving

$$e' \cong \frac{-R'}{2D} e^{i(\delta'+D+i\Gamma')t/2} \tag{A.26}$$

Expanding and reordering the argument of the exponential equation (A.26) becomes

$$e' \cong \frac{-R'}{2D} e^{i(\delta_r+u+s)t} e^{-\varepsilon t/2} \tag{A.27}$$

Equation (A.27) is in resonance when $\delta_r+u+s = 0$ and β' is in resonance when $\omega' = \Delta_r+s-u = 0$. δ_r and Δ_r are the two largest terms and are out of resonance by about the separation from the β_0-e_0 crossing, about 10 MHz for the maximum sensitivity operating point. Therefore, The e' contribution will be dropped.

B. Driven 3-Level α_0-β_0

The important difference between the α_0-β_0 resonance and the strong resonances and previous work with motional DC electric fields is that there are two parity conserving channels into the β_0 state.

$$\begin{bmatrix} \alpha' \\ e_+' \\ \beta' \\ e_0' \end{bmatrix} = \begin{bmatrix} \cos\phi_1 & \sin\theta_1 & 0 & \sin\theta_4 \\ -\sin\theta_1 & \cos\phi_2 & \sin\theta_2 & 0 \\ 0 & -\sin\theta_2 & \cos\phi_3 & \sin\theta_3 \\ -\sin\theta_4 & 0 & -\sin\theta_3 & \cos\phi_4 \end{bmatrix} \begin{bmatrix} \alpha \\ e_+ \\ \beta \\ e_0 \end{bmatrix} \qquad (A.28)$$

where

$$\begin{array}{ccc} \sin^2\phi_1 & = \sin^2\theta_1 + & \sin^2\theta_4 \\ \vdots & & \vdots \\ \phi_4 & & \end{array} \qquad (A.29)$$

The approximate size of the above matrix elements is,

$$\sin\theta_1 \sim \frac{\langle\alpha_0|xy|e_+\rangle}{E_{\alpha_0}-E_{e_+}+i\Gamma/2} \sim \frac{(xy)\sin\theta}{1500} \sim \frac{(xy)1/20}{1500} \sim \frac{xy}{30{,}000} \qquad (A.30)$$

$$\sin\theta_2 \sim \frac{\langle\beta_0|xy|e_+\rangle}{E_{\beta_0}-E_{e_+}+i\Gamma/2} \sim \frac{(xy)\cos\theta}{i50} \sim \frac{xy}{50} \sim \frac{xy}{50} \qquad (A.31)$$

$$\sin\theta_3 \sim \frac{\langle\beta_0|z|e_0\rangle}{E_{\beta_0}-E_{e_+}+i\Gamma/2} \sim \frac{z\sin2\theta}{i50} \sim \frac{z\ 1/10}{50} \sim \frac{z}{500} \qquad (A.32)$$

$$\sin\theta_4 \sim \frac{\langle\alpha_0|z|e_+\rangle}{E_{\alpha_0}-E_{e_0}+i\Gamma/2} \sim \frac{z\cos2\theta}{1500} \sim \frac{z}{1500} \sim \frac{z}{1500} \qquad (A.33)$$

If $z = 0.1xy$, which is larger than possible with glass tubes, then by a factor greater than 100, $\sin\theta_2$ is the only relevant matrix element for the Stark to Zeeman transformation. However, since the effect of z electric fields is also desired, θ_3 shall be retained. P^{-1} for α_0-β_0 becomes

$$P^{-1} = \begin{bmatrix} 1 & 0 & 0 & 0 \\ 0 & \cos\theta_2 & \sin\theta_2 & 0 \\ 0 & -\sin\theta_2 & \cos\theta_3 & \sin\theta_3 \\ 0 & 0 & -\sin\theta_3 & \cos\theta_3 \end{bmatrix} \qquad (A.34)$$

Since the $\langle\beta_0|z|e_0\rangle$ matrix element for actual z will be small, its effect on the energy levels will be ignored, hence

$$\Lambda'_{\alpha_0-\beta_0} = \Lambda'_{\text{strong res.}}$$

Ignoring off-resonance terms, H_{rf} in the Zeeman basis is

$$H_{rf} = \begin{bmatrix} 0 & M & 0 & R \\ M & 0 & 0 & 0 \\ 0 & 0 & 0 & 0 \\ R & 0 & 0 & 0 \end{bmatrix} \cos(\omega t) \qquad (A.35)$$

where

$$R = \langle e_0|z|\alpha_0\rangle$$

$$M = \langle e_+|xy|\alpha_0\rangle \; .$$

Let

$$R' = R\cos\theta_3 \simeq R \qquad V' = M\sin\theta_2$$

$$T' = -M\sin\theta_2 + R\sin\theta_3 = V' + R\sin\theta_3 \qquad (A.36)$$

$$\delta_r = E_{e_0} - E_{\alpha_0} + \cdot\omega \qquad \Delta_r = E_{\beta_0} - E_{\alpha} + \cdot\omega$$

$$\chi_r = E_{e_+} - E_{\alpha_0} + \cdot\omega$$

$$H_{rf} = e^{i\Lambda'_r t} P^{-1} H_{rf} P e^{-i\Lambda'_r t} \qquad (A.37)$$

$$= \frac{1}{2} \begin{bmatrix} 0 & M\cos\theta_2 \, e^{i\chi'_r t} & T' \, e^{-i\Delta'_r t} & R' \, e^{-i\delta'_r t} \\ M\cos\theta_2 \, e^{i\chi'_r t} & -i\Gamma'/2 & 0 & 0 \\ T' \, e^{i\Delta'_r t} & 0 & 0 & 0 \\ R' \, e^{i\delta'_r t} & 0 & 0 & 0 \end{bmatrix}$$

Therefore the equation of motion becomes,

$$i\begin{bmatrix}\dot{\alpha}'_0\\ \dot{e}'_+\\ \dot{\beta}'_0\\ \dot{e}'_0\end{bmatrix} = \tag{A.38}$$

$$\frac{1}{2}\begin{bmatrix}0 & M\cos\theta_2\, e^{i\chi'_r t} & T'\, e^{-i\Delta'_r t} & R'\, e^{-i\delta'_r t}\\ M\cos\theta_2\, e^{i\chi'_r t} & -i\Gamma'/2 & 0 & 0\\ T'\, e^{i\Delta'_r t} & 0 & -\gamma/2 & 0\\ R'\, e^{i\delta'_r t} & 0 & 0 & -i\Gamma'/2\end{bmatrix}\begin{bmatrix}\alpha'_0\\ e'_+\\ \beta'_0\\ e'_0\end{bmatrix}$$

We shall eliminate e'_+ from the equation of motion. The reasons for this are:

1) It is coupled to α'_0, 1/20 as strongly as e_0
2) It always has a small population because of its large radiative width.

Applying this reduction, equation (A.38) becomes

$$i\begin{bmatrix}\dot{\alpha}'_0\\ \dot{\beta}'_0\\ \dot{e}'_0\end{bmatrix} = \begin{bmatrix}0 & \frac{T'}{2}\, e^{i\Delta'_r t} & \frac{R'}{2}\, e^{-i\delta'_r t}\\ \frac{T'}{2}\, e^{i\Delta'_r t} & -\gamma/2 & 0\\ \frac{R'}{2}\, e^{i\delta'_r t} & 0 & -i\Gamma'/2\end{bmatrix}\begin{bmatrix}\alpha'_0\\ \beta'_0\\ e'_0\end{bmatrix} \tag{A.39}$$

This is identical to the strong resonance equation (A.13) if T' is substituted for V'. When $E_z=0$, T'=V', otherwise T' is a function of both the xy and z electric fields.

C. General Solution

This section contains one solution to the 3 and 4 level resonances and shows how they can be specialized to each case. Only the two strong resonances and α_0-β_0 are used. The general form for the equation of motion is

$$i \begin{bmatrix} \dot{\alpha}' \\ \dot{e}' \\ \dot{\beta}' \end{bmatrix} = \begin{bmatrix} 0 & A\, e^{-i\delta_r' t} & B\, e^{-i\Delta_r' t} \\ A\, e^{i\delta_r' t} & -\frac{i}{2}(\Gamma-\gamma) & 0 \\ B\, e^{i\Delta_r' t} & 0 & -i\gamma/2 \end{bmatrix} \begin{bmatrix} \alpha' \\ e' \\ \beta' \end{bmatrix} \tag{A.40}$$

The solution to the differential equation for the population of the β state is

$$\beta(t) = -\cos(\theta_2)\, \frac{e^{-\gamma t/2}}{i} \int_0^t B\, e^{i\omega' t}\, e^{(\gamma-\varepsilon)t/2}\, dt \,. \tag{A.41}$$

In all three cases $\sin\theta_2$ is proportional to the x+y dc Stark matrix element between the p-state and β state. Changing the limits of the above integral to $\pm\tau/2$,

$$\beta(\tau/2) = \frac{-\cos(\theta_2)\, e^{i\omega'\tau/2}\, e^{-\frac{1}{2}(\gamma+\varepsilon)\tau/2}}{i} \int_{-\tau/2}^{\tau/2} B\, e^{i\omega' t}\, e^{(\gamma-\varepsilon)t/2}\, dt \,. \tag{A.42}$$

The above is completely general, and by substitution of the appropriate variables from Table 2 yields β_{final} for any of the 3 transitions.

Since these differential equations were solved using many approximations a question remains as to how good the solutions are.

Recall that the α-e amplitudes were solved for first, then the β amplitude. If the solution is to remain valid the amplitude in the β state must remain small with respect to the α amplitude. In the case of the strong resonances this means not depopulating the initial α state too much.

The differential equations were solved assuming B, γ, ε, and ω' were constants as a function of time for a given atom. This depends on the path an atom follows through the interaction region. This will be the case for beam tilts and divergence, but not for offsets. Therefore, using the above solution to describe offset cases is expected to give better results than tilted and diverging cases.

This might also be the reason why Lévy lineshape theory works better in the γ-ε=0 case. Not only is there averaging along the beam, but perhaps averaging over approximations made is solving the differential equations. Since the average across the beam is done in finite distances, $\beta(\tau)$ is converted to $\beta(z)$. Note that τ is not measured in seconds. τ always occurs with matrix elements measured in MHz,

$$\langle MHz\rangle\tau \quad \text{with} \quad \tau \quad \text{in} \quad 2\pi \ \mu\text{sec}$$

or

$$\langle MHz\rangle 2\pi \ 10^{-6}\tau' \quad \text{with} \quad \tau' \quad \text{in sec}$$

let

$$\tau' = z_0/V'$$

z_0 = interaction region length (cm)
V' = beam velocity (cm/sec)

or

$$\langle MHz\rangle\tau \rightarrow \langle MHz\rangle 2\pi \ 10^{-6} \ z_0/V = \langle MHz\rangle \ z_0/V$$

$$V = 2\pi/10^6 V'$$

With the following change of variable,

$$\tau = \frac{z_0}{V}\ , \quad t = \frac{z}{V}\ , \quad dt = \frac{1}{V}\, dz \tag{A.43}$$

equation (A.42) becomes,

$$\beta\left(\frac{z_0}{2V}\right) = \frac{-\cos(\theta_2)\ e^{i\omega' z_0/2V}\ e^{-\frac{1}{2}(\gamma+\varepsilon)z_0/2V}}{iV} \int_{-z_0/2V}^{+z_0/2V} e^{i\omega' z/V}\ e^{(\gamma-\varepsilon)z/2V}\ dz \tag{A.44}$$

Table A.1: Possible Transitions

(1) $\quad$ e_+ $\quad$ ($\cos\theta$)
z $\quad\quad$ xy

$\alpha_+-\beta_0$: $\quad$ α_+ $\quad\quad$ β_0 $\quad$ $R = \langle\alpha_+\vert z\vert e_+\rangle$

$E = \langle e_+\vert x+iy\vert \beta_0\rangle$

xy $\quad$ e_0 $\quad$ z
($\sin\theta$) $\quad\quad$ ($\sin2\theta$)

(1) $\quad$ e_+
z $\quad\quad$ (0)

$\alpha_+-\beta_-$: $\quad$ α_+ $\quad\quad$ β_- $\quad$ $R = \langle\alpha_+\vert x+iy\vert e_0\rangle$

$E = \langle e_0\vert x+iy\vert \beta_-\rangle$

xy $\quad$ e_0 $\quad$ xy
($\sin\theta$) $\quad\quad$ ($\cos\theta$)

($\sin\theta$) $\quad$ e_+
xy $\quad\quad$ (0)

$\alpha_0-\beta_-$: $\quad$ α_0 $\quad\quad$ β_- $\quad$ $R = \langle\alpha_0\vert x+iy\vert e_0\rangle$

$E = \langle e_0\vert x+iy\vert \beta_-\rangle$

z $\quad$ e_0 $\quad$ xy
($\cos2\theta$) $\quad\quad$ ($\cos\theta$)

($\sin\theta$) $\quad$ e_+ $\quad$ ($\cos\theta$)
xy $\quad\quad$ xy

$\alpha_0-\beta_0$: $\quad$ α_0 $\quad\quad$ β_0

$R = \langle e_0\vert z\vert \alpha_0\rangle$

$M = \langle e_+\vert x+iy\vert \alpha_0\rangle$

$E = \langle e_+\vert x+iy\vert \beta_0\rangle$

$E_z = \langle e_0\vert z\vert \beta_0\rangle$

z $\quad$ e_0 $\quad$ z
($\cos2\theta$) $\quad\quad$ ($-\sin2\theta$)

<u>Notes:</u> (1) Items in parantheses are the hyperfine suppression.
(2) The xyz is the direction of the field (rf or DC) driving the transition with $\vec{B} = B_0\hat{z}$.

Table A.2

Summary of Terms Used in the Lineshape Theory

$\alpha_+ - \beta_0$	$\alpha_0 - \beta_-$	$\alpha_0 - \beta_0$
$\alpha = \alpha_+$ $e = e_+$ $\beta = \beta_0$	$\alpha = \alpha_0$ $e = e_0$ $\beta = \beta_-$	$\alpha = \alpha_0$ $e = e_+$ $\beta = \beta_0$
$A = \frac{1}{2} R'$	*	*
$B = \frac{1}{2} V'$	*	$\frac{1}{2} T'$
$R' = R\cos\theta_2 \cong R$ $V' = -R\sin\theta_2$	* *	* $T' = -M\sin\theta_2 + R\sin\theta_3$
$\sin\theta_2 = \dfrac{\langle\beta_0\vert H_S^{x+y}\vert e_+\rangle}{E_{\beta_0} - E_{e_+} + i\Gamma/2}$	$\sin\theta_2 = \dfrac{\langle\beta_-\vert H_S^{x+y}\vert e_0\rangle}{E_{\beta_-} - E_{e_0} + i\Gamma/2}$	$\sin\theta_2 = \dfrac{\langle\beta_0\vert H_S^{x+y}\vert e_+\rangle}{E_{\beta_0} - E_{e_+} + i\Gamma/2}$
		$\sin\theta_3 = \dfrac{\langle\beta_0\vert H_S^{z}\vert e_0\rangle}{E_{\beta_0} - E_{e_0} + i\Gamma/2}$
		$= \dfrac{-\sqrt{3}\, e a_0 \sin 2\Theta E_z}{E_{\beta_0} - E_{e_0} + i\Gamma/2}$
$\delta' = \delta_r' - i\Gamma'/2$	*	*
$\Delta' = \Delta_r' - i\Gamma'/2$	*	*
$\delta_r' = \delta_r + u$ $= E'_{e_+} - E'_{\alpha_+} + \cdot\omega$ $\delta_r = E_{e_+} - E_{\alpha_+} + \cdot\omega$	* $= E'_{e_0} - E'_{\alpha_0} + \cdot\omega$ $\delta_r = E_{e_0} - E_{\alpha_0} + \cdot\omega$	* $= E_{e_+} - E_{\alpha_0} + \cdot\omega$ $\delta_r = E_{e_+} - E_{\alpha_0} + \cdot\omega$
$\Delta_r' = \Delta_r - u$ $= E'_{\beta_0} - E'_{\alpha_+} + \cdot\omega$ $\Delta_r = E_{\beta_0} - E_{\alpha_+} + \cdot\omega$	* $= E'_{\beta_-} - E'_{\alpha_0} + \cdot\omega$ $\Delta_r = E_{\beta_-} - E_{\alpha_0} + \cdot\omega$	* $= E'_{\beta_0} - E'_{\alpha_0} + \cdot\omega$ $\Delta_r = E_{\beta_0} - E_{\alpha_0} + \cdot\omega$
$E'_{\alpha_+} = E_{\alpha_+}$ $E'_{e_+} = E_{e_+} + u$ $E'_{\beta_0} = E_{\beta_0} - u$	$E'_{\alpha_0} = E_{\alpha_0}$ $E'_{e_0} = E_{e_0} + u$ $E'_{\beta_-} = E_{\beta_-} - u$	$E'_{\alpha_0} = E_{\alpha_0}$ $E'_{e_+} = E_{e_+} + u$ $E'_{\beta_0} = E_{\beta_0} - u$

*The same as the column to the left of this one.

Table A.2 (continued)

$\alpha_+ - \beta_0$	$\alpha_0 - \beta_-$	$\alpha_0 - \beta_0$
$R = \langle\alpha_+\|H^z_{rf}\|e_+\rangle$	$R = \langle\alpha_0\|H^z_{rf}\|e_0\rangle$	$R = \langle e_0\|H^z_{rf}\|\alpha_0\rangle$
$= \epsilon_z\langle\alpha_+\|z\|e_+\rangle$	$= \sqrt{3}\ ea_0\cos 2\Theta\epsilon_z$	$= \epsilon_z\langle e_0\|z\|\alpha_0\rangle$
$= \epsilon_z \sqrt{3}\ ea_0$		$= \sqrt{3}\ ea_0\cos 2\Theta\epsilon_z$
$E = \langle e_+\|H^{x+y}_S\|\beta_0\rangle$	$E = \langle e_0\|H^{x+y}_S\|\beta_-\rangle$	$E = \langle e_+\|H^{x+y}_S\|\beta_0\rangle$
$= \langle e_+\|H^x_S\|\beta_0\rangle+\langle e_+\|H^y_S\|\beta_0\rangle$	$= \langle e_0\|H^x_S\|\beta_-\rangle+\langle e_0\|H^y_S\|\beta_-\rangle$	$= \langle e_+\|H^x_S\|\beta_0\rangle+\langle e_+\|H^y_S\|\beta_0\rangle$
$= \sqrt{3}\ ea_0\cos\Theta(E_x+iE_y)$	$= \sqrt{3}\ ea_0\cos\Theta(E_x+iE_y)$	$= \sqrt{3}ea_0\cos\Theta E_x+i\sqrt{3}ea_0\cos\Theta E_y$
		$M = \langle e_+\|H^x_{rf}\|\alpha_0\rangle+\langle e_+\|H^y_{rf}\|\alpha_0\rangle$
		$= \epsilon_x\langle e_+\|x\|\alpha_0\rangle+\epsilon_y\langle e_+\|y\|\alpha_0\rangle$
		$= \sqrt{3}ea_0\cos\Theta\epsilon_x+i\sqrt{3}ea_0\sin\Theta\epsilon_y$
$\Gamma' = \Gamma-\gamma$	*	*
$\gamma = \frac{\|E^2\|\Gamma}{(E_{e_+}-E_{\beta_0})^2+\Gamma^2/4}$	$\gamma = \frac{\|E^2\|\Gamma}{(E_{e_0}-E_{\beta_-})^2+\Gamma^2/4}$	$\gamma = \frac{\|E^2\|\Gamma}{(E_{e_+}-E_{\beta_0})^2+\Gamma^2/4}$
$\epsilon = \frac{1}{4}\frac{R^2\Gamma}{\delta_r^2+\Gamma^2/4}$	*	*
$\delta' = \Delta_r + s - u$	*	*
$u = \frac{(E_{e_+}-E_{\beta_0})\|E^2\|}{(E_{e_+}-E_{\beta_0})^2+\Gamma^2/4}$	$u = \frac{(E_{e_0}-E_{\beta_-})\|E^2\|}{(E_{e_0}-E_{\beta_-})^2+\Gamma^2/4}$	$u = \frac{(E_{e_+}-E_{\beta_0})\|E^2\|}{(E_{e_+}-E_{\beta_0})^2+\Gamma^2/4}$
$s = \frac{1}{4}\frac{R^2\delta_r}{\delta_r^2+\Gamma^2/4}$	*	*

*The same as the column to the left of this one.

References for Appendix A

1. This appendix contains nothing original by the author and is presented merely as a convenience to the reader. Unpublished. Laurent Lévy dissertation, p.143, University of Michigan (1982). Gordon Drake, University of Windsor, Windsor, Canada. Private communication.

2. Throughout this appendix the following abbreviations are used:

$$\alpha{+1} \equiv \alpha{+} \,, \quad \alpha{-1} \equiv \alpha{-} \,, \quad \beta{+1} \equiv \beta{+} \,, \quad \beta{-1} \equiv \beta{-} \,.$$

3. Unpublished. Laurent Lévy, PhD Thesis, University of Michigan (1982) 147. Note that I have absorbed the • into the definition of the matrix elements.

APPENDIX B

Microcontroller

A. Introduction

General purpose micro- or minicomputers are commonly used to control experiments. In a typical experiment the computer may be used to control the duration of an event by providing a binary pulse of known width. Usually the computer software will change a bit in an output port from low to high, execute a number of instructions in a loop, then change the bit from high to low. Thus, the computer clock frequency and the number of instructions in the loop determine the width of the control pulse. There are several problems with this method. Ordinarily the width of the computer word (8, 16 or 32 bits for most general purpose computers) limits the number of devices that can be controlled simultaneously (within nanoseconds). Many computers have dynamic memory, causing the time required to execute an instruction loop to vary. When using a general purpose computer not specifically designed for experimental control, the sophistication of the software and hardware may be a problem. For example, an I/O processor between the user program and the I/O port will destroy the one-to-one correspondence between real time and the number of instructions executed. The user's program may time out periodically when a multiuser and/or multitasking operating system runs programs in the background. Sophisticated operating systems may make writing device drivers time consuming. Another problem is that commonly available micro/minicomputers require varying lengths of time to execute different instructions, making it difficult to determine the amount of time required to execute a complex sequence of events.

A solution to these problems would be a machine that has an arbitrarily long word length, and for which all instructions, even the case of a branch taken or not taken, require the same amount of time to execute. In this paper we describe a machine that has, in addition to these features, directly addressable I/O ports, no I/O processor, no dynamic memory, and no background processes.

B. Comparison to a General Purpose Computer

Like a general purpose computer, the microcontroller has memory in which instructions and data are stored, a control unit to decode and execute instructions, an arithmetic and logic unit (ALU), and I/O capability.

For sequencing and control applications the microcontroller has several features which make it more attractive than a general purpose computer. Since all instructions require the same amount of time (500 ns) to execute, it is relatively simple to write programs that use fixed time intervals to control laboratory apparatus. Writing data to an I/O port can be done significantly faster with the microcontroller than with most eight bit microprocessors and somewhat faster than with most sixteen bit microprocessors. During every 500 ns instruction cycle 16 bits of data can be transferred to an I/O port.

The disadvantage of the microcontroller design described here is that the user must program the device at the microprogram level. It must be loaded and controlled by a general purpose computer (hereafter referred to as the control computer), and it is not commercially available.

C. Block Diagram Description

The major components of the microcontroller are shown in fig. B.1. The upper left hand corner of the figure contains the control section of the microcontroller. It controls all sections of the microcontroller except the external control section. Instructions and data are stored in the microprogram memory. The microsequencer fetches instructions from microprogram memory and decodes and executes them. The microsequencer can branch on its own internal conditions or on conditions obtained from the ALU. The sixteen bit data bus (center of figure) is used to transfer data between components of the microcontroller. The number of bits in the data bus does not limit the number of devices the microcontroller can control. This point will be discussed in section VI.

The memory is a sixteen bit by 4k (k=1024) words static read/write memory. All data transfers to and from memory occur on the data bus.

The ALU is a general purpose unit with seventeen internal registers of sixteen bits each. The unit can perform additions/subtractions, increments/decrements, shifts, and logical operations with data contained in its registers or on the data bus. The ALU is useful for data reduction or signal integration when data must be compressed before being sent to the control computer.

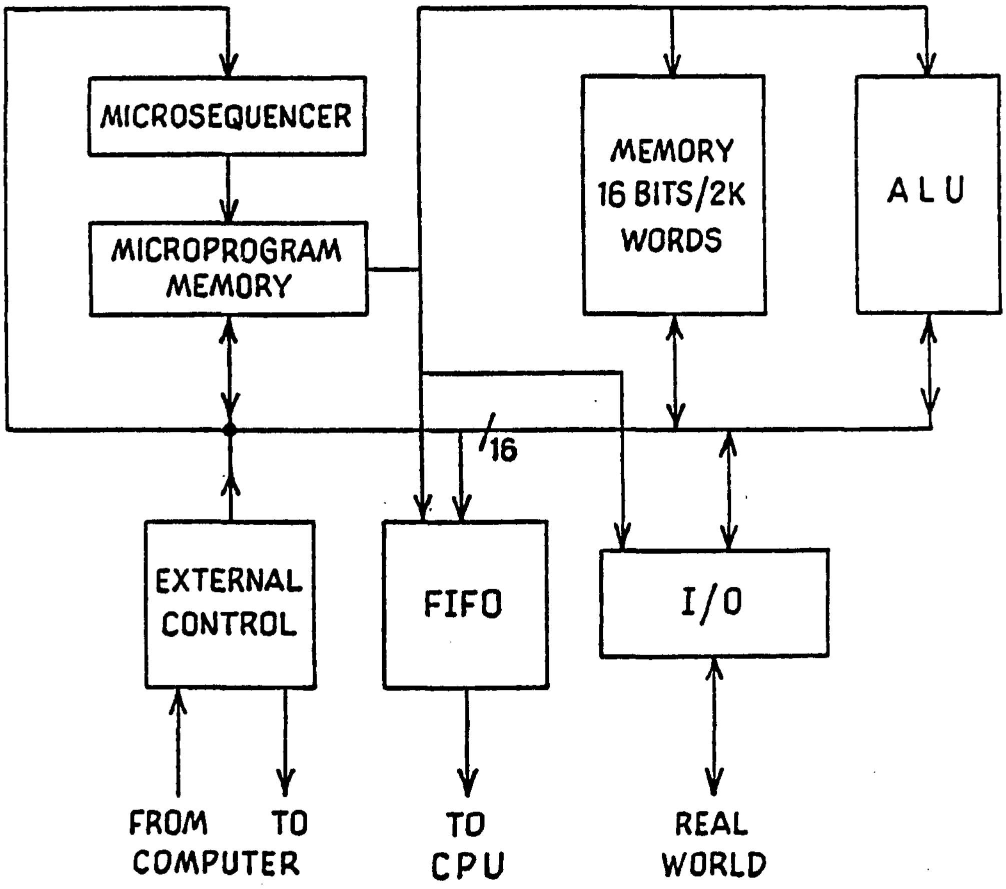

Figure B.1 Microcontroller - General Block Diagram

The I/O section is used to input/output data to the real world when speed is not important. The output section simply passes data to external devices through a series of latches. Microprogram memory, ALU, memory, and external control can all transfer data to the output section. The input section consists of tristate buffers through which memory, ALU, FIFO, and the output section can access data.

The external control section enables the control computer to communicate with and control the microcontroller. Two UART's, latches, buffers, and demultiplexers allow data and instructions from the control computer to be transmitted to the microcontroller. One UART is configured for bidirectional data transfer allowing data gathered by the microcontroller to be sent to the control computer. The contents of the microprogram memory and memory can also be sent to the control computer, permitting them to be verified after loading.

D. Detailed Circuit Description

The microcontroller is based on Advanced Microdevices' 2900 series microcontroller products. The control section of the microcontroller is a five phase clock, a twelve bit microprogram sequencer (AM2910), a microprogram address latch, microprogram memory and external control logic (see fig. B.2).

D.1. Five Phase Clock

A five phase clock (see fig. B.3 for pulse sequence) controls the execution of all microcontroller functions. The five phase clock runs continuously once started by the control computer.

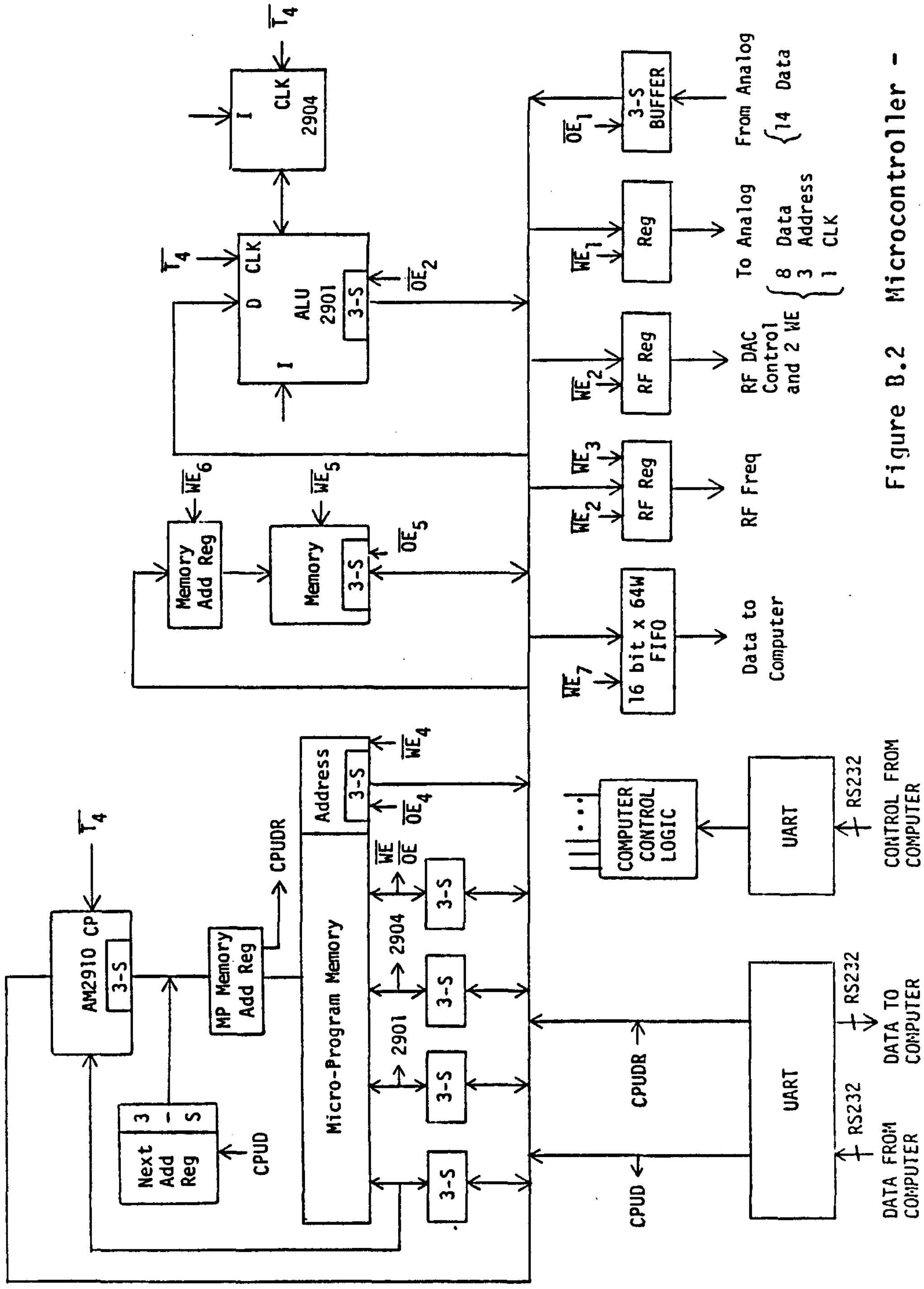

Figure B.2 Microcontroller - Detailed Block Diagram

*Are typically off, operate only under computer control.

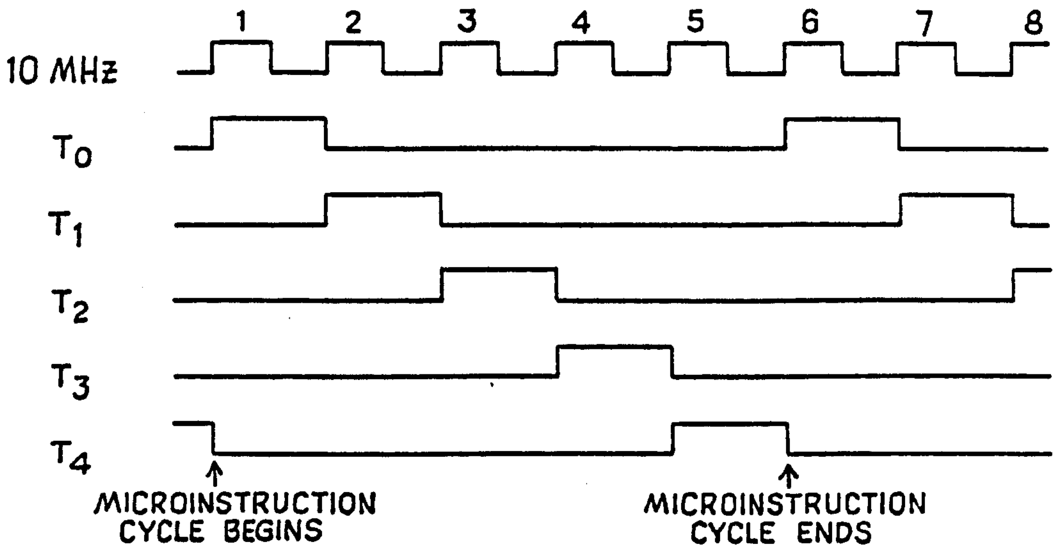

Figure B.3 Five Phase Clock

D.2. Microsequencer and Microprogram Memory

The Am2910 is an address sequencer that controls the order of execution of instructions stored in microprogram memory. It has the capability to sequentially access the microprogram memory or conditionally branch to any microinstruction in its 4096 word range (currently there are only 2048 words of microprogram memory). An internal stack allows subroutines to be nested five deep, and an internal counter provides loop count control with a capacity of 4096.

Before the end of every microinstruction cycle the Am2910 outputs the address of the next microinstruction. At the beginning of the next microinstruction cycle this address is latched in the microinstruction address latch. About 175 ns later the selected 56 bit word appears at the output of microprogram memory. During the remaining 325 ns of the instruction cycle the Am2910 selects the next microword address using its instruction, external conditions supplied on its condition code input, and internal conditions such as its current address. The new address is again latched at beginning of the next microinstruction cycle (the rising edge of T_4). Four bits of the 56 bit microword are used to control the Am2910. Six bits control the origin and destination of data transfers and thirty control the ALU. The remaining sixteen bits can be enabled onto the data bus. Thus, they are available to any device that can be written to.

D.3. Data Bus

The data bus is used to transfer data from one section to another. See fig. B.4. Three bits of the microword provide the input to a 3-to-8 line decoder (the output enable decoder) which is enabled during $T_2 + T_3 + T_4$. These outputs are used to enable different devices onto the data bus. Three other bits are used to provide the inputs to a write-enable decoder. The write-enable decoder is enabled during $T_2 + T_3$. The rising edge of its active low output is used to clock the contents of the data bus into different sections of the microcontroller. Microprogram memory, memory, ALU, input buffers, and the external control section can all output data. Devices to which data can be written are the memory address latch, memory, ALU, FIFO, and output buffers. All data transfers occur during a single microinstruction cycle. Programming the microcontroller consists of specifying the origin and destination of data transfers (and the location of each microinstruction). For example, the microcontroller can be programmed to output data contained in microprogram memory to one of the output buffers. A more complex application might comprise loading an address in an ALU register, incrementing it, loading that value into the memory address latch and writing that memory word to an output buffer. Repeating this passes a long table of data to external devices.

D.4. Memory

The address of the memory location to be read from (written to) is loaded into the memory address latch. The memory is then output enabled (write enabled). Memory is currently 16 bits by 4k words. It

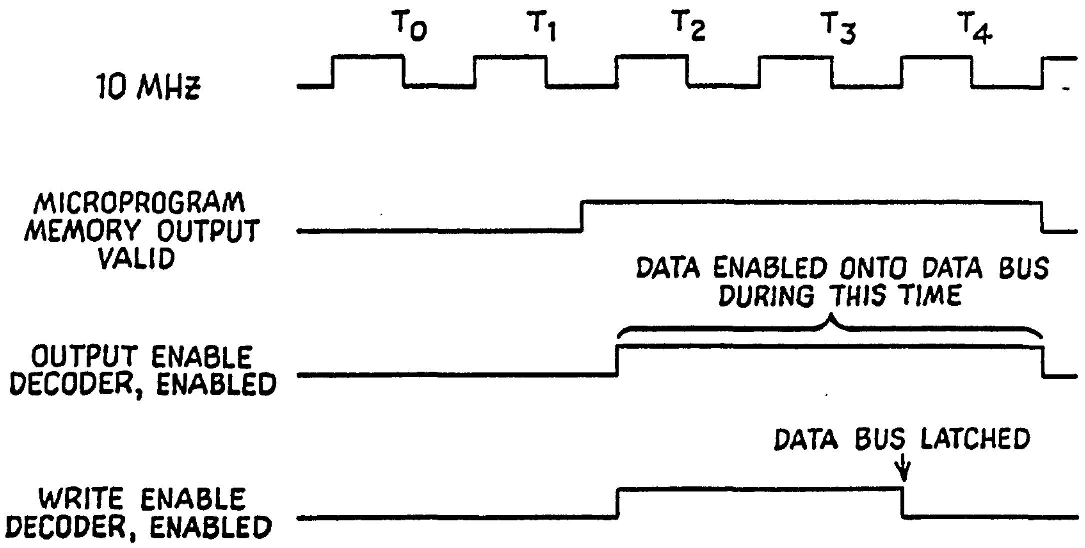

Figure B.4 Buss Timing Cycle

was designed to be expandable to 64k words with no modification to its control logic.

D.5. ALU

The ALU consists of four 4 bit ALU slices (Am2901), a status and shift control unit (Am2904), and a high-speed look-ahead carry generator (Am2902). The Am2901 contains 17 internal registers and performs arithmetic operations, logic functions, and a variety of shifts. The Am2904 performs miscellaneous functions that aid the ALUs with the generation of the carry-in signal to the Am2901s and storage and testing of Am2901 status flags. The Am2902 provides look-ahead carry generation for the Am2901s, resulting in shorter times for arithmetic operations.

D.6. External Control

The control computer uses three eight bit buses to control the microcontroller. One (control bus) is used to transmit instructions to the microcontroller, and the other two are used to transmit and read data (data return bus). The control bus drives a 5-to-24 line decoder which provides clock signals to various control registers in the microcontroller and tristate enable signals to buffers which can be enabled onto the data return bus. By loading the microcontroller control registers, the control computer can start, stop, advance the microcontroller clock phase, and load and verify the microprogram memory and memory. The control computer can execute all data transfers within the microcontroller that are possible under Am2910 control a single phase at a time.

E. Software Support

We have written several programs in C to support the microcontroller, including a cross assembler, microcontroller control package, and several test programs. The control package can load/verify the memory and microprogram memory, start, stop, single phase step, and single instruction start, stop, and advance the microcontroller. The test programs are capable of monitoring status bits in the ALU and FIFO, and testing either the microprogram memory or memory with user selectable data patterns.

F. Possible System Configurations

Without modification to existing circuit diagrams it would be possible to build a minimal system consisting of the microsequencer, microprogram address latch, microprogram memory and associated buffers, and the external control section. This would free 36 bits of microprogram memory that could be deleted or used to control other devices. Any or all of the following could be added one at a time to the minimal configuration: ALU, FIFO, memory, and I/O buffers. Few modifications would be required to add more microprogram memory or more I/O latches. Addition of more microprogram memory bits would allow direct control of devices in the laboratory. Software for microcontroller support should work on any machine that compiles C. Use of the software on different control computers may require slight modification of two routines which communicate with the control computer I/O ports.

APPENDIX C

Magnetic Field Control Unit

A. Introduction

A magnetic field control unit was designed, built, and tested to regulate the magnetic field in our experiment. It was designed to meet the following requirements:

1) 500-610 gauss operating range;
2) resolution ≅1/40 gauss, frequency synthesizer dependent;
3) absolute value of magnetic field not required, relative values sufficient;
4) stability over time (24 hours) and temperature (1K), $\Delta B/B < 10^{-5}$;
5) can reverse field to 1 part in 10^5;
6) does not disturb B field in the interaction region, i.e. cannot modulate local B field (frequency modulation of the rf source is used);
7) computer controlled, requiring a minimum of user interaction;
8) can step B field from value to value under computer control: Two stepping modes:
    a. no MNR feedback, step time 100 milliseconds
    b. NMR feedback, step time 800 milliseconds;
9) B field stepping synchronizable with E flip and ADC conversions to within nanoseconds;
10) above numbers of $10^{\pm 5}$ are good enough for the fast beam, attention is paid to requirements for slow beam requiring $10^{\pm 7}$.

B. Block Diagram Description

The magnetic field control unit is composed of four sections (fig. C.1); an NMR-reference feedback loop used to lock an NMR absorption dip to a reference frequency, a second feedback loop to

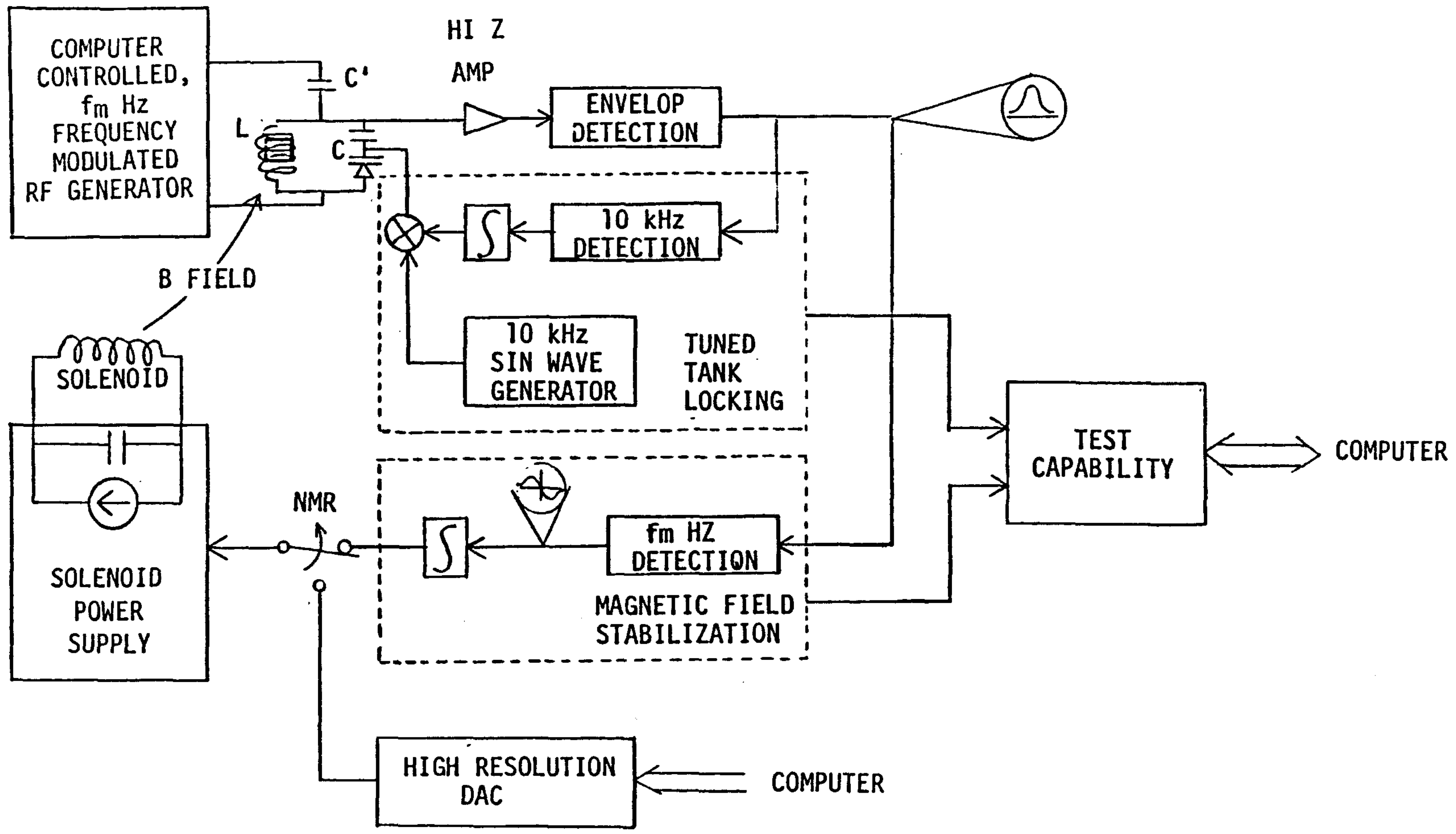

Figure C.1 Magnetic Field Control Unit - General Block Diagram keep a rf-tuned tank locked to the reference frequency, a high resolution DAC to step the magnetic field without reference to an NMR signal, and self-test electronics.

B.1 NMR Stabilization Loop

The magnetic field is stabilized by locking an NMR absorption dip to a reference frequency generated by a frequency synthesizer. The frequency synthesizer, operating at frequency ω_{rf_0}, and sinusoidally frequency modulated at frequency ω_Ω, applies a voltage V to a rf bridge consisting of a parallel LC tank tuned to ω_{rf_0} in series with a small capacitor, C'. The interior of the inductor contains a water sample doped with $CuSO_4$. When the magnetic field value is such that the proton resonance, ω_N, is near ω_{rf_0}, energy from the rf magnetic field generated by the inductor is absorbed in the water as the ω_{rf} passes through the proton resonance frequency. This lowers the impedance of the tuned tank, causing the voltage across the tank, V_0, to decrease. V_0 is amplified with a high-impedance low-noise amplifier, and after envelope detection, yields the familiar NMR absorption dip. The first Fourier harmonic is extracted from the absorption dip, producing the familiar dispersive lineshape shown at the output of the ω_Ω detection circuitry in fig. C.1. This Fourier harmonic is then used as the error signal to an integrator whose output controls the current in the solenoid, thus correcting deviations of the proton resonance from the frequency synthesizer's output. By making small (< .1%/sec) changes in the reference frequency, the magnetic field may be stepped through a desired sequence of values.

B.2 Tuned-Tank Balance Circuitry

The tuned-tank balance circuitry automatically keeps the peak of the tuned-tank resonance locked to the center of the rf modulation range. This is accomplished by modulating the tanks resonant frequency around the reference frequency by small amounts and detecting any differences between the average values. The difference is then used as an error signal to ocrrect the bias voltage of a vari-cap diode generating part of the tuned-tank capacitance, thus keeping the tuned-tank centered on the reference frequency.

B.3 Rapid Sequencing of the Magnetic Field

The magnetic field can be rapidly stepped from point to point by pulsing the power supply control input with specific patterns. This is accomplished by removing the NMR referenced portion fromthe control loop and just using the DACs.

B.4 Test Capability

The magnetic field control unit has the capability to monitor all internal variables that must be monitored to ensure systematic free operation (see section D), and those used to optimize performance.

C. Detailed Block Diagram Description

The frequency synthesizer, all DAC's, and all analog switches are software programmable (see figure C.2).

C.1 NMR Stabilization Loop

The system frequency reference is a 10 MHz crystal clock. It is divided by 10 for use by the frequency synthesizer and by 10^5 to generate 100 Hz (ω_Ω). The 100 Hz square wave is filtered by a high Q filter with a bandpass of about 1 Hz, its amplitude controlled with a multiplying eight bit DAC, then used to frequency modulate the frequency synthesizer. It was necessary to use a frequency derived from the synthesizer's reference for the frequency modulation. The (digital feedback loop) frequency synthesizers divide its 1 MHz reference and its output frequency down to 100 Hz for comparison. This generates sidebands at ±100 Hz on the output frequency that beat with the desired frequency modulation causing the detected NMR signal to oscillate at the difference frequency. The second use of the 100 Hz is extraction of the first and third harmonics from the NMR signal. The 100 Hz is transmitted to the analog section via an optical isolator. The square wave output of the optical isolator is bandpass filtered at 100 and 300 Hz by active filters with Q's of about 100. The 100 and 300 Hz signals are then multiplied together with the output of the envelope detector, thus extracting the first and third harmonics of the NMR signal.

The output of the frequency synthesizer is a TTL-compatible square wave capable of driving 50 ohms. Its amplitude is controlled

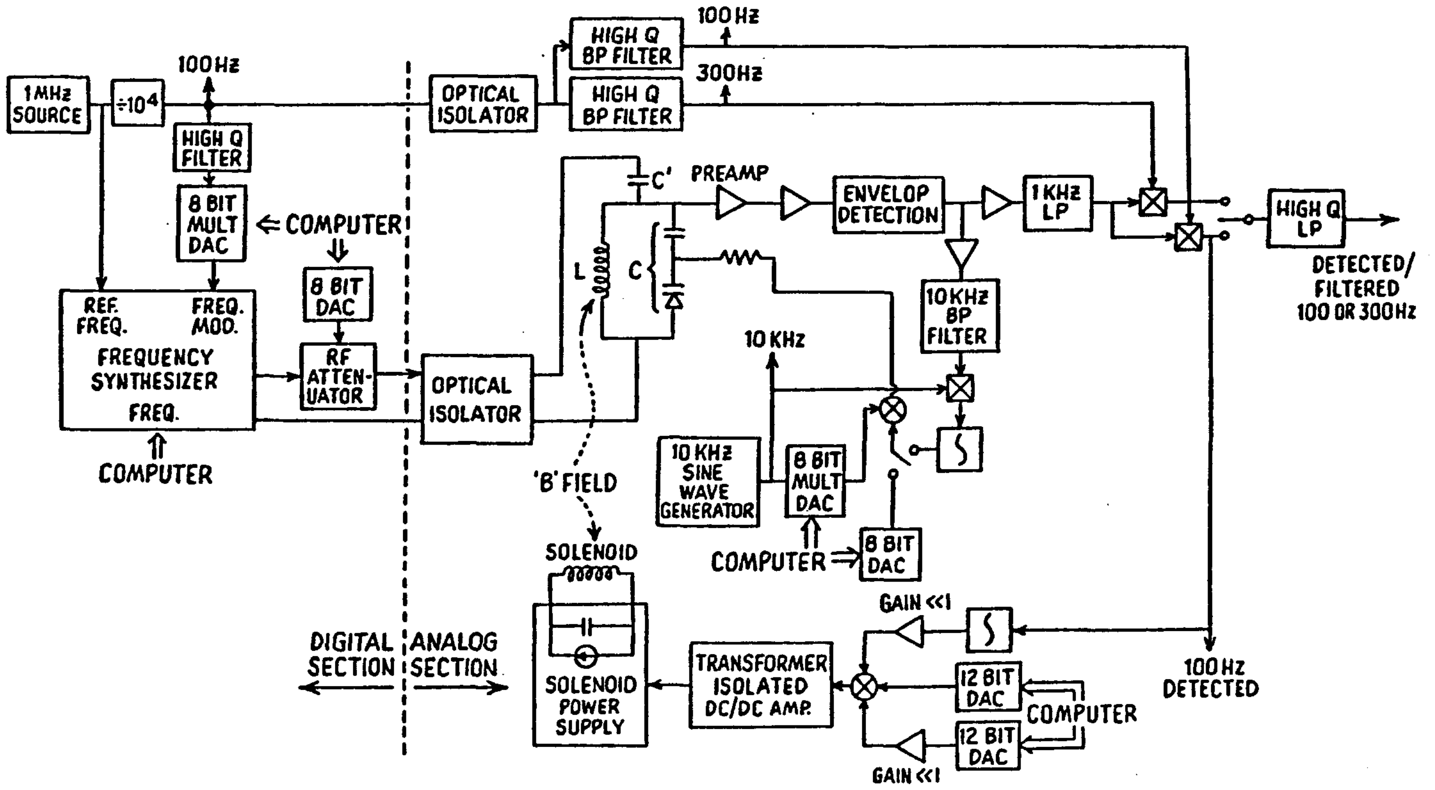

Figure C.2 Magnetic Field Control Unit - Detailed Block Diagram by an rf attenuator whose control current is set by an eight bit DAC. The rf is then optically isolated onto the rf tank. The tanks Q of 60 select the ω_{rf_0}harmonic of the square wave.

All of the change in the tank voltage due to NMR absorption occurs across the preamp input if the tank is driven with a current source. In practice the tank is in series with a small capacitor C'. Making $Z_{C'} >> Z_{tank}$ approximates this condition.

The voltage across the tank, V_0, is amplified by a factor of 12 with a high-impedance low-noise FET preamplifier.[3] The preamplifier noise is significantly lower than the tuned-tank Johnson noise. After the preamplifier, V_0 is amplified by a factor of five and envelope detected using diode rectification. Envelope detection results in the same signal-to-noise as synchronous detection,[4] since the signal-to-noise is large. The detected signal is then amplified and low-pass filtered at 1 KHz yielding the NMR absorption dip. The first and third Fourier harmonics are extracted from the absorption dip. The first harmonic is used an integrator's error signal, the output of which is summed with the output of two 12 bit DACs. The sum of these three voltages is used to control the current in the solenoid.

To achieve stabile operation, the integrator's gain is << 1, resulting in the integrator being unable to control the solenoid current throughout a five gauss range (a typical scan range). Therefore, as the magnetic field is scanned, the DACs outputs are adjusted. Both DACs have a voltage range of zero to ten volts. The course DAC has a gain of one, and the fine DAC has a gain << 1. The sum of the two form a DAC with a resolution of 19.5 straight binary bits. To change the magnetic field only the coarse DACs output is adjusted. The fine DAC is only required for fast stepping of the magnetic field.

C.2 Tuned-Tank Balance Circuitry

To achieve maximum signal-to-noise, it is necessary to keep the rf bridges resonant frequency, ω_{Q_0}, the same as that of the proton resonance.[1] This is achieved by assuming ω_N is the same as ω_{rf_0} and locking ω_{Q_0} to ω_{rf_0}.[2] This illustrated by assuming ω_{rf_0} is a constant. The total tank capacitance, C, is partially generated by a vari-cap diode, thus permitting electronic control of the tank resonant frequency. ω_{Q_0} is modulated symmetrically around ω_{rf_0} at frequency ω_C by modulating C around the capacitance required for tank resonance at ω_{rf_0}. C is modulated by summing a small ac voltage of frequency ω_C with the dc voltage required to achieve tank resonance at ω_{rf_0}. If for some reason ω_{Q_0} is not centered on ω_{rf_0}, V_0 will contain amplitude modulation at ω_C. After envelope detection (fig. C.2), any harmonics at ω_C are phase-sensitively detected. The output of the phase sensitive detector is a dispersive lineshape in the quantity $\omega_{Q_0}-\omega_{rf_0}$. It is used as an error signal to the input of an integrator whose output is used to apply V_{Bdc} to the vari-cap diode. Since the tuned tank balance circuitry corrects differences between ω_{Q_0} and ω_{rf_0} the tuned tank will automatically follow changes in the reference frequency. Thus, automatically following the stepping of the magnetic field.

The signal that modulates the vari-cap diode in the tuned tank at ω_C is generated by a single chip waveform generator. ω_C's amplitude is controlled by an eight bit multiplying DAC. The sine wave output of the wave form generator is used to phase sensitively detect the ω_C component of the envelope detected output of the tank. The detected ω_C component is the error signal for the integrator which directly drives the vari-cap diode in the tuned tank. For diagnostic purposes, the integrator can be switched out and an eight bit DAC switched in.

C.3 Rapid Sequencing of the Magnetic Field

For some data gathering modes it is only necessary to spend 100 milliseconds at a given magnetic field value. Thus it is desirable to be able to rapidly sequence the magnetic field. Doing this using NMR stabilization requires a minimum of 800 milliseconds per field point for two reasons. First, the frequency synthesizer requires 450 milliseconds to settle to within ten percent of its final value. Second, the solenoid power supply is a voltage-controlled current source in parallel with a 0.003 farad capacitor, driving a load of 2.5 henries in series with 21.5 ohms. The current source responds in less than one millisecond to a request for a step function change in the output current. 800 milliseconds elapses before 96 percent of the current is flowing through the solenoid, and not onto the capacitor. This problem is overcome with the following technique.

Changing the current in an inductor instantaneously requires a delta function of voltage applied to it, fig. C.3. To step the solenoid current quickly, a high resolution DAC drives the power

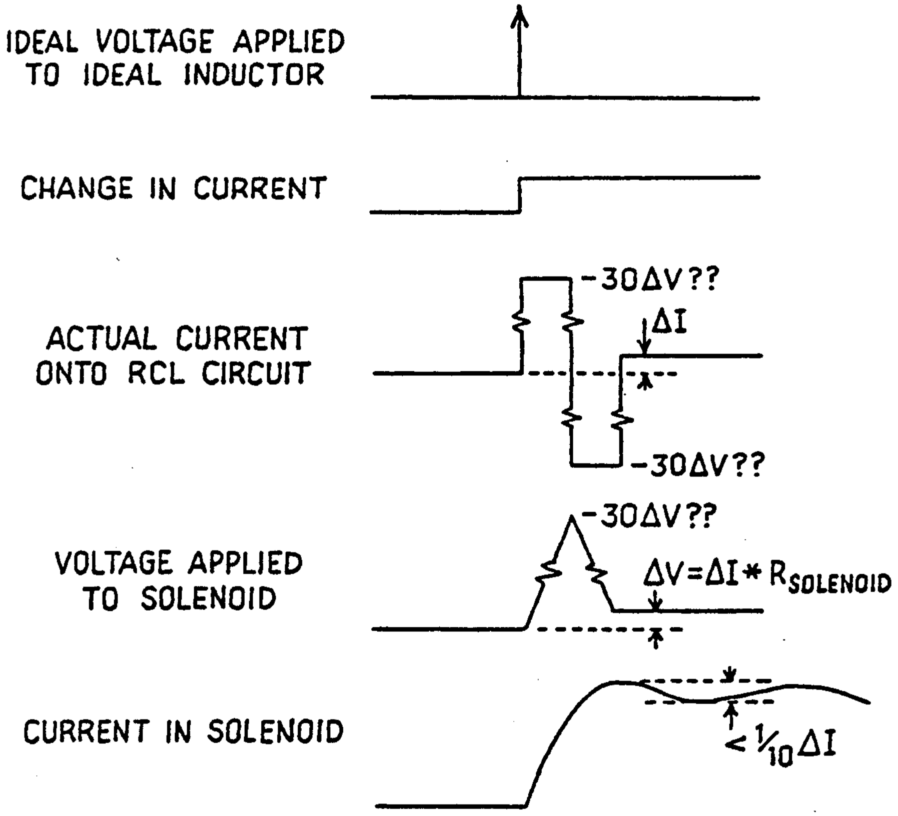

Figure C.3 Rapid Sequencing of Magnetic Field Value supply control input so that the voltage across the solenoid approximates a delta function as closely as possible. To change the solenoid current by ΔI, the control input is overdriven 81 ΔI for 10 milliseconds (fig. C3.2), causing the voltage across the solenoid to ramp up (current source driving a capacitor) well beyond its final value. The current is then underdriven by 71 ΔI for 10 milliseconds resulting in the voltage ramping down to its final value, and the current in the solenoid being within ten percent of its final value.

By calibrating the DAC with NMR, the magnetic field can be moved rapidly with the DAC, while stabilizing the field at its new value with NMR. Since the present frequency synthesizer requires 800 milliseconds to settle, it would have to be replaced to do this.

C.4 Test Capability

The magnetic field control unit has the capability to monitor all internal variables required to ensure systematic-free operation (see Section D), and those used to optimize performance.

The following voltages can be monitored with a sample-and-hold and 12 bit ADC:

Tuned-tank resonance just after detection
Tuned-tank locking loop multiplier output offset
Tuned-tank locking loop integrator output
NMR absorption dip
NMR 1st harmonic multiplier output offset
NMR 3rd harmonic multiplier output offset
NMR loop integrator output
10 Hz low pass filter of detected 1st and 3rd harmonic
Coarse DAC output

D. Performance Analysis

D.1 Analytical Description of NMR and LRC Resonant Circuit

This section describes and compare the NMR absorption dip and LRC tuned-tank resonance (hereafter called the Q curve). Analytical expressions for the Fourier harmonics of both curves are known.[5,6]

Throughout this work all Lorentzian-shaped functions are assumed of unit height, independent of width. The NMR absorption dip is assumed to be Lorentzian. It can be shown that an LRC tuned-tank approximates a Lorentzian when $1/Q^2 << 1$ and $(\omega_0-\omega)/\omega_0 << 1$, both easily satisfied in this sytem. Table C.1 defines symbols.

D.1(a) Fourier expansion of modulated Lorentzian line shapes

A Lorentzian line shape has the form:

$$G(x) = 1/(1+x^2) \; . \tag{D.1}$$

Sinusoidal modulation of x, replaces x by x + m cosωt, where

$$\begin{aligned} x &= 2\,\frac{\omega_0-\omega}{\omega_{1/2}} \; , \\ \text{and} \quad m &= \omega_m/\omega_{1/2} \; , \\ \omega_{1/2} &= \text{full width at half maximum} \; , \\ \omega_m &= \text{peak-to-peak sine wave modulation} \; . \end{aligned} \tag{D.2}$$

Expanding (D.1) in a Fourier series of the general form:

$$S(x,t) = \sum_{n=0}^{n=\infty} S_n(x)\cos(n\Omega t) \tag{D.3}$$

Table C.1

Frequently Used Symbols

ω_{rf_o}	: average value of rf
ω_Ω	: frequency of the frequency modulation of ω_{rf}
$\omega_{rf_{min/max}}$	: minimum/maximum instantaneous values of rf
ω_{Q_o}	: average value of the tuned tank resonance (T^2R)
$\Delta\omega_Q$	: FWHM of LCR T^2R
$\omega_{Q\Omega_{min/max}}$	: min/max instantaneous value of T^2R at frequency Ω due to tuned tank following ωrf because of automatic tank balancing
ω_C	: frequency of the amplitude modulation of the vari-cap by the TTB system
$\omega_{QC_{min/max}}$	: min/max instantaneous value of T^2R at frequency ωC
ω_N	: frequency of NMR resonance
$\Delta\omega_N$	: FWHM of NMR resonance

$$X_Q = (\omega_{rf_o} - \omega_{Q_o})/\Delta\omega_Q$$

$$X_N = (\omega_{rf_o} - \omega_N)/\Delta\omega_N$$

$$m_{rf} = \frac{1}{2}\frac{(\omega_{rf_{max}} - \omega_{rf_{min}})}{\Delta\omega_Q}$$

$$m_{Q\Omega} = \frac{1}{2}\frac{(\omega_{Q\Omega_{max}} - \omega_{Q\Omega_{min}})}{\Delta\omega_Q}$$

$$m_{QC} = \frac{1}{2}\frac{(\omega_{QC_{max}} - \omega_{QC_{min}})}{\Delta\omega_Q}$$

$$m_N = \frac{1}{2}\frac{(\omega_{rf_{max}} - \omega_{rf_{min}})}{\Delta\omega_N}$$

where,

$$S_n(x) = \frac{1}{2}\frac{1}{m^n}\varepsilon_n i^n \frac{\{[(1-ix)^2 + m^2]^{1/2} - (1-ix)\}^n}{[(1-ix)^2 + m^2]^{1/2}} + \text{c.c.}\ , \qquad \text{(D.3b)}$$

$$\varepsilon_0 = 1\ ,\ \varepsilon_n = 2 \quad (n=1,2,\ldots)\ .$$

For n=1,

$$S_1(x) = \frac{(2)^{1/2}}{m}\frac{x[(M^2+4x^2)^{1/2} + M]^{1/2} - [(M^2+4x^2)^{1/2} - M]^{1/2}}{(M^2 + 4x^2)^{1/2}} \qquad \text{(D.3c)}$$

where,

$$M = 1 - x^2 + m^2\ .$$

For m << 1,

$$S_1(x) = -2xm/(1+x^2)^2 + O(m^3)\ ,$$

approximating the first derivative.

Numerical optimization of $S_1(x)$ as a function of m, to yield the largest value for small x, results in $m = 0.71\pm0.01$. It is suspected that if an analytical expression were found, it would be $m = 1/\sqrt{2}$. This yields an ideal peak-to-peak modulation amplitude of,

$$m_{opt} = \omega_{1/2}/\sqrt{2} \qquad \text{(D.4)}$$

For $m = m_{opt}$, and x small, numerical calculation yields

$$S_1(x) = 0.76x \qquad \text{(D.5)}$$

The expressions presented here can be used to describe the shape of the NMR absorption dip and the Q curve.

D.1(b) Description of LRC resonant circuit

The NMR coil and the capacitor in parallel with it are modeled as an ideal inductor, L, in series with an ideal resistor, R, both of which are in parallel with an ideal capacitor, C. The impedance, $|Z|$, of the circuit near resonance, assuming $Q >> 1$, where
$Q = \omega_0 L/R$ and $\omega_0 = 1/\sqrt{LC}$, is:

$$|Z| \cong \frac{1}{[(R/\omega L)^2 + (\omega C - 1/(\omega L))^2]^{1/2}} \qquad (D.6)$$

Assuming $1/Q^2$ and $(\omega_0 - \omega)/\omega_0 << 1$, equ. D.6 can be rearranged to yield:

$$|Z| \cong \frac{Q/(C\omega_0)}{1 + 2Q^2((\omega_0 - \omega)/\omega_0)^2} \qquad (D.7)$$

This is a Lorentzian with $x = \sqrt{2}\, Q(\omega_0 - \omega)/\omega_0$.

D.1(c) NMR Lineshape

Assuming relaxation effects can be ignored, the NMR absorption dip can be approximated as a Lorentzian.[6] How closely the actual resonance can be approximated by a Lorentzian is unknown at this time, however, the following analysis assumes the NMR signal is Lorentzian.

D.2 Noise and Signal Strengths

A limitation to the accuracy with which the magnetic field can be measured is the available signal-to-noise. A fundamental limitation of the current approach is the Johnson noise of the inductor. A practical limitation is the noise induced by electronic components. This section discusses the available signal size and relevant noise sources.

D.2(a) Johnson noise of the coil

Assuming the R in the tuned-tank generates Johnson noise given by $V_n = \sqrt{4kTR\Delta f}$ the noise voltage seen by the preamp is

$$v_{rms} = V_n Q = \sqrt{4kTZ\Delta f} \qquad (D.8)$$

where,

k = Boltzman's constant = 1.38×10^{-23} Joule/K ,

T = circuit temperature in °K ,

Z = tank impedence (at resonance $Z = QL\omega_o = RQ^2$),

Δf = observation bandwidth in Hz .

In a properly designed circuit this should be the only noise, and, hence, is the limiting factor in the signal-to-noise ratio.

D.2(b) NMR absorption dip signal size

It can be shown that the signal size is

$$v_s = k'Q(\omega_o^3 L)^{1/2} \qquad (D.9)$$

where k' is a constant. (Where does this come from????) This results in the following signal-to-noise ratio,

$$S/N = \frac{k'\omega_o^{3/2}Q^{1/2}}{(4kTZ\Delta f)^{1/2}} \qquad (D.10)$$

D.2(c) Noise introduced through tuned-tank balance circuitry (TTBC)

The tuned-tanks vari-cap diode is controlled by application of a voltage. This introduces noise into the tuned tank at all frequencies. The noise is a potential problem in three frequency ranges; at the NMR frequency, at the vari-cap modulation frequency, and at the rf modulation frequency. The noise at all of these frequencies is sufficiently small so as not to be a problem.

D.3 Systematics

This section develops a mathematical model for the NMR signal plus the Q-curve after envelope detection. Ideally this signal would be an NMR absorption dip which is a sine wave modulated, nonsaturated, Lorentzian. However, the reference frequency (ω_{rf_0}) is a frequency modulated at harmonics of ω_Ω in addition to ω_Ω, Q-curve harmonics are mixed with those of the NMR absorption dip, and there are dc offset voltages in the control loops locking the NMR absorption dip to ω_{rf_0} which must be considered.

D.3(a) Description of detected Q-curve and NMR signal

The model used for a general description of the NMR and Q curve after envelope detection is shown in figure C.4. The motivation for this model is stated very nicely by Andrews,[8] pg. 33, "This equality of voltage is no coincidence, since it merely expresses the fact that absorption in any system at a given frequency may be simulated by replacing the absorber with an oscillator of the same frequency, but of opposite phase.... However,...such oscillators are not a fiction,

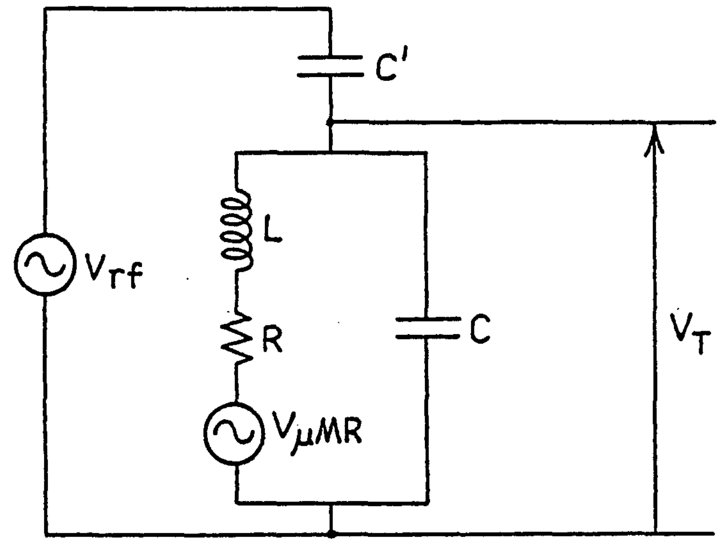

Figure C.4 NMR Tuned Tank Model

but are actually present in the form of the forced precession of the resultant magnetic moment about H_0....one may continue to observe nuclear induction of the freely precessing magnetic moment after the radiofrequency field has been switched off." Using superposition this model results in,

$$V_{Total} = V_{rf} \frac{Z_T}{(Z_{C'} + Z_T)} + V_{NMR} \frac{Z_T}{R + Z_L} , \qquad \text{(D.11a)}$$

where Z_T is the impedance of the tuned-tank (equ. D.1), and $Z_{C'}$ and Z_L are the impedances of C' and L respectively. Before this expression is Fourier analyzed, several simplifications are made. Both denominators of D.11a are almost pure imaginary. Therefore, when calculating $|V_T|$ the magnitude of the sum is approximately equal to the sum of the magnitudes. This results in the following,

$$|V_T| \cong V_{rf} \left|\frac{Z_T}{(Z_{C'} + Z_T)}\right| + V_{NMR} \left|\frac{Z_T}{R + Z_L}\right| \qquad \text{(D.11b)}$$

Replacing $Z_{C'} + Z_T$ with $Z_{C'}$ ($|Z_{C'}|/|Z_T| \cong 20$) results in an error of 1/20 in the size of V_{rf}. Replace $R + Z_L$ by Z_L resulting in an error of less than one part in a hundred. Replace the ω dependence in $Z_{C'}$ and Z_L by ω_{Q_0}, causing an error of about one part in ten thousand assuming ω is instantaneously frequency modulated with a width of 200 Hz. (The actual frequency spectrum of the frequency- and amplitude-modulated signals from the tuned-tank have not been worked out. However, experimentally this approximation is known to be very good.) This results in the following:

$$|V_T| \cong V_{rf} \left|\frac{Z_T}{Z_{C'_o}}\right| + V_{NMR} \left|\frac{Z_T}{Z_{L_o}}\right| , \tag{D.12}$$

where $Z_{C'_o} = Z_{C'}(\omega_o)$ and $Z_{L_o} = Z_L(\omega_o)$.

Approximating Z_T and V_{NMR} by Lorentzian lineshapes results in,

$$Z_T = Z'_T \frac{1}{1 + X_T^2} , V_{NMR} = V'_{NMR} \frac{1}{1 + X_N^2} . \tag{D.13}$$

Equation D.13 assumes ideal models for the tuned tank and absorption dip. This is expected to be a good approximation for the tuned tank since it is operated close to its peak and modulated over such a small fraction of its width. However, the absorption dip is modulated rapidly over most of its width, causing distortion. Deviations from ideal lineshapes is accounted for by adding an error term to Z_T and V_{NMR}. With the above substitutions, equation (D.12) becomes

$$V_T \cong V_{rf} \left|\frac{Z'_T}{Z_{C'_o}}\right| (\frac{1}{1+X_T^2} + E_T) [1 + \frac{V'_{NMR}}{V_{rf}} \left|\frac{Z_{c'o}}{Z_{L_o}}\right| (\frac{1}{1+X_N^2} + E_N)] \tag{D.14}$$

where E_T and E_N are the error terms for the tank resonance curve and the NMR curve, respectively.

To get an idea of how large some of the above terms are, note that,

$$X_T \cong \frac{\omega_{rf_o} - \omega_{Q_o}}{\frac{1}{2}\,\Delta\omega_Q} = \frac{2.3\times10^6\text{Hz}\times10\text{ppm}}{\frac{1}{2}\,60\text{kHz}} \sim 10^{-3}$$

Therefore, $1/(1+X_T^2)$ can be expanded in powers of X_T^2. Since V'_{NMR}/V_{rf}, X_T^2, and E_T are all << 1, all products of them in equ. D.14, are dropped, resulting in the equation for the detected voltage which is Fourier analyzed,

$$V_T \cong V_{rf}\,\frac{|Z'_T|}{|Z_{C_o}|}\left[\frac{1}{1+X_T^2} + E_T + \frac{V'_{NMR}}{V_{rf}}\,\frac{|Z_{C_o}|}{|Z_{L_o}|}\left(\frac{1}{1+X_N^2} + E_N\right)\right. \qquad (D.15)$$

Although all the errors in equ. D.15 could be lumped into one error term, better understanding of the system results by keeping the error terms separate. E_T can be measured without the NMR signal present, and then E_N measured by subtraction with both signals present.

D.3(b) Harmonic distortion

Closed form solutions for the Fourier spectrum of $1/(1 + x^2)$ where $x = x_o + m\cos(\omega t)$, were discussed in section D.1(a). The actual system has $x = x_o + m\cos(\omega_m t) + \sum m'\cos(\omega'_m t + \phi'_m)$, where the primes represent extraneous frequency modulation, most likely at $\omega'_m = 2\omega, 3\omega, \ldots$ and ϕ'_m is some phase angle. Two sources of this are nonlinearities in the frequency synthesizer response to its frequency modulation voltage, and the frequency modulation voltage containing higher order harmonics. These harmonics can appear at ω_m by being mixed with ω_m by the nonlinearities of the Lorentzian lineshape. The occurance of unwanted harmonics is called harmonic distortion.

The NMR absorption dip has been analyzed, assuming no tuned-tank background, for the effect of 2ω and 3ω harmonic distortion at ω and 3ω. Analytical calculation shows that only one error is important, $\omega' = 2\omega$ and $m' = 0.01m$ results in the zero crossing of the ω and 3ω detected channels shifting about 2 ppm.

This analysis not been done for the tuned-tank background, but the effects would be very small due to the larger width of the tuned-tank resonance, about 60 kHz vs. 200 Hz for the NMR signal.

D.3(c) DC offsets at the multiplier output and the integrator input

The multiplier output offset voltage (V_{moo}) and the integrator input offset voltage (V_{iio}) causes systematic shifts of the magnetic field point being stabilized. These voltages occur in the NMR stabilization loop and the tuned tank balance circuit. The general circuit description used for both loops is illustrated in figure C.5. a_1 is the size of the first harmonic at either ω_m or ω_C, given by (see table C.1),

$$a_1 = \frac{m}{m_{opt}} 0.76xS \qquad (D.16)$$

where:

m_{opt} , the optimal modulation amplitude
m , the actual modulation amplitude, $m < m_{opt}$
x , offset of line center
S , peak signal height

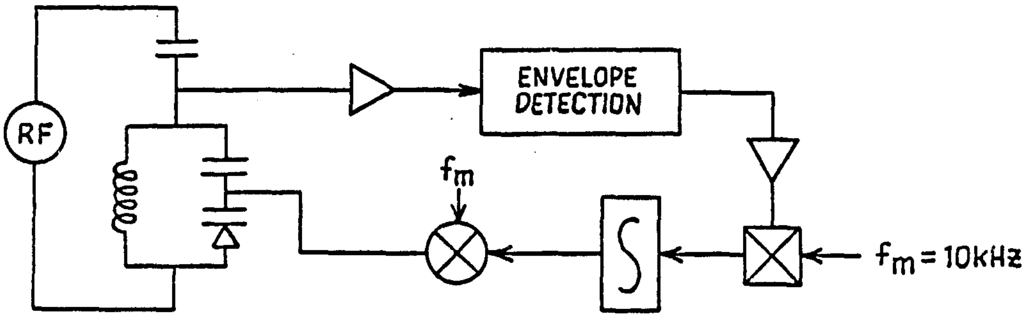

Figure C.5a Feedback Loop for Tuned Tank Balance

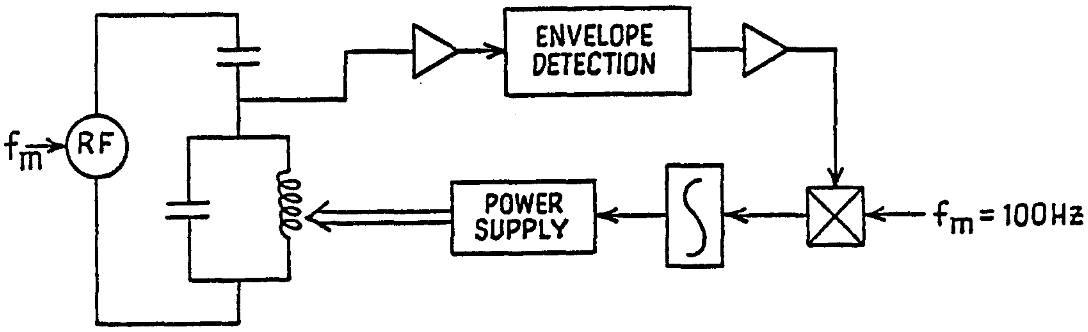

Figure C.5b Feedback Loop for NMR Signal

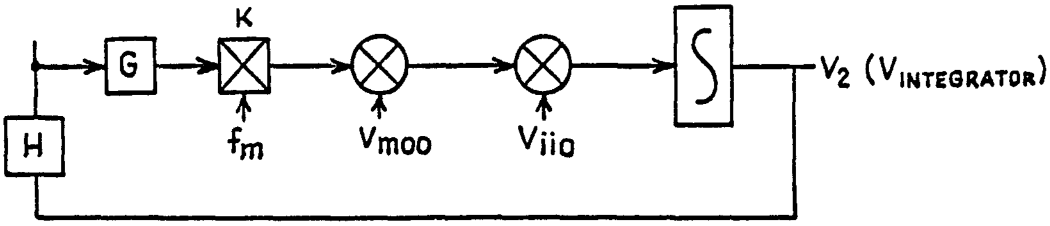

Figure C.5c Generalized Feedback Loop for NMR and Tuned Tank Balance, Including Offset Voltages

The dc component of the multiplier output is GKa_1, plus the multiplier output offset voltage. This voltage is summed with the integrators input offset voltage, yielding

$$V_i = \int_{-\infty}^{t} (GKa_1 + V_{moo} + V_{iio})dt \qquad (D.17)$$

The control loop steady state response results in the ideal integrator input voltage being zero. This causes a_1 to be stabilized at a value correcting for the offset voltages

$$a_{1ss} = -(V_{moo} + V_{iio})/GK \ . \qquad (D.18)$$

This locks the feedback loop to a location offset from the zero crossing of the first Fourier harmonic, resulting in an x_{error} of,

$$x_e = - \frac{m_{opt}}{m} \frac{1}{0.76} \frac{1}{GK} \frac{(V_{moo} + V_{iio})}{S} \qquad (D.19)$$

(i) Offset voltages in the NMR stabilization loop

Changes in the offset voltages in the NMR stabilization loop will shift the value of the magnetic field by an amount given by equ. D.19. See table C.2 for permitted sizes of offset voltages.

(ii) Offset voltages in the tuned-tank balance circuit

Offset voltages in the tuned-tank balance circuit (TTB) indirectly effects the magnetic field value because Q-curve harmonics are detected along with the NMR harmonics. Non-zero offset voltages in the TTB loop offset the Q-curve from the middle of the rf

Table C.2

Practical Numbers for NMR Stabilization Loop

Desired B field stability/°C	10 ppm	0.1 ppm
V_{moo}	100 μV/°C	*
V_{iio}	5 μV/°C	*
$m_N = m_{opt}$	$1/\sqrt{2}$	*
S,NMR signal height	50 μV	*
Assumed linewidth	200 Hz	*
Allowed Δx/°C	0.1	0.001
Required GK	105	1.05×10^4

*Same as column to left.

modulation range, causing the first harmonic of the Q-curve to be detected in the NMR loop along with the NMR signal. To keep the integrator's input zero, the NMR loop offsets the NMR resonance in the opposite direction causing the magnetic field to shift. This effect can be made arbitrarily small by adjusting the gains in the TTB loop.

Keeping the TTB offset voltages small enough to remove undesirable shifts in the magnetic field requires,

$$\frac{d}{dP} a_{1Q\Omega} < \frac{d}{dP} a_{1N} < x_{NEmax} \tag{D.20}$$

where

P = any parameter that effects a_{1Q} or a_{1N}, the case being analyzed is offset voltages

$a_{1Q\Omega}$ = a_1 in NMR loop at Ω due to Q-curve not centered on rf modulation, i.e. $X_Q \neq 0$

a_{1N} = a_1 in NMR loop at Ω due to NMR curve not centered on rf modulation, i.e. $X_N \neq 0$

x_{NEmax} = the maximum error allowed in the NMR loop

Recall that

$$a_{1N} = \frac{m_N}{m_{opt}} 0.76 X_N S_N \tag{D.21}$$

$$a_{1Q\Omega} = \frac{m_{Q\Omega}}{m_{opt}} 0.76 X_Q S_Q \tag{D.22}$$

$$a_{1Q\omega C} = \frac{m_{QC}}{m_{opt}} 0.76 X_Q S_Q \tag{D.23}$$

Observing that m_{QC} can be made larger than $m_{Q\Omega}$ and, hence, $a_{1Q\omega C} > a_{1Q\Omega}$, then if $a_{1Q\omega C}$ is signal-to-noise limited, $a_{1Q\Omega}$ will be even smaller. Knowing $m_{Q\Omega}$ and an allowed upper limit for $a_{1Q\Omega}$,

$$X_Q = a_{1Q\Omega} \frac{m_{opt}}{m_{Q\Omega}} \frac{1}{0.76 S_Q} \tag{D.24}$$

Substituting D.24 into D.25 thus sets alimit on the allowable $a_{1Q\omega c}$ occurring in the TTB loop.

$$a_{1Q\omega C} = \frac{m_{QC}}{m_{Q\Omega}} a_{1Q\Omega} \tag{D.25}$$

Using D.25 a limit on $(GK)_Q$ results,

$$a_{1Q\omega C} > \frac{V_{moo} + V_{iio}}{(GK)_Q}$$

$$(GK)_Q > \frac{V_{moo} + V_{iio}}{a_{1Q\omega C}} = \frac{V_{moo} + V_{iio}}{\frac{m_{QC}}{m_{Q\Omega}}\, a_{1Q\Omega}} = \frac{m_{Q\Omega}}{m_{QC}} \frac{V_{moo} + V_{iio}}{a_{1N}} = \frac{m_{Q\Omega}}{m_{QC}} (GK)_N$$

or

$$(GK)_Q > \frac{m_{Q\Omega}}{m_{QC}}(GK)_N$$

$(GK)_N$ is given in table C.2.

References for Appendix C

1. A. Abragam, The Principles of Nuclear Magnetism, Oxford, at the Clarendon Press, 1961.

2. K. Borer, "The Nuclear Magnetic Resonance System for the CERN Muon Storage Ring," Nuclear Instruments and Methods 143 (1977) 203-218.

3. J. Quateman, private communication.

4. A. Bruce Carlson, Communication Systems An Introduction to Signals and Noise in Electrical Communication, Second Edition, 1968, McGraw-Hill Book Company.

5. H. Wahlquist, Journal of Chemical Physics 35, #5 (1961).

6. R. Arndt, Journal of Applied Physics 36, #8 (1965).

7. P. Cerez and A. Brillet, Metrologia 13 (1977) 29-33.

8. E.R. Andrew, Nuclear Magnetic Resonance, Cambridge University Press, 1955.